ANISOTROPIC ETCHING OF Si(100) IN AQUEOUS SOLUTIONS

A Dissertation

Presented to the Faculty of the Graduate School

of Cornell University

In Partial Fulfillment of the Requirements for the Degree of

Doctor of Philosophy

by

Ankush Gupta

January 2011

ANISOTROPIC ETCHING OF Si(100) IN AQUEOUS SOLUTIONS

Ankush Gupta, Ph.D

Cornell University 2011

The microelectronics industry has long sought an aqueous etchant that could produce atomically flat Si(100) surfaces by anisotropic etching. This dissertation shows that near-atomically-flat Si(100) surfaces *can* be produced by an aqueous silicon etchant — 40% NH_4F (aq.). The etching of Si(100) in 40% NH_4F (aq.) produced H_2 bubbles as a reaction product, which led to significant roughening of the surface if not removed. A near-atomically flat surface was produced if the bubbles were periodically removed from the etching surface. Analysis of the infrared spectrum of the NH_4F-etched surface showed that the surface was H-terminated. A new spectral deconvolution technique led to reinterpretation of the spectral bands and revealed the surface structure that is consistent with the STM images of the surface. Investigations of the bubble-induced roughening of Si(100) surface during NH_4F etching revealed a new mechanism of {111} microfacet formation on this surface.

To understand the etch kinetics that produced the observed morphologies, a fully atomistic kinetic Monte Carlo simulation of Si(100) etching was developed. The simulations showed that previously postulated models of H/Si(100) etching based solely on bond counting or interadsorbate stress cannot explain the experimental etch morphologies. The simulations suggested mechanisms that lead to the formation of flat stripes, hillocks, and rough morphologies observed on etched Si(100) surfaces. The production of long rows observed on the NH_4F-etched Si(100) surface could only be explained by the fast etching of dihydrides bonded to monohydrides — termed as

"α-dihydrides".

In addition, a comprehensive study of the vibrational spectrum of various H-terminated Si surfaces produced by NH_4F (aq.) etching was performed using density functional theory. The simulations predicted stretch mode energies within 2% of the experimentally observed; however, the accuracy of the calculations was strongly affected by interadsorbate strain. Simulation of point defects on H/Si(100) surfaces provided insights into the origin of large heterogeneous broadening observed on NH_4F-etched Si(100) surfaces.

BIOGRAPHICAL SKETCH

Ankush Gupta was born in New Delhi in India. He did his primary education in Prakash Punj Vidya Sadan (New Delhi), the high school (grade 6^{th} to 10^{th} in the Indian education system) in St. Joseph's Academy, and senior secondary schooling (grade 11 and 12) in Smt. Durgabai Deshmukh Andhra Education Society Sr. Sec. School (New Delhi). Soon after that, he joined Indian Institute of Technology, Kanpur to pursue a 5-year integrated Masters program on Chemistry. After finishing his undergraduate in 2005, he came to U.S.A. to join the Ph.D. program in Chemistry at Cornell University. Here he did his graduate research work in the group of Prof. Melissa A. Hines. After finishing his Ph. D., he is heading back to India to fulfill his life's purpose.

Dedicated to the Divine Masters who illuminated for me the way…

ACKNOWLEDGMENTS

This dissertation, although is compilation of my graduate research work, but is a result of efforts of many individuals who have visibly and invisibly contributed to my research as well as my graduate experience at Cornell. These individuals have made me to reach this stage so that I can present this text to you and be eligible to receive a Ph. D. degree.

First and foremost is my research supervisor Prof. Melissa A. Hines. Her enthusiasm, ingenuity, and sincerity for science was what caused me to stay in the graduate school in the first place (since I wasn't sure if I want to do a Ph.D., even after coming to Cornell). Working with her allowed me to get a first hand experience of a rare combination of skills ranging from electronics to machining to computing to writing and presenting (apart from doing chemistry). Her understanding nature, patience, and helping hand is what helped me move on through the up and down of the research as well as the melodrama of success and failures and reach this finish line. None of this undermines the constant guidance she provided from the beginning of the research projects to the writing of this thesis. I sincerely thank her for her constant patience, understanding and guidance.

I also thank Prof. Richard Hennig for guiding me through the mysteries of DFT calculations. His cheerfulness and constant helping hand made the whole work a fun adventure and a great rewarding experience.

I thank Prof. Jiwong Park and Prof. Roger Loring for serving on my special committee.

No amount of thanks would suffice for what my buddies Ian, Brandon and Marc gave to me in this graduate work. Apart from being a co-fighter in some of the scientific battles that we fought leading to this dissertation, they have been constant source of fun, support, and inspiration (particularly when you are looking for a quick

one). I also thank past group members Debodhonyaa and Amy for the valuable help they gave me in getting started with the research work and the cheerful group atmosphere they created in the lab. I would also like to thank Verónica L. Morales for her help in conducting the side-profile bubbles evolution experiments.

Next, I would like to thank Tom McCarrick for amazing learning experience he provided as instructor for the physical chemistry lab courses for which I served as a TA, and being always available for any help. A lot of thanks to Lars Washburn without whom a lot of small and big experiments would have given me much more torture, and who was always willing to help with his knowledge as well as his lab tools.

I thank my friends Dom, Paulina, Kursad, Yogi, Cristina, Ashivni, Preetha, Amit, Anand, Alper, Vatsav, Garima, Mahbud, Henrike, and the great community members of Ithaca who helped and supported me through the good and the bad times, making this place a home away from home. I also offer my honors to my friend Kurt, who left this world before I could finish my dissertation.

Finally, I thank the department of Chemistry for giving me the opportunity to take courses, conduct research, and serve as a teaching assistant, each of which helped me to learn and grow in many ways.

TABLE OF CONTENTS

LIST OF FIGURES

LIST OF TABLES

Chapter 1

Introduction

1.1. Anisotropic Etching

A sphere of single crystal silicon when etched in KOH (aq.) transforms into an isodecahedron with vertices along the slow etching (111) and (100) directions of the crystal.[1] This orientation-dependent etching of crystalline surfaces is termed "anisotropic etching" and has been both a subject of fascination and a useful tool to mineralogists and material scientist for past two centuries.[2,3] In the 1950's, researchers discovered that anisotropic etchants could be used to identify (atomic scale) dislocations and other defects in crystals[4] — a property that played an important role in the development of technologies for producing high-purity crystalline silicon. Anisotropic etchants are now an important tool for bulk micromachining in nanofabrication. For example, anisotropic etchants such as KOH and tetramethyl ammonium hydroxide can be used to machine silicon structures with high precision, enabling low-cost production of intricate nanostructures for use as sensors and actuators for pressure, force, flow, and acceleration.[5]

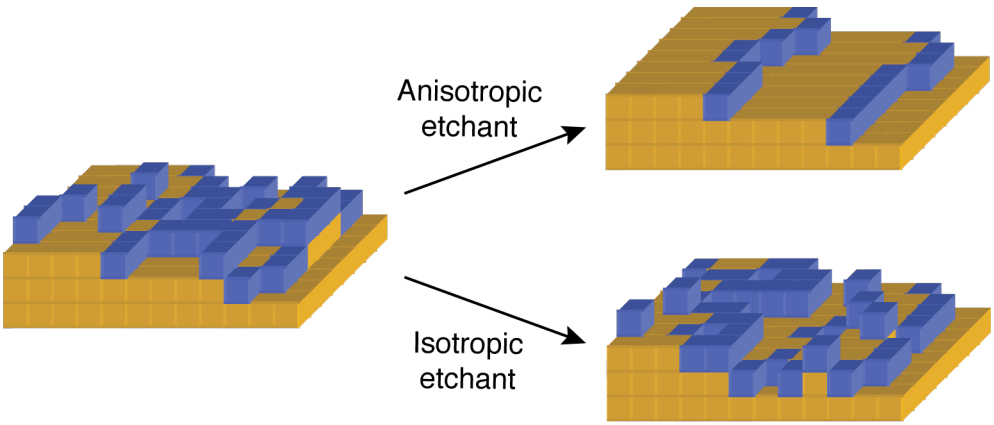

Figure 1.1. An anisotropic etchant preferentially etches defects sites (such as step and kink sites), shown in blue, over the terrace, shown in yellow, leading to the production of smooth terraces. In contrast, an isotropic etchant etches sites randomly, producing rough surfaces.

At the atomic scale, etchant anisotropy stems from the preferential removal of specific defect sites (such as step and kink sites) by the etchant. Fig. 1.1 schematically illustrates the result of anisotropic etching on a simple cubic crystal. Rapid etching of kink and step sites leads to step-flow etching and the production of a near-flat surface. In contrast, an isotropic etchant removes surface sites with little or no selectivity, leading to the formation of rough surfaces.

One of the landmarks in anisotropic etching was the production of atomically-smooth Si(111) surfaces by NH_4F (aq.) etching which was reported by Higashi *et al.*[6] in 1990. Figure 1.2 shows a scanning tunneling microscope (STM) image of a Si(111) surface prepared by NH_4F etching of an initially rough surface; the high-resolution image in the inset shows the atomic-scale perfection of the etched terraces. The infrared spectrum of the etched surface displays a single sharp Si-H stretch band with a linewidth of 0.9 cm^{-1} (0.1 cm^{-1} at T = 130 K)[7] — the narrowest linewidth ever observed for a covalently-bonded adsorbate on a surface.

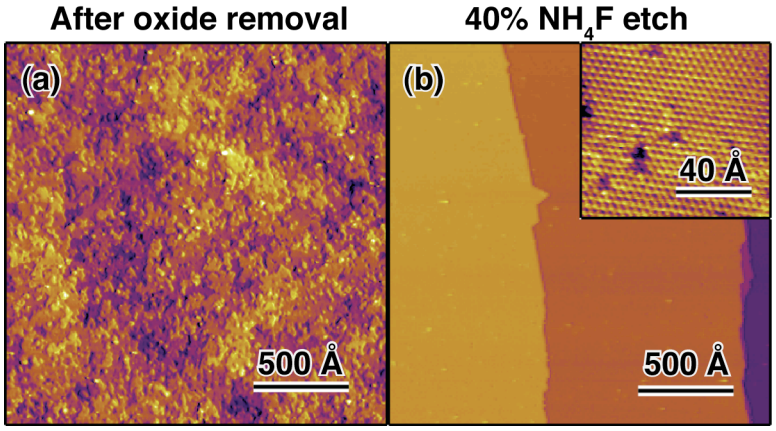

Figure 1.2. STM images of Si(111) surfaces obtained after (a) surface oxide removal and (b) etching in 40% NH_4F (aq.).

Detailed understanding of etched Si(111) surfaces in terms of their chemical structure and morphologies stimulated the development of atomistic simulations of the anisotropic etching of these surfaces.[8-10] The simulations were used in conjunction with

the experimental morphologies to quantify the site-specific etch kinetics on these surfaces. In particular, these studies elucidated the reactivity of various defect sites, which are present in extremely low concentrations and beyond the detection limit of most surface analysis tools. These studies led to significant insights into the etching reaction mechanisms on these surfaces.

1.2. Si(100) Surface and its Anisotropic Etching

In the microelectronics industry, Si(100) is the preferred Si substrate for device fabrication.[11] The Si/SiO_2 interface on Si(100) has better interfacial electronic properties for the fabrication of complementary metal-oxide-semiconductor (CMOS) devices. Additionally, Si(100) wafers are favored for square chip dicing since this surface has four orthogonal {110} cleavage planes normal to the wafer surface.

The performance of CMOS transistors, among other factors, depends upon the surface smoothness of the starting Si wafers, as the initial roughness of the wafers degrades the properties of CMOS devices fabricated on these wafers. For example, Ohmi *et al.*[12] showed that increasing the root-mean-square roughness of the starting wafers from 2 Å to 10 Å decreases the channel mobility in metal-oxide-semiconductor field-effect transistors (MOSFETS) fabricated on these wafers by a factor of four. Later, similar investigations showed that reducing the initial roughness of wafers also leads to reductions in low-frequency noise[13] and increase in the dielectric breakdown field[14] in CMOS devices fabricated on these wafers.

One of the principle sources of Si wafer roughness is the aggressive chemicals that are used to clean the surfaces during device fabrication. An ideal cleaning solution would be one that would anisotropically etch Si(100) wafers to produce atomically-smooth surfaces.

This ideal Si(100) etchant was actively sought by dozens of research groups around the world; however, all evidence suggested that aqueous etchants tend to

roughen Si(100) surfaces. The infrared spectra of Si(100) surfaces etched in NH_4F (aq.) and other HF-based etchants had multiple broad and complex bands in the Si-H stretch regions.[15-20] Cluster simulations[15] suggested that the multiple broad bands were due to heterogeneous (rough) surfaces terminated with mono-, di-, and trihydrides. This interpretation served as the unquestioned basis for all subsequent infrared analyses of etched H/Si(100) surfaces. In contrast, an atomically-flat H/Si(100) surface would be completely dihydride terminated, as shown in Fig. 1.3, with an infrared spectrum consisting of two well-defined Si-H stretch modes. The common understanding[21] that emerged from these studies was that aqueous etchants progressively roughened (100) surfaces, in part, by producing slow-etching (111) microfacets.

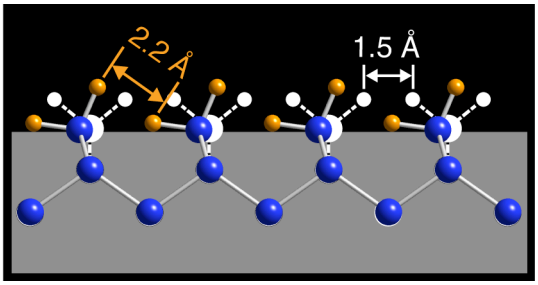

Figure 1.3. Predicted structure of the ideal H/Si(100) surface showing canting of dihydrides to relieve interadsorbate strain. The bulk-terminated position of atoms is shown in white. The Si and H atoms are shown in blue and orange, respectively.

Contrary to this understanding, this dissertation shows that aqueous etching by the well-known etchant NH_4F *can produce* near-atomically-smooth Si(100) surfaces. Re-investigation of this etching system showed that the hydrogen bubbles produced on the surface by the etching reaction led to profound roughening of surface. A near-atomically-smooth morphology, shown in Fig. 1.4, was produced by periodically removing the bubbles from the etching surface. Surprisingly, the infrared spectrum of the near-atomically-smooth surface was identical to the (broad) spectrum previously reported; however, a new deconvolution technique led to a reinterpretation of the

spectral bands. In addition, investigations of the bubble-induced roughening during NH_4F etching revealed a new, unexpected mechanism of (111) microfaceting on the Si(100) surface due to bubble formation.

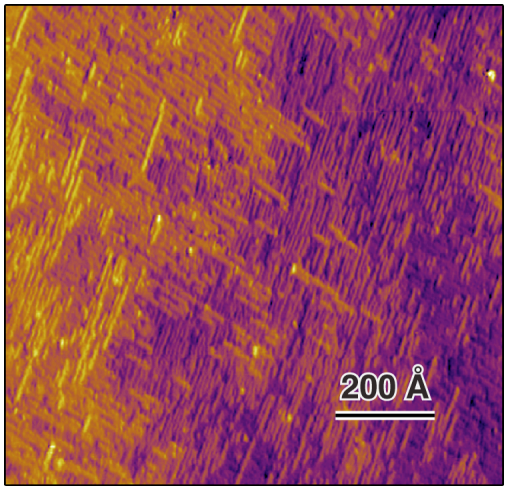

Figure 1.4. STM image of a Si(100) surface etched in room-temperature 40% NH_4F (aq.).

The difficulty in producing flat Si(100) surfaces has been attributed to the interadsorbate strain on this surface. On a bulk-terminated H/Si(100) surface, as illustrated in Fig. 1.3, the distance between H atoms on neighboring dihydrides would be 1.51 Å, much less than the 2.4 Å van der Waals diameter of H,[23,24] which would lead to severe steric strain. Simulations of this surface[22,25-27] predict a canting of the dihydrides to increase the interhydride distance, thereby reducing the interadsorbate strain. Flat H/Si(100) terraces, however, have not been observed experimentally over extended regions. The previous conclusions about roughening of Si(100) surfaces in aqueous etchants were often explained in terms of strain reduction, as the H/Si(111) facets are unstrained. Analysis of the NH_4F-etched surface showed that although etching reduces interadsorbate strain by ~50%, strain is not minimized.

The production of near-atomically-flat Si(100) surface during NH_4F etching warranted re-examination of the existing computational models of H/Si(100) etching. These models were predominantly based upon a bond-counting approach[28-30] (*i.e.*,

competitive etching of dihydrides, monohydrides, and trihydrides). Nearest-neighbor effects on the site reactivities were sometimes included using phenomenological parameters.[31] These models did not predict formation of near-atomically-flat Si(100) morphologies as observed in NH_4F etching. In addition, Faggin *et al.*[32] recently reported that de-oxygenated H_2O etches Si(100) to produce the H-terminated, highly homogenous surface shown in Fig. 1.5. To investigate the chemical origins of these etch morphologies, a fully-atomistic Kinetic Monte Carlo (KMC) simulation of H/Si(100) etching was developed. The KMC simulation studies showed that bond-counting models or models based purely upon interadsorbate strain cannot explain the observed morphologies. The simulations suggested that the site reactivity is governed by a complex interplay of factors.

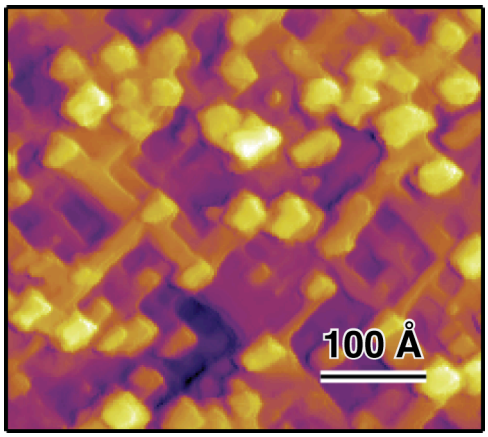

Figure 1.5. STM image of a Si(100) surface etched in room-temperature, deoxygenated H_2O for 11 hr.[32]

1.3. Outline of the Dissertation

This dissertation broadly consists of three parts. The first part describes the morphological evolution of Si(100) surfaces during etching in room temperature 40% NH_4F (aq.) solutions. The experimental techniques that were used for Si sample preparation and the characterization of the etched surfaces are described in Chapter 2. Chapter 3 describes the production of a near-atomically-flat morphology on Si(100) by

NH_4F etching. The roughening of the Si(100) surface by H_2 bubbles produced during NH_4F etching is described in Chapter 4; a novel mechanism of {111} microfacet formation by bubbles is proposed.

The second part presents KMC simulations of the anisotropic etching of Si(100) surfaces in aqueous solutions in Chapter 5. The simulations suggested mechanisms that could explain the formation of flat stripes, {111} microfaceted hillocks, and rough morphologies observed on experimental Si(100) surfaces etched in aqueous solutions. In particular, simulations suggested that the high reactivity of a particular type of dihydride explains the formation of long rows on NH_4F-etched Si(100) surface (Fig. 1.4).

The third part of this dissertation, Chapter 6, describes density functional theory simulations of the infrared spectra of H-terminated silicon surfaces produced by aqueous etching. The simulations confirmed the interpretation of the experimental spectra. A variety of defects on the H/Si(100) surfaces were simulated, thereby explaining the unusually large linewidths observed on NH_4F-etched Si(100) surfaces.

REFERENCES

[1] P. J. Hesketh, C. Ju, S. Gowda, E. Zanoria, and S. Danyluk, J. Electrochem. Soc., **140**, 1080 (1993).

[2] A. P. Honess, *The Nature, Origin, and Interpretation of the Etch Figures on Crystals* (John Wiley & Sons, New York, 1927).

[3] K. Sangwal, *Etching of Crystals: Theory, Experiment, and Application* (Elsevier, Amsterdam, 1987).

[4] W. C. Dash, in *Growth and Perfection of Crystals*, edited by R. H. Doremus, B. W. Roberts, and D. Turnbull, (Wiley, New York, 1958), p. 361.

[5] M. Elwenspoek and H. V. Jansen, *Silicon Micromachining* (Cambridge Univ. Press, Cambridge, 1998).

[6] G. S. Higashi, Y. J. Chabal, G. W. Trucks, and K. Raghavachari, Appl. Phys. Lett. **56**, 656 (1990).

[7] P. Dumas, Y. J. Chabal, and G. S. Higashi, Phys. Rev. Lett. **65**, 1124 (1990).

[8] J. Kasparian, M. Elwenspoek, and P. Allongue, Surf. Sci. **388**, 50 (1997).

[9] J. Flidr, Y.-C. Huang, T. A. Newton, and M. A. Hines, J. Chem. Phys. **108**, 5542 (1998).

[10] H. Zhou, J. Fu, and R. M. Silver, J. Phys. Chem. C **111**, 3566 (2007).

[11] A discussion on properties of various crystallographic orientations of Si can be found in F. Shimura, *Semiconductor Silicon Crystal Technology* (Academic Press, Inc., San Diego, 1989), p. 53.

[12] T. Ohmi, K. Kotani, A. Teramoto, and M. Miyashita, IEEE Electron Dev. Lett. **12**, 652 (1991).

[13] P. Gaubert, A. Teramoto, T. Hamada, M. Yamamoto, K. Kotani, and T. Ohmi, IEEE Trans. Electron Dev. **53**, 851 (2006).

[14] R. Kuroda, T. Suwa, A. Teramoto, R. Hasebe, S. Sugawa, and T. Ohmi, IEEE Trans. Electron Dev. **56**, 291 (2009).

[15] Y. J. Chabal, G. S. Higashi, K. Raghavachari, and V. A. Burrows, J. Vac. Sci. Technol. A **7**, 2104 (1989).

[16] P. Dumas, Y. J. Chabal, and P. Jakob, Surf. Sci. **269/270**, 867 (1992).

[17] M. Niwano, Y. Takeda, Y. Ishibashi, K. Kurita, and N. Miyamoto, J. Appl. Phys. **71**, 5646 (1992).

[18] C. H. Bjorkman, M. Fukuda, T. Yamazaki, S. Miyazaki, and M. Hirose, Jpn. J. Appl. Phys. **34**, 722 (1995).

[19] M. Nakamura, M. B. Song, and M. Ito, Electrochim. Acta **41**, 681 (1996).

[20] N. Miyata, S. Watanabe, and S. Okamura, Appl. Surf. Sci. **117/118**, 26 (1997).

[21] Y. J. Chabal, G. S. Higashi, and R. J. Small, *Handbook of Silicon Wafer Cleaning Technology* (2nd Edition), edited by K. A. Reinhardt and W. Kern (William Andrew Publishing, Norwich, NY, 2008), p. 515.

[22] J. E. Northrup, Phys. Rev. B **44**, 1419 (1991).

[23] L. Pauling, *The Nature of Chemical Bond* (3rd Edition), (Cornell Univ. Press, Ithaca, NY, 1960), p. 260.

[24] V. Gogonea, C. Bãleanu-Gogonea, and E. Osawa, J. Mol. Struct. (Theochem) **432**, 177 (1998).

[25] S. Ciraci and I. P. Batra, Surf. Sci. **178**, 80 (1986).

[26] K. Endo, K. Arima, K. Hirose, T. Kataoka, and Y. Mori, J. Appl. Phys. **91**, 4065 (2002).

[27] U. Freking, P. Krüger, A. Mazur, and J. Pollmann, Phys. Rev. B **69**, 035315 (2004).

[28] H. Camon, M. Djafari, D. Estève, A. M. Gué, and Z. Moktadir, Microsys. Technol. **1**, 163(1995).

[29] H. Camon, Z. Moktadir, and M. Djafari-Rouhani, Mat. Sci. Eng. B **37**, 142 (1996).

[30] M. A. Gosálvez, R. M. Nieminen, P. Kilpinen, E. Haimi, V. Lindroos, Appl. Surf. Sci. **178**, 7 (2001).

[31] M. A. Gosálvez and R. M. Nieminen, New J. Phys. **5**, 100.1 (2003).

[32] M. F. Faggin, S. K. Green, I. T. Clark, K. T. Queeney, and M. A. Hines, J. Am. Chem. Soc. **128**, 11455 (2006).

Chapter 2

Experimental Techniques

The experiments on silicon etching consisted of three essential components: preparation of reproducible, H-terminated starting Si surfaces, etching of the surface in an aqueous etchant, and characterization of the etched surface morphology and its chemical structure. Sample preparation involved dicing samples from commercial Si wafers and cleaning the diced samples to remove contamination and mechanical damage on the surface. These procedures are described in Section 2.1. The etching procedures were specific to each experiment and are discussed in Chapter 3. Chemical characterization of the etched surfaces used polarized infrared (IR) spectroscopy in both the multiple-internal-reflection (MIR) and transmission geometries, which is described in Section 2.2. Morphological characterization of the etched surfaces by scanning tunneling microscopy (STM) is described in Section 2.3.

2.1. Sample Preparation and Cleaning

To obtain reproducible starting surfaces, silicon samples must be processed to remove morphological and chemical imperfections. Even though commercial silicon wafers are optically smooth, they are rough at the nanoscale. An oxidation and annealing step was used to generate reproducibly (albeit not atomically) smooth surfaces. In addition, Si etching is extremely sensitive to even trace amounts of contaminants, both metallic and organic. Heavy metals, such as Cu, Fe, Ag, and Cr, induce unwanted redox reactions at Si surfaces, which can lead to large etch pits or impurity islands (even at concentrations as low as 10^{10}atoms/cm^2).[1,2] Adsorbed organic impurities and particulate matter can mask the etching surface, thereby producing etch hillocks or leading to unstable tunneling during STM imaging. A number of chemical

processing steps were, therefore, used to remove all contaminants and produce a fully H-terminated starting surface.

The as-received Si wafers were oxidized in 1 atm of O_2 at 1100°C for 45 min to produce a ~1000-Å-thick SiO_2 layer, which engulfed any surface defects and impurities. The wafers were then annealed at 1100°C for 30 min in 1 atm of N_2 to smooth the Si/SiO_2 interface.[3,4] The oxide layer also passivated the surface and protected the Si/SiO_2 interface from damage during the sample cutting process.

To dice the wafers into samples, the wafers were glued to a glass plate using a thermoplastic adhesive (Crystalbond 509, Aremco Products, Inc.) and then coated with a sacrificial layer of the adhesive to protect the surface. The wafers were then diced using a diamond saw into 0.6″ × 1.5″ size samples for infrared spectroscopy or 0.6″ × 0.7″ samples for STM imaging. Diced samples were reheated, removed from the glass plate, and immersed in acetone for 30 min to remove the adhesive layer. Residual glue and other organic contaminants were removed with sequential immersion in refluxing trichloroethylene, room temperature acetone, and room temperature methanol. Immediately after the methanol wash, the samples were rinsed in ultra-pure water, obtained by filtration of reverse-osmosis, de-ionized water in a Milli-Q (Millipore) filtration system, to prevent deposition of any solid residue from the drying methanol on the surface. The ultra-pure water had a resistivity of 18.2 MΩ-cm and total organic carbon (TOC) level less than 20 ppb.

For infrared spectroscopy in the MIR geometry, the two short ends of the sample were beveled at 45º. For this beveling, the samples were glued with the thermoplastic adhesive to a custom-made stainless-steel chuck that held the sample edge at 45º to the polishing surface. Multiple samples were glued on top of one another on the chuck to reduce the risk of sample breakage during polishing. The edges of the samples were successively polished with a 320 grit abrasive pad, a 600 grit abrasive pad, a 3.0 micron

alumina slurry, and a 0.05 micron alumina slurry (Buehler) on a Buehler Metaserv Grinder Polisher. The samples were then de-glued from the chuck, rotated by 180º, re-glued, and polished similarly on the other side.

Since metals and most plastics would react with the aggressive solutions used in these experiments and release contaminants into the solution, all cleaning and etching procedures used solid Teflon or glass labware. The labware was subjected to the RCA cleaning procedure, developed by Kern and Puotinen in 1960's,[5] before each experiment. In the first step, the labware was immersed for 20 min in a basic peroxide solution, known as "standard clean 1" (SC1), which consisted of approximately 1:1:4 by volume of 14 M NH_4OH (aq., EMD Chemical, ACS grade), 30% H_2O_2 (aq., J. T. Baker, CMOS grade), and ultrapure H_2O at 80°C. This alkaline peroxide solution is very effective at oxidizing and removing organic impurities, and the ammonia solvates metals through the formation of amine complexes.[6] The labware was then rinsed in ultra-pure water and immersed for 20 min in an acidic peroxide solution, known as "standard clean 2" (SC2), which consisted of approximately 1:1:4 by volume of 13 M HCl (aq., J. T. Baker, ACS grade), 30 % H_2O_2 (aq., J. T. Baker, CMOS grade), and ultrapure H_2O at 80°C. The SC2 solution dissolves alkali metals, metal hydroxides [e.g., $Al(OH)_3$, $Fe(OH)_3$], and transition metals (e.g., Ag, Au).[6] The labware was then rinsed in ultra-pure water and used for cleaning and etching of the sample. When not in use, all labware was stored under ultra-pure water to prevent contamination.

After the labware was cleaned, the sample was first cleaned in a fresh SC1 solution at 80ºC for 10 min followed by a thorough rinse in ultrapure water. The sample was then cleaned in a fresh SC2 solution at 80ºC for 10 min followed by an ultrapure water rinse. The thick protective oxide layer was then removed by a 75 s immersion in buffered oxide etch (BOE, J. T. Baker, CMOS grade), which consisted of 5:1 by volume of 40% NH_4F (aq.) and 50% HF (aq.). The profound hydrophobicity of H-

terminated samples was used as a visual indicator of complete removal of the (hydrophilic) oxide layer. For STM experiments, which required a higher level of cleanliness, the sample was the given a second SC2 clean, which produced a thin (~10 Å) oxide layer on the surface. This layer was then removed with a 15 sec immersion in BOE to produce a H-terminated starting surface.

2.2. Surface Infrared Spectroscopy

Infrared spectroscopy is capable of identifying the surface adsorbated as well as the nature of their bonding. The primary consideration in surface infrared spectroscopy, however, is the signal-to-noise ratio since the concentration of atoms on a typical surface is only ~10^{15} atoms/cm^2 (≃10^{-8} moles/cm^2). To enhance the signal from such a low concentration, an experimental geometry with a high surface electric field and multiple interactions of the beam with the adsorbates is highly desirable. For infrared-transparent substrates, the multiple-internal-reflection (MIR) geometry, originally developed by Harrick in 1960,[7] combines both of these conditions to give a high signal-to-noise ratio. This geometry was used for most experiments. Due to the limited spectral range of the MIR geometry for Si substrates (*vide infra*), the transmission geometry was also employed in some experiments. The two geometries are discussed in Section 2.2.1. Using a knowledge of surface electric fields in the MIR geometry, the polarized infrared spectra were decomposed into their Cartesian components as described in Section 2.2.2. This deconvolution simplified the spectra and revealed additional information about the orientation of surface bonds.

2.2.1. Experimental Geometries

The experimental MIR geometry is shown in Fig. 2.1(a). The samples were cut from 500-μm-thick, double-side-polished silicon wafers into 0.6″ × 1.5″ rectangles, the two short ends of which were polished into 45° bevels. The infrared beam from the spectrometer was focused on one beveled face at normal incidence and was then totally

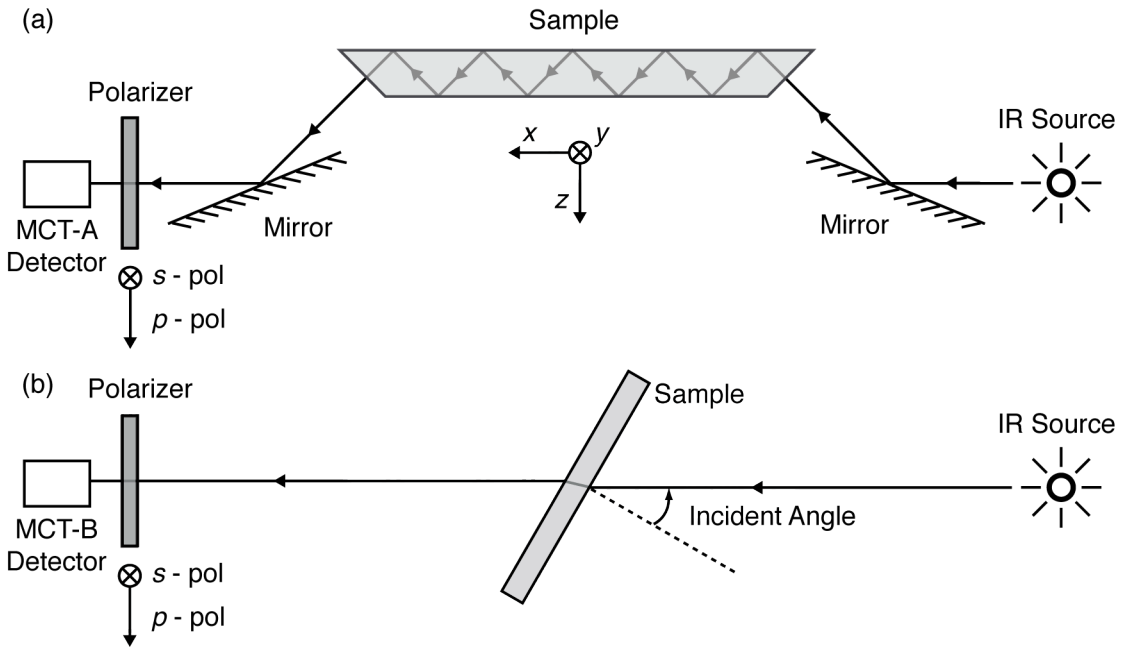

Figure 2.1. Apparatus for recording polarized infrared absorption spectra in (a) MIR geometry and (b) transmission geometry.

internally reflected ~75 times within the sample before exiting the opposite bevel. The beam then passed though a ZnSe wire-grid polarizer (Molectron), which transmitted either the *p*-polarized (electric field in the plane of incidence) or the *s*-polarized (electric field perpendicular to the plane of incidence) radiation. The light was then detected with a liquid-N_2-cooled mercury-cadmium-telluride detector (MCT-A, Thermo Scientific). The spectral measurements were performed with a Fourier-transform infrared (FTIR) spectrometer (Nexus 670, Thermo Nicolet). Since free carriers and certain impurities in the bulk Si absorb in the infrared region,[8,9] wafers of low doping level (*p*-type, resistivity >1000 Ω cm) and low carbon and oxygen impurity levels, obtained by float-zone processing, were used for the MIR experiments.

In the MIR geometry, internal reflection of radiation at the surface allows vibrational modes polarized parallel and perpendicular to the surface to be probed with comparable sensitivity and with a signal-to-noise ratio much better than the more common external reflection and transmission geometries.[10]

For Si surfaces, the MIR geometry works exceptionally well above 1500 cm^{-1}, a region that includes the important Si-H stretch vibrations. Multiphonon absorption of bulk silicon[9] attenuates most of the radiation below 1500 cm^{-1}. As a result, the MIR geometry cannot be used to study low energy vibrations, such as Si-H bending modes.

For the spectral region below 1500 cm^{-1}, the transmission geometry, shown in Fig. 2.1(b), was used. In this geometry, the much shorter path length of the light in the sample significantly reduces absorption by bulk Si. The same samples were used for both geometries (although the edge beveling was not required in transmission). The *p*-polarized spectra were recorded at a 74° angle of incidence, which was near Brewster's angle for silicon. At Brewster's angle, *p*-polarized radiation is completely transmitted,[11] which minimizes baseline distortions due to interference.[12] This incidence angle represents a compromise between the high angle that maximizes the normal component of the surface electric field and the smaller angle needed for complete transmission of the ~6-mm-diameter infrared beam. Similarly, transmittance of *s*-polarized radiation is maximum at normal incidence and decreases monotonically with increasing angle of incidence;[11] however, normal incidence produces large interference fringes in the spectra.[12] To balance these competing effects, the *s*-polarized spectra were recorded at 30° incidence. A MCT-B detector (Thermo Scientific) was used for transmission measurements because of its high sensitivity in the 500 - 700 cm^{-1} region.

2.2.2. Deconvolution of Absorption Spectra Obtained in MIR Geometry

Due to orientation of the respective electric fields, *s*-polarized radiation only probes the components of the vibrations oriented along the *y*-direction (as defined in Fig. 2.1), whereas *p*-polarized radiation probes components in both the *x*- and *z*-directions. The *x*- and *z*-components of the vibrations, therefore, cannot be independently determined from the two polarized spectra without further processing. Using a knowledge of surface electric fields, the components of the spectra along all

three Cartesian directions can be obtained from the raw polarized spectra. For complex spectra with overlapping bands, this deconvolution process can lead to significant spectral simplification, particularly when the Cartesian axes are aligned with the high-symmetry directions of the surface.

The infrared absorbance A of an adsorbate is given by

$$A = a\,(\mathbf{E} \cdot \boldsymbol{\mu})^2, \tag{2.1}$$

where $\mathbf{E}$ is the local electric field at the adsorbate, $\boldsymbol{\mu}$ is the transition dipole moment of the vibrational mode, and a is a proportionality constant. The local electric field at the adsorbate is different than the incident electric field. The simplest model for calculating the local electric field at a surface is known as the two-layer model, shown in Fig. 2.2(a). In this model, the substrate is separated from the vacuum by a sharp planar boundary. The adsorbates are assumed to reside in the vacuum layer. The electric fields at the interface can be derived using classical electrodynamics.[10,13] Here, the substrate is assumed to be isotropic, which leads to the well-known Fresnel equations, but the field calculations can be extended to anisotropic substrates. For p-polarized incident radiation, as sketched in Fig. 2.2(a), the electric field on the vacuum side of the

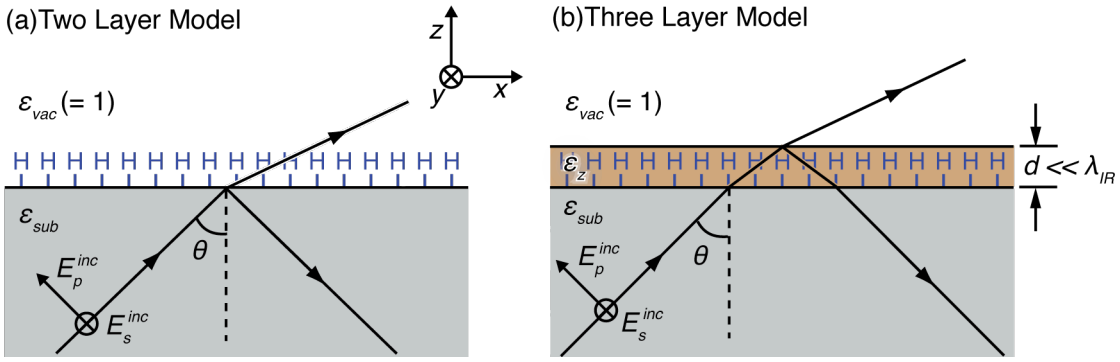

Figure 2.2. Schematic representation of internal reflection at an adsorbate-covered surface for p- and s-polarized radiation in (a) two-layer model and (b) three-layer model. The transmitted beam [and reflection in adsorbate layer in (b)] is shown for completeness for generalized angle θ. In the case of total internal reflection, the vacuum field is purely evanescent in nature, and decays exponentially with distance from the surface.

interface has parallel and perpendicular components, $E_{\parallel}$ and $E_{\perp}$, respectively, with magnitudes

$$E_{\parallel} = 2E_p^{inc}\cos\theta\sqrt{\frac{\sin^2\theta - 1/\varepsilon_{sub}}{(1-1/\varepsilon_{sub})[(1+1/\varepsilon_{sub})\sin^2\theta - 1/\varepsilon_{sub}]}}, \text{ and} \tag{2.2}$$

$$E_{\perp} = 2E_p^{inc}\sin\theta\frac{\cos\theta}{\sqrt{(1-1/\varepsilon_{sub})[(1+1/\varepsilon_{sub})\sin^2\theta - 1/\varepsilon_{sub}]}}, \tag{2.3}$$

where E_p^{inc} is the magnitude of the incident electric field, θ is the angle of incidence, and ε_{sub} is the substrate dielectric constant (assumed to be isotropic). For *s*-polarized incident radiation, as sketched in Fig 2.2(a), the electric field E_s on the vacuum side of the interface is parallel to the surface, with a magnitude given by

$$E_s = 2E_s^{inc}\frac{\cos\theta}{\sqrt{(1-1/\varepsilon_{sub})}}, \tag{2.4}$$

where E_s^{inc} is the magnitude of the incident electric field. The two-layer model does not include the optical response of the adsorbates and has been found inaccurate in several quantitative spectral studies.[13,14]

The three-layer model[10,15,16] corrects this deficiency and includes the optical response of the adsorbates. This model, illustrated in Fig. 2.2(b), defines the system in terms of three media − the bulk substrate, an infinitesimally thin adsorbate layer, and the vacuum − separated by sharp planar boundaries. Since the adsorbates are often *oriented* on a surface, the dielectric response of the adsorbate layer is expected to be anisotropic. For simplicity, the dielectric tensor of the adsorbate layer is assumed to be diagonal with principal axes along *x*, *y*, and *z*. The continuity of the parallel components of the electric field across the vacuum/adsorbate interface requires

$$E_s^{ad} = E_s, \text{ and} \tag{2.5}$$

$$E_{\|}^{ad} = E_{\|}, \tag{2.6}$$

where E_s^{ad} and $E_{\|}^{ad}$ are the *s*-polarized electric field and the parallel component of *p*-polarized electric field, respectively, in the adsorbate layer. [Since the adsorbate layer is infinitesimally thin (~ 1.5 Å), the electric field within the adsorbate layer is assumed to be constant.] Similarly, the normal component of the displacement field must be continuous across the vacuum/adsorbate layer interface, which implies

$$\varepsilon_z E_{\perp}^{ad} = E_{\perp}, \tag{2.7}$$

where $E_{\perp}^{ad}$ is the perpendicular component of *p*-polarized radiation in the adsorbate layer, and ε_z is the *z*-component of the adsorbate layer dielectric tensor (assumed diagonal). As a result, the electric field components at adsorbates in the three-layer model E_s^{ad}, $E_{\|}^{ad}$, and $E_{\perp}^{ad}$ are given by E_s, $E_{\|}$, and $E_{\perp}/\varepsilon_z$, respectively. In essence, the adsorbate layer screens the normal component of the electric field by a factor of ε_z, but has no effect on the in-plane components of the field.

The accuracy of discrete dielectric layer models for surface field calculations has been extensively reviewed by Feibelman,[17] who found two fundamental problems with such models. First, in reality the electric fields at the surface are not just determined by the local dielectric response of the adsorbates but also by the response of nearby atoms and molecules. Second, the sharp discontinuity of the surface normal electric field is unrealistic, because it implies charge localization at the boundary over sub-atomic distances. Feibelman concluded that if the frequency is well below the substrate plasma frequency and surface layer absorption is small, local dielectric models are adequate for the calculations of surface fields. The power absorption of thin adsorbate monolayers on surfaces is small (typical absorbance of a monolayer $\lesssim 10^{-4}$). Insulators and undoped semiconductors have plasma frequency in the far-ultraviolet region.[18,19] For these materials, the three-layer model can be adequately used for surface infrared spectroscopy.

Using the local electric fields calculated from the three-layer model (Eqns. 2.5 - 2.7), the absorbances of *p*- and *s*-polarized radiation in the MIR geometry can be expressed using Eqn. 2.1 as

$$A_p = a \sum_{\text{all reflections}} [E_{\parallel}(\mathbf{r}_k)\mu_x(\mathbf{r}_k) + E_{\perp}(\mathbf{r}_k)\mu_z(\mathbf{r}_k)/\varepsilon_z]^2, \text{ and} \tag{2.8}$$

$$A_s = a \sum_{\text{all reflections}} E_s(\mathbf{r}_k)^2 \mu_y(\mathbf{r}_k)^2, \tag{2.9}$$

where $\mu_x(\mathbf{r}_k)$, $\mu_y(\mathbf{r}_k)$, and $\mu_z(\mathbf{r}_k)$ are the Cartesian components of the transition dipoles for the adsorbates at $\mathbf{r}_k$, the position of the k^{th} reflection. Every reflection of *p*-polarized radiation at the surface leads to a relative phase shift between *x* and *z* components.[20] Assuming the electric field samples the same distribution of $\boldsymbol{\mu}$ at every reflection, the cross terms in Eqn. 2.8 average to zero over the entire sample, and the summation over all reflections can be absorbed in the constant to yield the equations

$$A_p = cE_{\parallel}^2\mu_x^2 + cE_{\perp}^2\mu_z^2/\varepsilon_z^2, \text{ and} \tag{2.10}$$

$$A_s = cE_s^2\mu_y^2, \tag{2.11}$$

where μ_x, μ_y, and μ_z are the Cartesian components of the surface transition dipole, and *c* is a constant.

The three components of the transition dipoles cannot be uniquely determined from the two equations 2.10 and 2.11. To solve these equations, more information is required.

A. Surfaces with macroscopic symmetry

Some surfaces have a macroscopic symmetry such that

$$\mu_x^2 = \mu_y^2. \tag{2.12}$$

For example, the H/Si(100) surface has two-fold rotational symmetry, but alternate terraces are rotated by 90º with respect to each other. Thus, the H/Si(100) surface has four-fold rotational symmetry on a macroscopic scale, making the *x*- and *y*-directions equivalent. Another example is that of surfaces with three-fold rotational symmetry,

which do not have microscopically equivalent *x*- and *y*-directions, but averaging of the squares of transition dipole components along *x*- and *y*-directions leads to Eqn. (2.12). For such surfaces, the system of equations (2.10) and (2.11) can be inverted to obtain

$$\mu_x^2 = \mu_y^2 = \frac{A_s}{cE_s^2}, \text{ and} \tag{2.13}$$

$$\frac{\mu_z^2}{\varepsilon_z^2} = \frac{E_s^2 A_p - E_\parallel^2 A_s}{cE_s^2 E_\perp^2}. \tag{2.14}$$

B. Surfaces lacking macroscopic symmetry

If the surface lacks any macroscopic symmetry, then μ_x and μ_y are not inherently related. In this case, *p*- and *s*-polarized spectra for the surface can be measured in two orthogonal propagation directions, as shown in Fig. 2.3. In practice, this is achieved by collecting spectra on two different samples cut in orthogonal directions. If the two geometries (Fig. 2.3) have equal path length, then the absorbances of *p*- and *s*-polarized spectra taken in the two geometries, A_{p1}, A_{s1}, A_{p2}, and A_{s2}, respectively, can be written

$$\begin{pmatrix} A_{p,1} \\ A_{s,1} \\ A_{p,2} \\ A_{s,2} \end{pmatrix} = c \begin{pmatrix} E_\parallel^2 & 0 & E_\perp^2 \\ 0 & E_s^2 & 0 \\ 0 & E_\parallel^2 & E_\perp^2 \\ E_s^2 & 0 & 0 \end{pmatrix} \begin{pmatrix} \mu_x^2 \\ \mu_y^2 \\ \frac{\mu_z^2}{\varepsilon_z^2} \end{pmatrix}. \tag{2.15}$$

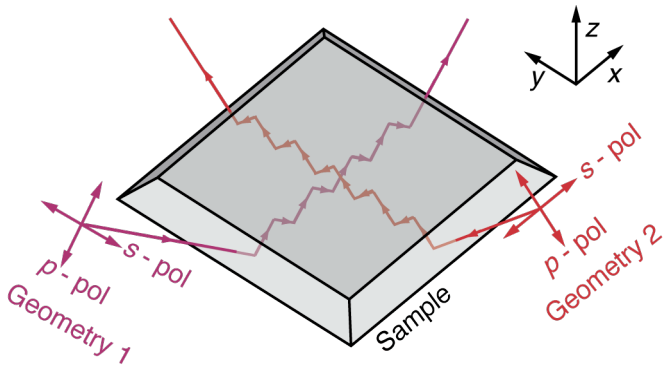

Figure 2.3. Measuring spectra of a sample in two orthogonal directions, shown as geometries 1 and 2, respectively, in both *p*- and *s*-polarization.

This equation is over-determined for the quantities μ_x^2, μ_y^2 and μ_z^2/ε_z^2. A *unique* best-fit solution to Eqn. 2.15 is obtained from the Morse-Penrose inverse of the coefficient matrix to give

$$\begin{pmatrix} \mu_x^2 \\ \mu_y^2 \\ \mu_y^2/\varepsilon_z^2 \end{pmatrix} = \frac{1}{c} \begin{pmatrix} \frac{E_\parallel^2}{2(E_\parallel^4+E_s^4)} & \frac{E_\parallel^4}{2E_s^2(E_\parallel^4+E_s^4)} & \frac{-E_\parallel^2}{2(E_\parallel^4+E_s^4)} & \frac{E_\parallel^4+2E_s^4}{2E_s^2(E_\parallel^4+E_s^4)} \\ \frac{-E_\parallel^2}{2(E_\parallel^4+E_s^4)} & \frac{E_\parallel^4+2E_s^4}{2E_s^2(E_\parallel^4+E_s^4)} & \frac{E_\parallel^2}{2(E_\parallel^4+E_s^4)} & \frac{E_\parallel^4}{2E_s^2(E_\parallel^4+E_s^4)} \\ \frac{1}{2E_\perp^2} & \frac{-E_\parallel^2}{2E_\perp^2E_s^2} & \frac{1}{2E_\perp^2} & \frac{-E_\parallel^2}{2E_\perp^2E_s^2} \end{pmatrix} \begin{pmatrix} A_{p1} \\ A_{s1} \\ A_{p2} \\ A_{s2} \end{pmatrix}. \quad (2.16)$$

Using Eqn. 2.16, the three Cartesian components of the transition dipole moments can be extracted from the polarized infrared spectra of the surface. In this method, the relative magnitudes of the two in-plane components can be obtained exactly, but surface normal component is scaled by a factor of ε_z^2 — a typically unknown quantity. The value of ε_z is not essential for the deconvolution process and is needed only for the determination of absolute orientation of the modes that have both surface normal and in-plane components.

This deconvolution method has been verified on the spectra of H/Si(110) surfaces.[14] The chemical structure of this surface is well understood, and the deconvoluted spectral components were fully consistent with the geometry of vibrational modes for the surfaces.

2.3. Scanning Tunneling Microscopy

Scanning tunneling microscopy (STM) is a technique that can image atomic scale surface topography of conducting samples. In this technique, a voltage bias is applied between the sample and a conducting tip, and the tunneling current between the two is used to probe the surface atoms. To obtain three-dimensional topography of the surface, the tip is the scanned across the surface keeping the tunneling current constant with a feedback circuit. The variations in tip height across the surface represent the

morphology of the surface. This mode of scanning, also known as constant current mode, was used to obtain all STM images.

A custom, Besocke-type[21] STM housed in an ultra-high vacuum (UHV) chamber with a base pressure of ~10^{-10} Torr was used for all experiments. The chamber was evacuated with a turbomolecular pump and an ion pump, with an initial baking of the chamber at ~110ºC for ~14 hr during the pump down stage. (The ion pump was turned off during the STM imaging, since the ions emitted from the pump can degrade the sample surfaces.) The main UHV chamber was connected to a hydrocarbon-free loadlock, which was evacuated sequentially by a liquid-N_2-cooled cryopump to a pressure of ~10^{-2} Torr and a turbo pump to a pressure of ~10^{-8} Torr. The complete UHV chamber rested on a vibration isolation system (Newport, Elite 3 active isolation system). Details of the STM design, UHV chamber and its control system have been documented elsewhere.[22-24]

The tips used for scanning were prepared by electrochemical etching of tungsten wire in aqueous KOH solution. These tips were then annealed *in-situ* inside the UHV chamber by field emission from a thoriated tungsten filament to clean-off any organics and metal oxide from the tip surface. Details of tip preparation and cleaning have been documented elsewhere.[22,23]

High conductivity silicon samples for stable tunneling were obtained from P-doped Si wafers with resistivity 0.5-10 Ω cm. After etching, the sample was transferred to a custom Teflon holder, and an InGa eutectic alloy was applied to the backside of the sample to facilitate good ohmic contact with the STM sample holder. The sample was then immediately loadlocked into the UHV chamber for STM imaging. The samples were typically imaged at a bias in the range -2.3 V to -2.8 V and a tunneling current in the range 0.26 nA to 0.32 nA.

A slight modification was made to the leg piezo controller circuit of the STM to prevent sporadic instabilities due to excessive current demands on the power operational amplifiers (PA-15, Apex Microtech.). The operational amplifiers were drawing a net current of up to ~24 mA near saturation, whereas the power supplies (± 200 V) were rated at 12 mA. This problem was addressed by increasing the values of input and feedback resistors while keeping the gain constant. The circuit diagram for the updated leg piezo controller is included in Appendix A.

REFERENCES

[1] H. Morinaga, M. Suyama, and T. Ohmi, J. Electrochem. Soc. **141**, 2834 (1994).

[2] B. C. Chung, G. A. Marshall, C. W. Pearce, and K. P. Yanders, J. Electrochem. Soc. **144**, 652 (1997).

[3] A. Ogura, J. Electrochem. Soc. **138**, 807 (1991).

[4] P. Jacob, P. Dumas, and Y. J. Chabal, Appl. Phys. Lett. **59**, 2968 (1991).

[5] W. Kern and D. A. Puotinen, RCA Rev. **31**, 187 (1970).

[6] A comprehensive review of standard Si cleaning procedures and their effectiveness can be found in W. Kern, *Handbook of Silicon Wafer Cleaning Technology* (2nd Edition), edited by K A. Reinhardt, and W. Kern (William Andrew Publishing, Norwich, NY, 2008), Chap. 1.

[7] N. J. Harrick, J. Phys. Chem. **64**, 1110 (1960).

[8] W. Spitzer and H. Y. Fan, Phys. Rev. **108**, 268 (1957).

[9] M. M. Pradhan, R. K. Garg, and M. Arora, Infrared Phys. **27**, 25 (1987).

[10] Y. J. Chabal, Surf. Sci. Rep. **8**, 211 (1988).

[11] Angle dependence of reflectance and transmittance at interface can be obtained using Fresnel equations. For air/silicon interface, this calculation can be found in V. P. Tolstoy, I. V. Chernyshova, V. A. Skryshevsky, *Handbook of Infrared Spectroscopy of Ultrathin Films*, (John Wiley and Sons, Hoboken, NJ, 2003), p. 30.

[12] V. P. Tolstoy, I. V. Chernyshova, V. A. Skryshevsky, *Handbook of Infrared Spectroscopy of Ultrathin Films*, (John Wiley and Sons, Hoboken, NJ, 2003), p. 79.

[13] Y. J. Chabal, in *Semiconductor Interfaces: Formation and Properties*, edited by G. LeLay, J. Derrien, and N. Boccara, Springer Proc. Phys. No. 22 (Springer, Berlin, 1987), p. 301.

[14] I. T. Clark, B. S. Aldinger, A. Gupta, and M. A. Hines, J. Chem. Phys. **128**, 144711 (2008).

[15] J. D. E. McIntyre and D. E. Aspnes, Surf. Sci. **24**, 417 (1971).

[16] A. N. Parikh and D. L. Allara, J. Chem. Phys. **96**, 927 (1992).

[17] P. J. Feibelman, Prog. Surf. Sci. **12**, 287 (1982).

[18] C. Kittel, *Introduction to Solid State Physics* (7th Edition), (John Wiley and Sons, Inc., New York, 1996), p. 278.

[19] I. Egri, Sol. St. Comm. **44**, 563 (1982).

[20] E. Hecht, *Optics* (3rd Edition), (Addison Wesley, Reading, MA, 1998), p. 116.

[21] K. Besocke, Surf. Sci. **181**, 145 (1987).

[22] T. A. Newton, Ph.D. Dissertation, Cornell University, 2000.

[23] S. P. Garcia, Ph.D. Dissertation, Cornell University, 2004.

[24] I. T. Clark, Ph.D. Dissertation, Cornell University, 2008.

Chapter 3

Aqueous NH_4F Etching of Si(100) and Formation of Near-Atomically-Flat Surface

3.1. Introduction

The fabrication of an integrated circuit involves 500-800 sequential steps, out of which 15% - 20% of the steps are wet cleaning.[1] The principal constituent of the cleaning solutions is often HF or buffered HF. Although primarily used for cleaning wafers, these solutions also increase surface roughness, which in turn degrades the performance of the fabricated devices.[2,3] An ideal cleaning solution would be one that both cleans the surface and produces an atomically smooth morphology. For Si(111), a perfect etchant of this type was found by Higashi *et al.*[4] in 1990 — 40% NH_4F (aq.). Interestingly, the smoothness of the etched morphology was not identified by microscopy, but rather from the infrared spectrum of the etched surface, which displayed a single sharp Si-H stretch band with a linewidth of 0.9 cm^{-1} (0.1 cm^{-1} at T = 130 K)[5] — the narrowest linewidth ever observed for a covalently-bonded adsorbate on a surface. This narrow linewidth is a manifestation of the unprecedented atomic-scale homogeneity of the surface. This discovery, later confirmed by scanning tunneling microscopy (STM),[6] was an important milestone in the field of surface science for two reasons. First, the morphological control was the result of an extremely simple aqueous solution. Second, this result and a series of experiments that followed[7-10] demonstrated the power of infrared spectroscopy in determining the local chemical structure of surfaces.

Since Si(100) is the substrate of choice in the microelectronics industry, the observation of atomically-flat etched Si(111) sparked an intense search for an etchant

that could similarly smooth the Si(100) surface. In spite of research efforts by scores of groups around the world, such an etchant remained elusive for almost two decades.

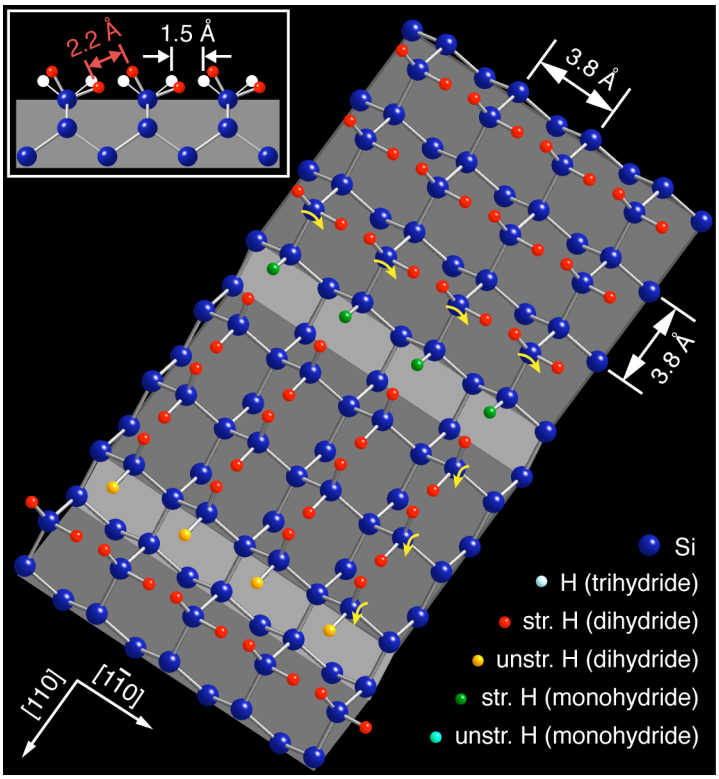

Figure 3.1. Structure of the ideal H/Si(100) surface. (Inset) Side view of a H/Si(100) terrace showing the predicted canting of strained dihydrides. The bulk-terminated positions of the surface atoms are shown in white. The color scheme classifies H atoms on the basis of their bonding (monohydride, dihydride, trihydride) and inter-adsorbate strain. The same scheme is used throughout this chapter.

The first and most obvious candidate for a "perfect" Si(100) etchant was NH_4F itself; however, the infrared spectrum of Si(100) etched in aqueous NH_4F, as well as other HF based etchants, displayed multiple broad bands in the Si-H stretch region.[11-16] Ideal flat terraces on the H/Si(100) surface would have complete dihydride termination, as shown in Fig. 3.1, and thus two infra-red active Si-H stretch modes corresponding to the symmetric and antisymmetric vibrations of the dihydrides. Cluster simulations[11] suggested that the multiple broad bands were due to an heterogeneous (rough) surface terminated with mono-, di-, and trihydrides. This interpretation served as the

unquestioned basis for all subsequent infrared analyses of etched H/Si(100) surfaces. Characterization of the NH_4F (aq.) etched Si(100) surface using high-resolution electron energy loss spectroscopy (HREELS)[17] suggested that this surface had a high density of dihydrides and monohydrides, but few trihydrides. Thermal desorption spectroscopy and reflection high-energy electron diffraction (RHEED) studies[18] indicated that prolonged etching of the surface (~10 min) in NH_4F decreased the density of dihydrides and increased the density of monohydrides. The general consensus[19] that emerged from these experiments was that aqueous NH_4F and other HF-based etchants progressively roughen Si(100) surfaces, in part by producing slow-etching (111) microfacets that are covered with monohydrides. Contrary to these conclusions, this chapter shows that aqueous etchants — in this case, NH_4F itself — *can* produce near-atomically-flat H/Si(100) surfaces.

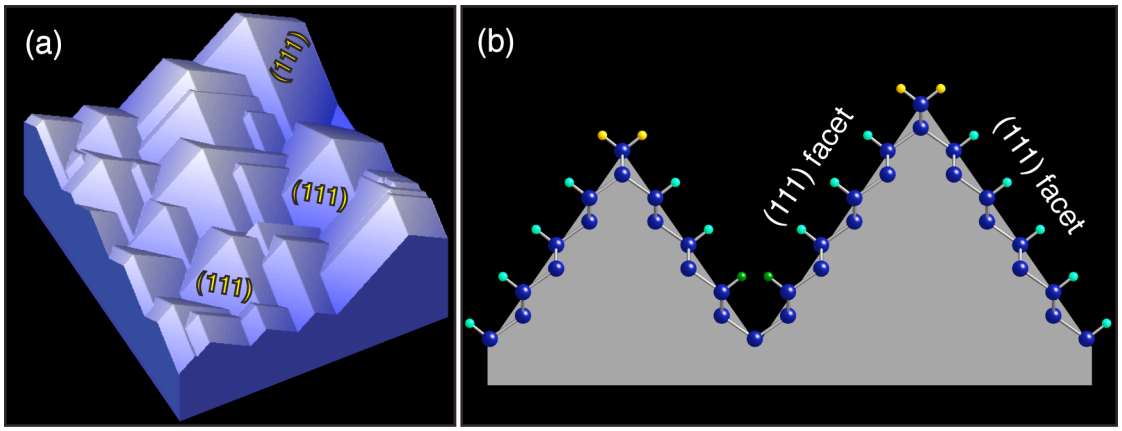

Figure 3.2. (a) A H/Si(100) surface covered with {111}-faceted hillocks. (b) Atomic structure of the hillocks in (a) shown in a cross section along the ⟨110⟩ direction.

Inter-adsorbate stress on H/Si(100) arises from the close proximity of H atoms on adjacent dihydrides. On the bulk-terminated surface, as shown in the inset of Fig. 3.1, the distance between H atoms on neighboring dihydrides would be 1.51 Å, which is much less than the 2.4 Å van der Waals diameter of H,[20,21] leading to severe steric strain. Simulations[22-25] predict the canting of these dihydrides, as illustrated in Fig. 3.1,

to increase the inter-hydride distance, thereby reducing the inter-adsorbate strain. Flat H/Si(100) terraces, however, have not been observed experimentally over extended regions. A microfaceted H/Si(100) surface, such as shown in Fig. 3.2, would have much lower inter-adsorbate stress than a flat surface; however, this chapter shows that microfaceting is not inherent to the NH_4F etching of H/Si(100).

This chapter describes the formation of near-atomically-flat H/Si(100) by room-temperature etching in 40% NH_4F (aq.) solution. The infrared spectrum of the etched surface was identical to that previously reported, however, a new deconvolution technique reconciled the band assignments with the surface morphology. Etching of the surface was accompanied by the evolution of H_2 bubbles, which transiently attached to the surface. If the bubbles were periodically removed from the etching surface, a near-atomically-flat surface was produced. On the other hand, if the bubbles were allowed to collect on the surface, the etched surface developed roughness visible to the naked eye. The role of bubbles in surface roughening is discussed in Chapter 4.

3.2. Experimental

For STM studies, 0.6″ × 0.7″ samples were diced from 500-μm-thick, single-side-polished, Cz-grown wafers (P-doped, resistivity 0.5-10 Ω cm), cut to within 0.9° of the (100) orientation or 3.5° ± 0.1° from the (100) orientation using the procedures described in Chapter 2. For infrared spectroscopy, 0.6″ × 1.5″ samples were diced from 500-μm-thick, double-side-polished, float-zone wafers (p-type, resistivity >1000 Ω cm), cut to within 0.9° of the (100) orientation or 5° ± 0.9° from the (100) orientation. For multiple internal reflection (MIR) experiments, the two short sides of the sample were polished into 45° bevels.

All samples were thermally oxidized and annealed to obtain a ~1000 Å oxide layer as described in Chapter 2. After a standard RCA clean, the sample was immersed in buffered oxide etch (BOE, J. T. Baker, CMOS grade), consisting of 5:1 by volume of

40% NH_4F (aq.) and 50% HF (aq.), for 75 s to produce a H-terminated starting surface. The sample was then etched in room temperature, 40% NH_4F (aq., J. T. Baker, CMOS grade) for varying times. During the etch, the sample was periodically removed from the etchant every 15 s to dislodge any H_2 bubbles. After etching, the sample was rinsed for 15 s in ultra-pure water (Millipore Milli-Q). The etch morphology was then characterized by STM or infrared spectroscopy.

STM imaging of the etched surfaces was performed in ultra-high vacuum, as described in Chapter 2. A negative bias between -2.3 V and -2.8 V was applied to the sample, which was scanned at a constant tunneling current of 0.26 – 0.32 nA. (High-resolution images were sometimes obtained at 0.15 nA tunneling current.)

Infrared spectra of the etched samples were obtained with both *s*- and *p*-polarized radiation in both the multiple-internal-reflection (MIR) and transmission geometries using a dry-air-purged Nicolet 670 FTIR spectrometer as described in Chapter 2. The spectra were referenced to oxidized surfaces obtained *in-situ* by 20 min exposure of the samples to O_3, which was produced by using a Hg pen lamp inside the spectrometer chamber. Interference fringe, when observed, was removed computationally.[26]

3.3. Results

The atomic-scale morphology of a Si(100) surface etched in NH_4F (aq.) solution for 30 s is shown by the STM images in Fig. 3.3. This morphology was statistically invariant for etch times ranging from 30 s to 40 min. The surface was near-atomically-flat and was characterized by long rows typically separated by 7.7 Å — twice the distance between adjacent Si atoms on an ideal H/Si(100) terrace, as shown in Fig. 3.1. The long axis of the elliptical protrusions was oriented perpendicular to the row direction. Adjacent rows were separated by ~0.9-Å-deep grooves. The rows were aligned with either the $\langle 110 \rangle$ or $\langle 1\bar{1}0 \rangle$ directions; the row direction rotated by 90º on

successive terraces. The root-mean-square roughness of the 3000 Å × 1000 Å region shown in Fig. 3.3(c) was 0.81 Å.

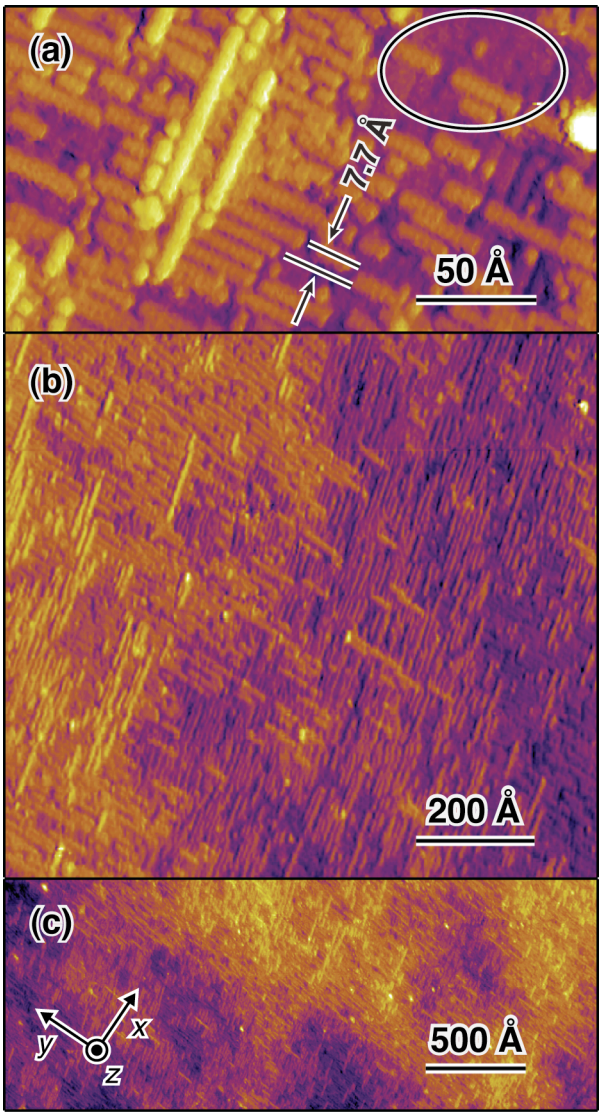

Figure 3.3. Three STM images of a Si(100) surface etched in room-temperature 40% NH_4F (aq.). The root-mean-square roughness of the region in (b) was 0.57 Å and in (c) was 0.81 Å. Some regions, such as the one highlighted by the ellipse in (a), had nearly-flat terraces with few long rows.

The row spacing of 7.7 Å was consistent with many possible atomic structures, some of which are shown in Fig. 3.4. The first possibility, shown in Fig. 3.4(a), was the well-known 2 × 1 reconstructed surface,[27] which is usually formed by the reaction of

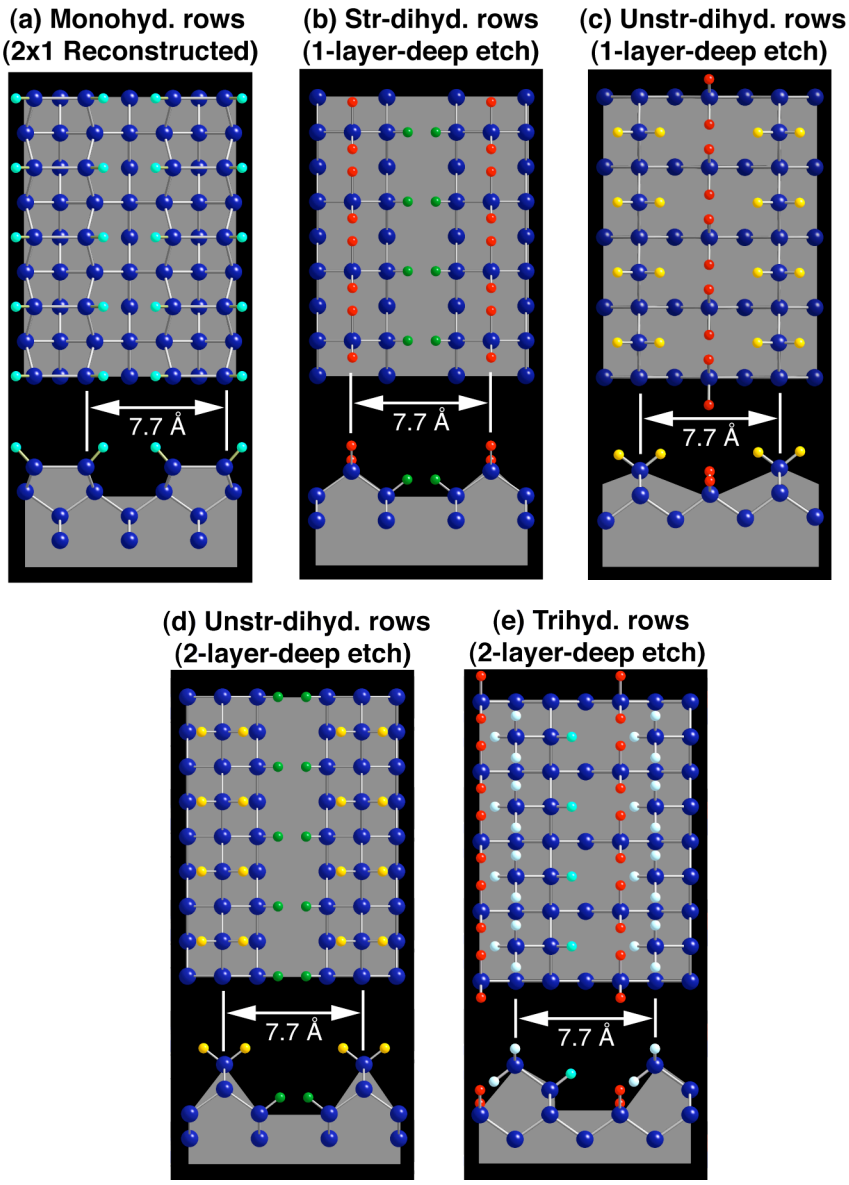

Figure 3.4. Possible atomic-scale structures consistent with the observed 7.7 Å row spacing. (a) 2 × 1 H/Si(100), (b) strained dihydride (Str. dihyd.) rows separated by single-layer-deep trenches of strained monohydrides, (c) unstrained dihydride (unstr. dihyd.) rows separated by single-layer-deep trenches of strained dihydrides, (d) unstrained dihydride rows separated by double-layer-deep trenches of strained monohydrides, and (e) trihydride (trihyd.) rows separated by trenches of strained dihydrides and unstrained monohydrides (monohyd.).

clean Si(100) – (2 × 1) surfaces with atomic hydrogen in ultra-high vacuum at high temperatures. Other possibilities were formed by etching every other row of Si atoms

from an unreconstructed H/Si(100) surface. Figures 3.4 (b - e) illustrate four such structures.

Structures formed by removing two layers of Si atoms, such as Fig. 3.4 (d) and (e), were inconsistent with the orthogonal rows of atoms observed on successive terraces in Fig. 3.3. As illustrated in Fig. 3.5, single-layer-deep etching of rows in the top terrace would allow the formation of orthogonal rows in the next terrace. The two-layer-deep etched rows, however, do not allow for this possibility.

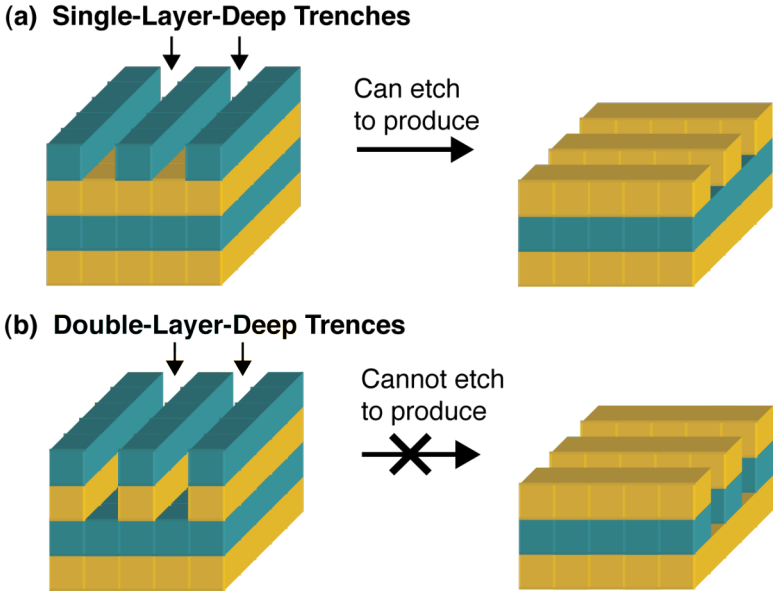

Figure 3.5. (a) Rows separated by single-layer-deep trenches can be etched to yield orthogonal rows, whereas (b) rows separated by double-layer-deep trenches cannot. Alternate layers are shown in different colors for clarity.

The chemical structure of the rows could not be established from the STM images; spectroscopic information was required. The Si-H stretch regions of the *s*- and *p*-polarized spectra of etched Si(100) are shown in Fig. 3.6 (a, b). These spectra were almost identical to those published by Dumas *et al.*[12] in 1992. Five broad, overlapping bands were observed in the Si-H stretch region; other spectral regions were featureless, including the regions corresponding to O-Si-H and Si-OH bands. The spectra were invariant for etch times ranging from 30 s to 40 min, consistent with the observed STM

images (*vide supra*). By comparison to previously published spectra,[28] the 2 × 1 reconstructed H/Si(100) structure [Fig. 3.4(a)] was conclusively ruled out.

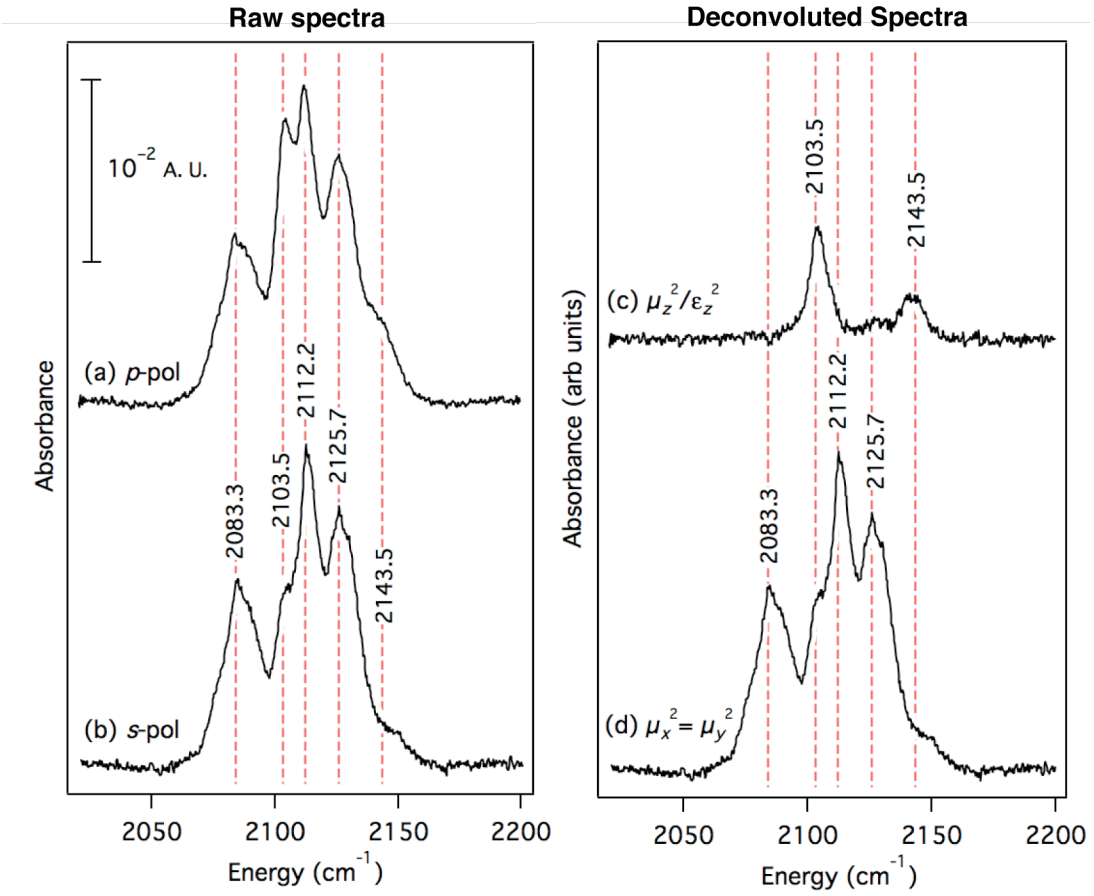

Figure 3.6. (a, b) The Si-H stretch region of the *p*- and *s*-polarized spectra of a NH_4F-etched, nominally-flat Si(100) surface obtained in the MIR geometry. (c, d) The in-plane and perpendicular components of the squared transition dipole moments extracted from the spectra in (a, b). The Cartesian axes are defined in Fig. 3.3.

Using the computational technique described in Chapter 2, these spectra were deconvoluted into in-plane and perpendicular components of the squared transition dipole moments, which are shown in Fig. 3.6 (c, d). Since H/Si(100) surfaces have a macroscopic four-fold symmetry, the *x* and *y* components of the transition dipole moments were identical. In spite of significant spectral simplification, the deconvoluted spectra of flat H/Si(100) surfaces were still too complicated for definitive interpretation.

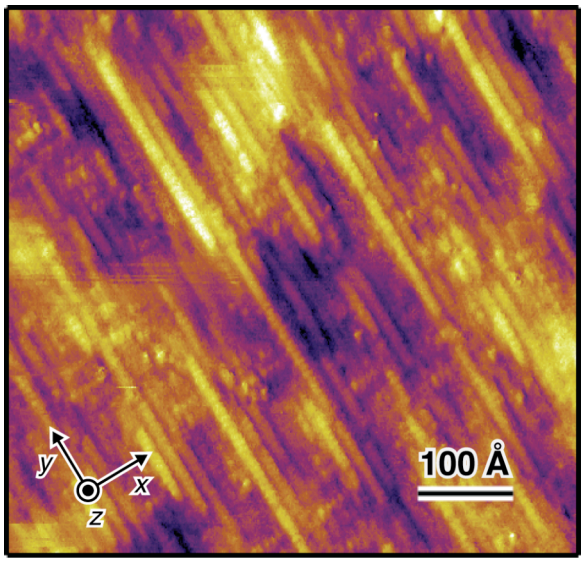

Figure 3.7. STM image of a NH_4F-etched Si(100) surface miscut by 3.5° towards the [011] direction showing the preferential formation of long rows parallel to the step edges.

Further information on the polarization of the in-plane modes was obtained from NH_4F-etched vicinal Si(100) surfaces. As shown in Fig. 3.7, when Si(100) surfaces miscut by 3.5° towards the [011] direction were etched in 40% NH_4F (aq.), the macroscopic four-fold symmetry was broken, and long rows of atoms were preferentially formed perpendicular to the miscut direction. Figure 3.8 shows the Cartesian components of the infrared spectrum of NH_4F-etched H/Si(100) miscut by 5º towards the [110] direction; the *x*, *y*, and *z* axes are defined in Fig. 3.7. The spectra displayed the same five bands as observed in the spectra of the nominally-flat surface, suggesting that same species were present on both surfaces. In addition, the sum of the *x*- and *y*-components in the miscut surface spectra was almost identical to twice the in-plane component of the nominally-flat surface spectra [Fig. 3.6(d)]. These similarities in the two spectra showed that the steps on the miscut surface did not introduce any new vibrational modes or change the relative densities of different species compared to the nominally-flat surface.

The polarization of the spectral bands in Fig. 3.8 and the STM images in Figs. 3.3 and 3.7 were only consistent with the missing-row morphology illustrated in Fig.

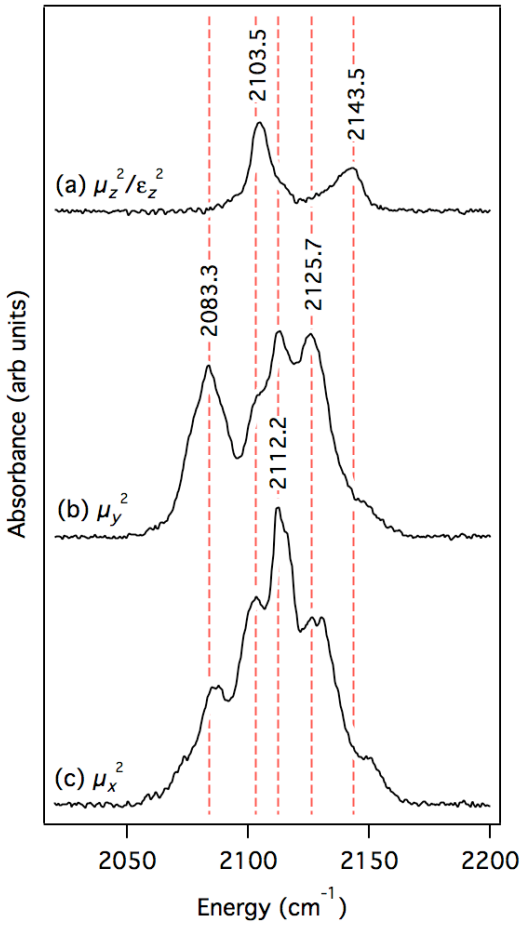

Figure 3.8. The Si-H stretch region of the Cartesian components of the squared transition dipole moments extracted from the polarized spectra of a NH_4F-etched Si(100) surface miscut by 5° towards the [011] direction. The Cartesian axes are defined in Fig. 3.7.

3.4(c); Fig. 3.9 shows the extended surface for this morphology along with the (assumed) structure of steps and row ends. The modes at 2103.5 cm^{-1} (*z*-polarized) and 2112.2 cm^{-1} (predominantly *x*-polarized) were assigned to the symmetric and the antisymmetric stretch vibrations, respectively, of unstrained dihydrides that decorated the long rows of Si atoms. This assignment was consistent with the observed polarization, the assignment of Dumas *et al.*,[12] and the 9-11 cm^{-1} splitting predicted for these modes by simulations.[29,30] The mode at 2083.3 was previously[12] assigned to the stretch vibrations of monohydrides; however, this assignment was inconsistent with the entirely in-plane polarization of this band. On a H/Si(100) surface, the Si-H bonds of

monohydride species are 54.5° from the surface normal. Their stretch vibration should therefore have comparable in-plane and normal components. Instead, the modes at 2083.3 cm^{-1} and 2143.5 cm^{-1} were attributed to the vibrations of the strained, canted dihydrides in the valleys between the rows. The predominantly *z*-polarized mode at 2143.5 cm^{-1} was assigned to the vibrations of the upward-pointing Si-H bond of canted dihydrides, whereas the predominantly *y*-polarized mode at 2083.3 cm^{-1} was assigned to the vibration of the nominally in-plane Si-H bond. This assignment was consistent with the observed polarization; however, the observed 60.2 cm^{-1} splitting was significantly smaller that the 100 cm^{-1} splitting predicted by recent DFT simulations.[25] In Chapter 5, new simulations that predict a mode splitting of 56 cm^{-1} are presented.

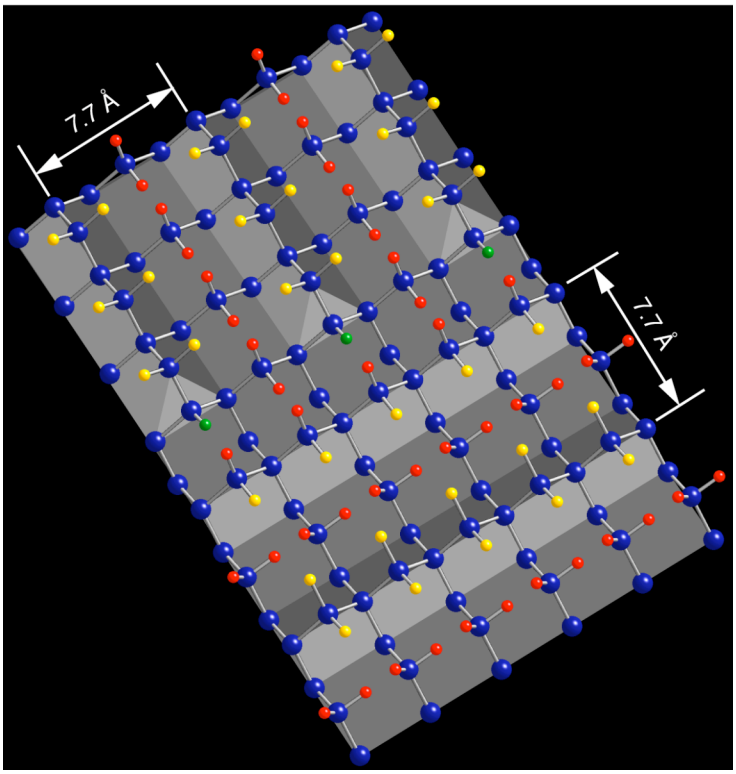

Figure. 3.9. Atomic structure of the NH_4F-etched H/Si(100) surface that is consistent with the STM and spectroscopic data. The terrace structure is identical to that in Fig. 3.4(c). The color scheme is given in Fig. 3.1.

The rows of unstrained dihydrides would presumably terminate in strained monohydrides as shown in Fig. 3.9. The band at 2125 cm^{-1} was tentatively assigned to the stretch mode of these strained monohydrides. Dumas *et al*.[12] had assigned the bands at 2125.7 cm^{-1} and 2143.5 cm^{-1} to the Si-H stretch modes of trihydrides; however, this assignment was inconsistent with the STM images in Fig. 3.3. Trihydrides would be imaged as double-layer-high protrusions on the surface; however, a significant density of such features was not observed. The relatively high energy of this mode in comparison to other (unstrained) monohydrides (such as those on H/Si(111) terraces) is attributed to interadsorbate strain. This hypothesis is supported by the DFT simulations presented in Chapter 5.

To confirm these assignments, spectra of the low-frequency Si-H bending and scissor modes were obtained in the transmission geometry. Figure 3.9 shows the transmission spectra in *s*- and *p*-polarizations for two NH_4F-etched surfaces: flat and vicinal Si(100) miscut by 9° toward the [011] direction. The spectrum of the vicinal Si surface was measured in two sample orientations as indicated by the insets to Fig. 3.10. Two broad, overlapping bands at 906.4 cm^{-1} and 917.0 cm^{-1} were observed in the dihydride scissor region on all *p*-polarized spectra; these two modes were assigned to scissor vibrations of the strained, canted and unstrained dihydrides, respectively. This assignment was consistent with the predicted mode ordering but slightly lower than the 19 cm^{-1} splitting predicted by the DFT simulations in Chapter 6.

In the Si-H wag region, spectra of flat NH_4F-etched Si(100) surface displayed a single band at 655.7 cm^{-1} as shown in Fig. 3.10(a). On NH_4F-etched vicinal Si(100) surfaces, this mode was resolved into two bands with different polarizations: a mode at 655.7 cm^{-1} polarized parallel to the surface steps (and the long atomic rows) and a mode at 659.6 cm^{-1} polarized perpendicular to the surface steps. On the basis of this characteristic polarization dependence, the modes at 655.7 and 659.6 cm^{-1} were

assigned to wag modes of the unstrained and the canted, strained dihydrides, respectively. This assignment was in good agreement with previous observations of dihydride wag modes at 655.5 cm^{-1} on H/Si(111) steps[10,31] and at 656 cm^{-1} on 3 × 1 reconstructed H/Si(100)[30] surfaces.

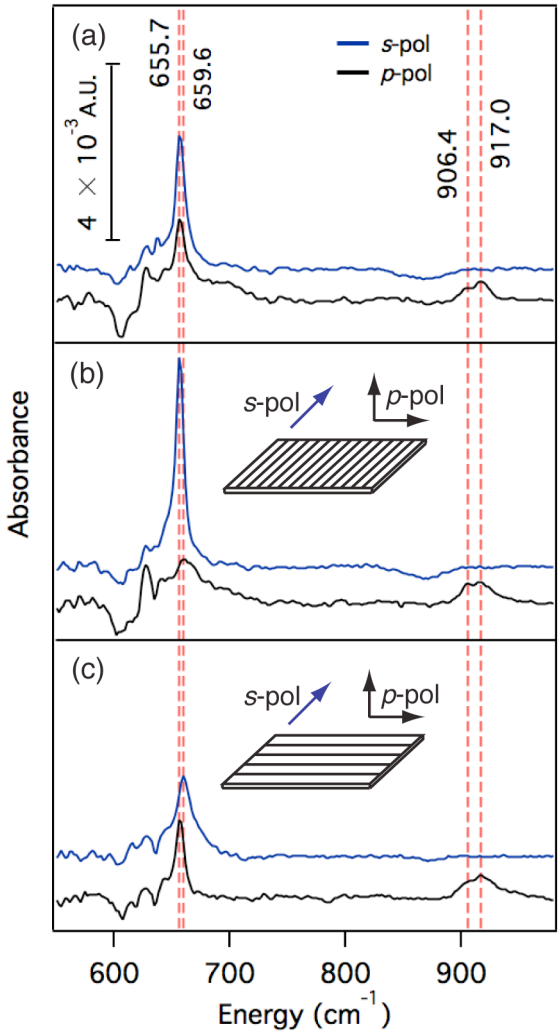

Figure 3.10. Transmission spectra of NH_4F-etched Si(100) surfaces in the Si-H wag and scissor region. (a) Spectra of a nominally-flat surface, (b) a 9° miscut surface with light propagating along the miscut direction, and (c) a 9° miscut surface with light propagating perpendicular to the miscut direction. The insets in (b, c) show the relative orientations of the vicinal steps and the electric field in both polarizations.

The missing-row structure, shown in Fig. 3.9, was also consistent with the orientation of the elliptical protrusions observed in the STM images of NH_4F-etched surfaces. Electronic structure calculations of H/Si(100)[24] suggest that dihydrides would be imaged as ellipses in STM with the long axis of the ellipses being parallel to the plane of the dihydride. This was consistent with the STM images in Figs. 3.3 and 3.7.

3.4. Discussion

These results conclusively prove that NH_4F (aq.) etching of Si(100) produces near-atomically-flat surfaces, at least when H_2 bubbles are removed from the etching surface. In addition to achieving the long-sought goal of producing near-atomically-smooth etched H/Si(100) surfaces, these results also contribute to the fundamental understanding of H/Si(100) and its aqueous etching.

The missing-row morphology on the NH_4F-etched surfaces was atomically smooth over extended regions with lower inter-adsorbate strain than the atomically-flat terraces. With alternating strained-dihydride and unstrained-dihydride rows, this morphology had about 50% less strain than an ideal H/Si(100) terrace. No microfaceting was observed even for etch times up to 40 min, showing that microfaceting is not inherent to the NH_4F etching of H/Si(100) and that the etching kinetics are not driven solely by surface strain minimization.

The missing-row motif was first suggested on the basis of a 2.2 nm × 2.2 nm STM image obtained by Endo *et al.*[24] on a HF-etched Si(100) surface. On the basis of theoretical surface energy calculations, they proposed a structure consisting of alternating unstrained-dihydride rows and strained-dihydride rows. No spectroscopic data, however, were obtained, and the atomic structure of the missing-row motif was not established.

Canting of strained dihydrides on the unreconstructed H/Si(100) surface has been predicted by several theoretical studies[22-25] based on surface energy calculations,

but this study provided the first experimental confirmation of these predictions. In addition, this study demonstrated the utility of the deconvolution technique discussed in Chapter 3 in the analysis of complex surface structures.

The surprisingly small line-width of the Si-H stretch mode on NH_4F-etched H/Si(111) surfaces led to the expectation that near-atomically-flat H/Si(100) surfaces would have similarly narrow Si-H stretch modes. This was not observed. Indeed, the near-atomically-flat H/Si(100) surfaces had unusually large linewidths. DFT calculations, presented in Chapter 5, show that point defects (vacancies) in the canted dihydride rows lead to large structural relaxations in the vicinity of the vacancy. These relaxations cause large shifts (up to 25 cm^{-1}) in the vibrational energies of nearby strained dihydrides. When averaged over an entire surface, point defects could lead to significant heterogeneous broadening. Consistent with this explanation, the spectrum of NH_4F-etched Si(100) showed little change down to at least -110 °C,[32] confirming the absence of significant homogenous broadening.

The NH_4F-etched H/Si(100) morphology also gave insights into the etch kinetics of the surface sites. Importantly, this morphology could not be explained by other models of anisotropic etching, such as step-flow etching or pit nucleation and growth. The production of long, single-atom-wide rows on the surface implies that row-end sites etch much more quickly than mid-row sites. This mechanism of row etching is supported by the Kinetic Monte Carlo (KMC) simulations of H/Si(100) surface etching presented in Chapter 5. To ascertain the exact mechanism of etching, investigations with KMC simulations are in progress.

The re-interpretation of the infrared spectra of NH_4F-etched H/Si(100) resolved several apparent discrepancies between the STM images presented here and previous analyses of the etched surface. Nevertheless, the reported increase in the density of monohydride species with etch time[13,18] are entirely inconsistent with the surfaces

studied in these experiments. This apparent discrepancy is resolved in Chapter 4, where the effects of H_2 bubbles — a reaction product — on the etch morphology are explored.

Two modes in the spectrum of NH_4F-etched Si(100) are missing from the assignment: the two (presumably non-degenerate) bend modes of the strained monohydride species, seen in Fig. 3.9, that terminate the dihydride rows. (The Si-H stretch vibration at 2125.7 cm^{-1} was tentatively ascribed to this species). The Si-H bend of unstrained monohydrides is observed at 626.7 cm^{-1} on H/Si(111);[31] however, the energy of the strained monohydride bend could not be accurately predicted by the DFT simulations presented in Chapter 5. One possibility is that the two strained monohydride bending modes were obscured by baseline noise, which is primarily due to fluctuations in phonon population caused by a small thermal instability. The second, perhaps less likely, possibility is that these bands were obscured by the more intense dihydride wag modes.

3.5. Conclusions

Near-atomically-flat, H-terminated Si(100) surfaces were produced by etching in 40% NH_4F (aq.) solution. The etch morphology reached steady state rapidly and was statistically invariant for etch durations of 30 s to 40 min provided the H_2 bubbles formed on the surface were periodically removed. The infrared spectrum of NH_4F-etched H/Si(100) was identical to that previously reported by Dumas *et al.*;[12] however, the spectrum was reassigned on the basis of polarization data obtained from a new spectral deconvolution technique. On the basis of the infrared analysis and the STM data, the atomic structure of the etched surface was deduced. The etch morphology had extended terraces with alternating long rows of strained and unstrained dihydrides and had ~50% less interadsorbate strain than the ideal flat H/Si(100) terraces.

REFERENCES

[1] W. Kern, *Handbook of Silicon Wafer Cleaning Technology* (2nd Edition), edited by K. A. Reinhardt and W. Kern (William Andrew Publishing, Norwich, NY, 2008), p. 14.

[2] T. Ohmi, K. Kotani, A. Teramoto, and M. Miyashita, IEEE Electron Device Lett. **12**, 652 (1991).

[3] R. Kuroda, T. Suwa, A. Teramoto, R. Hasebe, S. Sugawa, and T. Ohmi, IEEE Trans. Elec. Dev. **56**, 291 (2009).

[4] G. S. Higashi, Y. J. Chabal, G. W. Trucks, and K. Raghavachari, Appl. Phys. Lett. **56**, 656 (1990).

[5] P. Dumas, Y. J. Chabal, and G. S. Higashi, Phys. Rev. Lett. **65**, 1124 (1990).

[6] G. S. Higashi, R. S. Becker, Y. J. Chabal, and A. J. Becker, Appl. Phys. Lett. **58**, 1656 (1991).

[7] P. Jakob and Y. J. Chabal, J. Chem. Phys. **95**, 2897 (1991).

[8] P. Jakob, Y. J. Chabal, and K. Raghavachari, Chem. Phys. Lett. **187**, 325 (1991).

[9] P. Jakob, Y. J. Chabal, K. Raghavachari, and S. B. Christman, Phys. Rev. B **47**, 6839 (1993).

[10] S. Watanabe, Surf. Sci. **415**, 385 (1998).

[11] Y. J. Chabal, G. S. Higashi, K. Raghavachari, and V. A. Burrows, J. Vac. Sci. Technol. A **7**, 2104 (1989).

[12] P. Dumas, Y. J. Chabal, and P. Jakob, Surf. Sci. **269/270**, 867 (1992).

[13] M. Niwano, Y. Takeda, Y. Ishibashi, K. Kurita, and N. Miyamoto, J. Appl. Phys. **71**, 5646 (1992).

[14] C. H. Bjorkman, M. Fukuda, T. Yamazaki, S. Miyazaki, and M. Hirose, Jpn. J. Appl. Phys. **34**, 722 (1995).

[15] M. Nakamura, M. B. Song, and M. Ito, Electrochim. Acta **41**, 681 (1996).

[16] N. Miyata, S. Watanabe, and S. Okamura, Appl. Surf. Sci. **117/118**, 26 (1997).

[17] D. Gräf, S. Bauer-Mayer, and A. Schnegg, J. Vac. Sci. Technol. A **11**, 940 (1993).

[18] V. L. Thanh, D. Bouchier, and G. Hincelin, J. Appl. Phys. **87**, 3700 (2000).

[19] Y. J. Chabal, G. S. Higashi, and R. J. Small, *Handbook of Silicon Wafer Cleaning Technology* (2nd Edition), edited by K. A. Reinhardt and W. Kern (William Andrew Publishing, Norwich, NY, 2008), p. 515.

[20] L. Pauling, *The Nature of Chemical Bond* (3rd Edition), (Cornell Univ. Press, Ithaca, NY, 1960), p. 260.

[21] V. Gogonea, C. Bãleanu-Gogonea, and E. Osawa, J. Mol. Struct. (Theochem) **432**, 177 (1998).

[22] S. Ciraci and I. P. Batra, Surf. Sci. **178**, 80 (1986).

[23] J. E. Northrup, Phys. Rev. B **44**, 1419 (1991).

[24] K. Endo, K. Arima, K. Hirose, T. Kataoka, and Y. Mori, J. Appl. Phys. **91**, 4065 (2002).

[25] U. Freking, P. Krüger, A. Mazur, and J. Pollmann, Phys. Rev. B **69**, 035315 (2004).

[26] M. F. Faggin and M. A. Hines, Rev. Sci. Instrum. **75**, 4552 (2004).

[27] J. J. Boland, Phys. Rev. Lett. **67**, 1539 (1991).

[28] Y. J. Chabal and K. Raghavachari, Phys. Rev. Lett. **53**, 282 (1984).

[29] Y. J. Chabal and K. Raghavachari, Phys. Rev. Lett. **54**, 1055 (1985).

[30] M. K. Weldon, K. T. Queeney, A. B. Gurevich, B. B. Stefanov, Y. J. Chabal, and K. Raghavachari, J. Chem. Phys. **113**, 2440 (2000).

[31] Y. Caudano, P. A. Thiry, and Y. J. Chabal, Surf. Sci. **502**, 91 (2002).

[32] B. S. Aldinger, Ph. D. Dissertation, Cornell University, 2010.

Chapter 4

Bubble-Induced Roughening and Microfaceting of Si(100) during Aqueous NH_4F Etching

4.1. Introduction

Production of H/Si surfaces of atomic-scale smoothness is highly desired in the semiconductors industry, since the roughness of starting wafers is known to degrade the performance of fabricated devices.[1,2] One of the sources of roughness of the Si wafers is the aggressive chemicals used to clean the surfaces during wafer processing. An ideal cleaning solution would both clean the surface and produce atomically smooth surfaces. In 1990, Higashi *et al.*[3,4] showed that atomically smooth H-terminated Si(111) surfaces can be produced by room temperature etching with 40% NH_4F (aq.). Atomistic simulations of surface etching[5,6] explained this observation in terms of preferential etching of defects sites, such as step and kink sites, over terrace sites. Later, Arima *et al.*[7] showed that anisotropic etching by NH_4F (aq.) also produces relatively smooth Si(110) surfaces.

Anisotropic etchants preferentially etch all crystal faces rapidly except one, which leads to the development of characteristic shapes during etching. For example, an anisotropic etchant, such as KOH (aq.), preferentially etches all crystal faces of silicon except the slow-etching (111) face, thereby causing convex surfaces, such as spheres, to display the fastest etching planes and concave surfaces to display the slowest etching planes.[8] For this reason, anisotropic etchants are used extensively in bulk micromachining for applications ranging from sensors to actuators to microfluidics.

The production of atomically-smooth Si(100) surfaces — the substrate of choice in microelectronics — by anisotropic etching was intensively sought by many research groups around the world, but such an etchant remained elusive for a long time. Chapter

3 shows that anisotropic etching by NH_4F *could* generate Si(100) surface of near-atomic smoothness if H_2 bubbles produced during etching were periodically removed. This Chapter shows that more factors than etchant anisotropy determine the etch morphology. In NH_4F etching of Si(100), one of these factors is H_2 bubbles produced by the etching reaction.

In NH_4F solutions, silicon etching has been postulated to proceed through sequential oxidation and etching reactions of the form[9]

Oxidation: $\equiv Si{-}H + OH^- + H_2O \rightarrow \equiv Si{-}OH + H_2 + OH^-$, and

Etching: $(\equiv Si)_3Si{-}OH + 3HF \rightarrow 3(\equiv Si{-}H) + SiF_3OH$.

The profound H-termination of the NH_4F-etched Si surfaces has been attributed to oxidation being the rate-limiting step.[10] This reaction also evolves H_2 gas.

The effects of bubbles on silicon etching is not well understood. Bubble evolution has been observed in the KOH (aq.) etching of H/Si(100),[11] where it has been postulated to form both pillars[12] and pyramids[13,14] on the surface, presumably by masking (blocking) the regions underneath the bubble from etching. Nevertheless, the mechanism of pyramid formation is still under debate.[14] Bubble-induced roughening during NH_4F etching was reported previously on vicinal H/Si(111) and H/Si(100) surfaces;[9] however, the mechanism underlying these changes was not investigated.

This chapter examines the effects of H_2 bubbles on the morphology of H/Si(100) surfaces etched in room-temperature NH_4F (aq.). Bubble evolution led to the formation of characteristic morphological features on multiple length scales. These features were characterized with optical microscopy, optical interferometry, and atomic force microscopy (AFM). Based on these studies, new mechanisms of bubble-induced roughening and microfaceting are proposed. Methods to suppress bubble-induced roughening are also presented.

4.2. Experimental

Samples were cut from 500-μm-thick, Cz-grown wafers (P-doped, 0.5-10 Ω cm) and 500-μm-thick, float-zone wafers (*p*-type, resistivity >1000 Ω cm) which were thermally oxidized and annealed to produce a ~1000-Å-thick oxide layer as described in Chapter 2. The wafers were then diced into 0.6″ × 1.5″ samples for optical microscopy and optical interferometry or ~ 0.3″ × 0.3″ samples for AFM and side-profile microscopy.

For each experiment, all labware was given a standard RCA clean, as described in Chapter 2. The sample was subjected to a RCA clean and then immersed in buffered oxide etch (BOE, J. T. Baker, CMOS grade), a 5:1 by volume mixture of 40% NH_4F (aq.) and 50% HF (aq.), for 75 s to produce a H-terminated starting surface. The sample was then etched in room temperature, quiescent 40% NH_4F (aq., J. T. Baker, CMOS grade) for varying time periods. After etching, the sample was rinsed for 15 s in ultra-pure water (Millipore Milli-Q).

The morphologies of the etched surfaces were characterized with optical microscopy, optical profilometry, and atomic force microscopy (AFM). In optical microscopy, samples were imaged in dark-field mode to enhance contrast of micro-scale roughness. Optical interferometry was performed with an ADE Phase Shift MicroXAM optical interferometric profiler. AFM images were obtained in non-contact tapping mode with a Digital Instruments Multimode Atomic Force Microscope.

The growth of H_2 bubbles on the etching surface was studied *in-situ* using optical microscopy in two geometries. In the first geometry, the sample was etched in a custom Teflon cell while bubbles were imaged from above in dark-field mode. In the second geometry, the sample was etched in a glass cuvette with parallel flat sides while bubbles were imaged from the side using a Digital Bright Field Microscope (Hirox,

KH-7700). A Teflon spacer was placed under the sample to prevent optical distortions from the cuvette base.

The etch rate of the surface in 40% NH_4F (aq.) was determined gravimetrically by etching a 100-mm-diameter, double-side-polished wafer in a glass petri dish suspended in an ultrasonic bath. Sonic agitation dislodged bubbles from the surface. This method yielded an etch rate of 1.5 monolayer/s for room-temperature NH_4F etching of Si(100).

To test the effect of electrolytes on bubble formation, ammonium acetate (Mallinckrodt Chemicals) was added to 40% NH_4F (aq.) to produce a 1.5 M NH_4OOCCH_3, 40% NH_4F aqueous solution, which was then used as the etchant.

4.3. Results

When a Si(100) sample with an optically smooth surface was etched in quiescent 40% NH_4F (aq.), bubbles formed on the surface within 15-20 s. After ~20 min of etching, the sample was hazy by eye. Dark-field optical microscopy revealed a complex hierarchy of morphological features as shown in Fig. 4.1(a). (In dark-field mode, a flat surface would appear black. Light and colored regions are indicative of

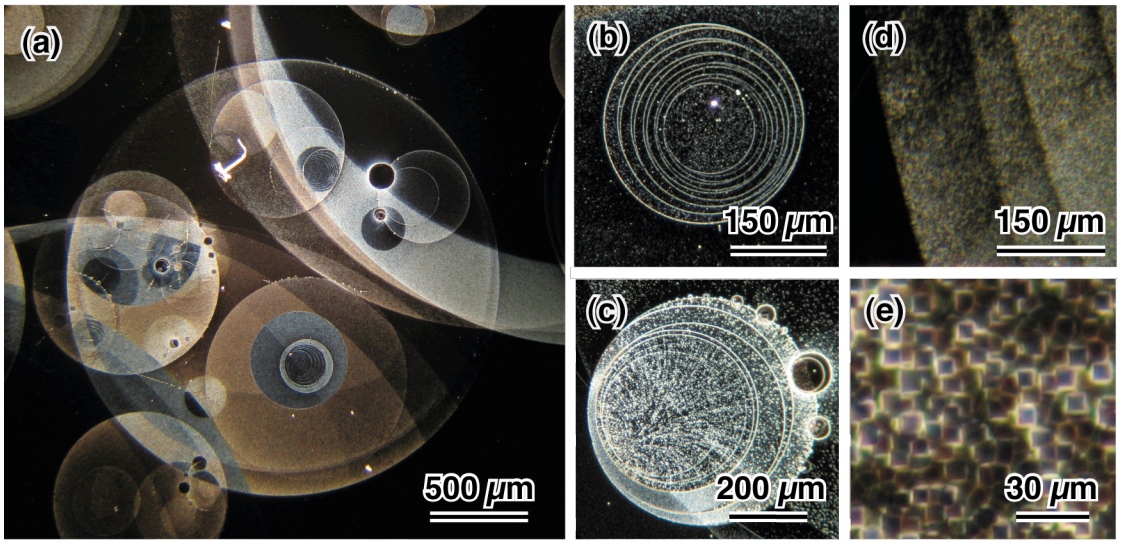

Figure 4.1. (a) Dark-field optical micrographs of a Si(100) surface etched in room-temperature, quiescent 40% NH_4F (aq.) for 1 hr showing a wide range of morphological features.

roughness.) The optical micrographs displayed three characteristic features: bright circular rings, which appeared singly or in nested ring patterns that were roughly concentric with comparable inter-ring spacings as shown in Fig. 4.1 (b, c); dark circles, which were often observed near the edges of the rings as seen in Fig. 4.1(c); and bright circular regions, as shown in Fig. 4.1(d). At higher resolutions, the bright circular regions appeared as fields of densely-packed squares with sides aligned with ⟨110⟩ and $\langle 1\bar{1}0 \rangle$ directions, as shown in Fig. 4.1(e).

As will be described in this section, the three types of features corresponded to circular pillars, circular pits, and microfaceted pits. The features were produced during different stages of bubble evolution. The vertical relief of these features, studied using optical profilometry and AFM, is described in Section 4.3.1. *In situ* studies of bubble growth and evolution are presented in Sections 4.3.2 and 4.3.3. Section 4.3.4 discusses features formed on the other principal faces of silicon, namely Si(111) and Si(110). Finally, Section 4.3.5 discusses methods to suppress bubble-induced roughening.

4.3.1. Vertical Relief of the Etch Features

The large circular rings observed in the optical micrographs were raised pillars as shown by optical interferometry. Fig. 4.2(a) shows the optical interferometric image of a 3-min-etched Si(100) surface which had several circular regions, all of which had

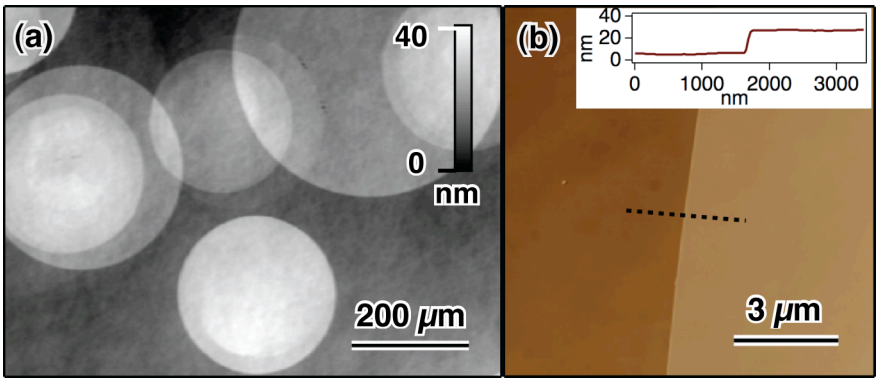

Figure 4.2. (a) Optical interferometry image of Si(100) surface etched in room-temperature, quiescent NH_4F (aq.) for 3 min. (b) AFM image of the edge of a pillar in (a). (Inset) Line profile extracted along the dashed line in the image.

heights ranging from 10 – 25 nm. The tops of these pillars were flat. When nested rings were observed, such as those in Fig 4.2(a), the inner circles always imaged lighter than the outer circles, indicating the formation of stepped, mesa-like structures. An AFM image of a pillar edge is shown in Fig. 4.2(b). Pillar edges were always sharp, as indicated by the line profile in Fig. 4.2(b).

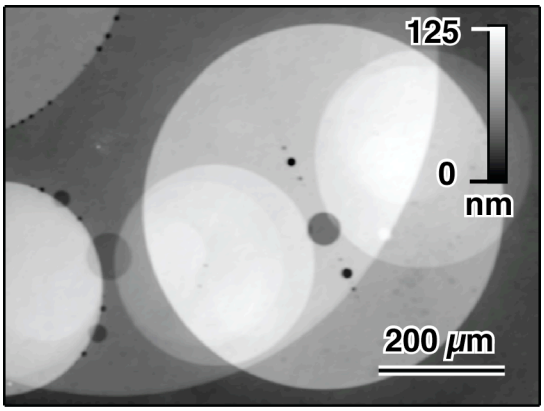

Figure 4.3. Optical interferometry image of Si(100) surface etched in room-temperature, quiescent NH_4F (aq.) for 8 min showing circular etch pits.

Optical interferometric images also showed that the small dark circles observed in the optical micrographs were circular pits. In the optical interferometric image shown in Fig. 4.3, several circular pits with depths ranging from 20 – 80 nm were observed.

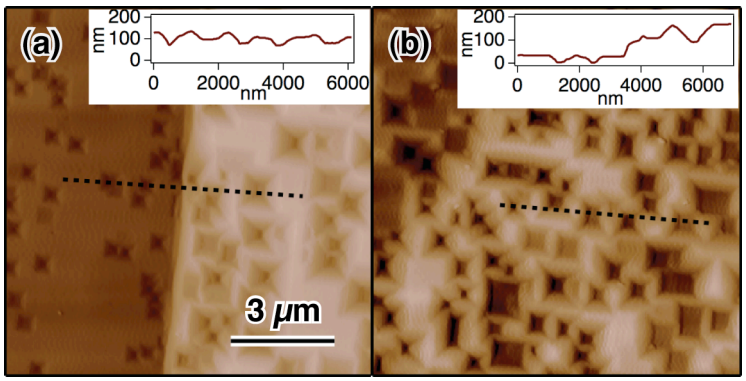

Figure 4.4. AFM images of a Si(100) surface etched in room temperature, quiescent NH_4F (aq.) for 25 min. The two images show different regions of the surface. Insets show line profiles of the sections highlighted by the black dashed lines.

The square features that constituted the rough regions on the surface were microfaceted pits. The AFM images of two different regions of a surface etched for 25 min in Fig. 4.4 show rough regions covered with square pits. As indicated by the line profiles, most of the pits were inverted square pyramids; some of the pits had flat bottoms. The pit density and size distribution varied widely across the surface. In some regions, as in Fig. 4.4(b), pits covered more than 50% of the surface area.

The formation and growth of these features was inherently linked to the temporal evolution of bubbles on the surface. To understand the formation of these features, the etching process was studied *in situ* as described in the following sections.

4.3.2. Bubble Masking and the Formation of Pillars

Real-time evolution of bubbles during etching was studied with *in situ* optical microscopy. When viewed from above, some bubbles appeared to grow continuously, whereas others grew in discrete steps. The latter mode is illustrated by Fig. 4.5, which presents individual frames of a video micrograph of a growing bubble. The bubble remained stationary for five seconds (t = 86 – 91 s), then suddenly expanded at t = 91 s over the course of a single frame (<1 s). This pattern of apparent immobility for tens of seconds followed by sudden expansion repeated four times from t = 86 s to 156 s. As discussed later, this discontinuous growth behavior led to the formation of nested pillars. But what caused this discontinuous growth? Was H_2 gas being added to the bubble in discrete events or was another mechanism responsible for this effect?

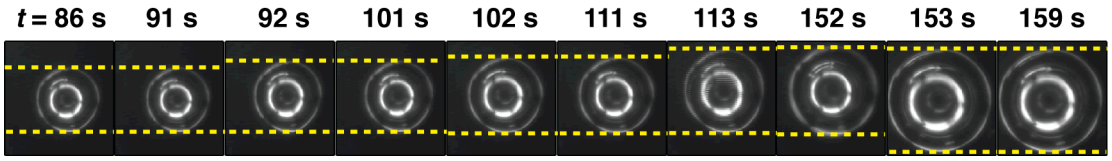

Figure 4.5. Individual frames extracted from a dark-field videomicrograph of a H_2 bubble growing on Si(100) etching in NH_4F (aq.) The etchant was added to the sample at t = 0, and the time of each frame is indicated above the frame. Yellow dashed lines indicate the size of the bubble. Each frame is ~120 μm × 120 μm.

Side profile images of the growing bubbles, such as that shown in the inset of Fig. 4.6(a), revealed the cause of the discontinuous growth. This geometry allowed for direct measurement of the height, width and contact diameter of the bubble. By fitting the bubble profile to a truncated ellipse and assuming cylindrical symmetry with respect to the surface normal, the bubble volume could also be estimated. Fig. 4.6 shows the temporal evolution of a bubble that underwent discontinuous growth. Two different growth modes were observed for the bubble. For the first 70 s of growth, the bubble grew roughly continuously, with the contact width and height increasing constantly. At later times, the contact width began to grow discontinuously as indicated by the dashed lines in Fig. 4.6. In this regime, the contact width remained constant for tens of seconds (*e.g.*, during $t = 76 – 105$ s), apparently remaining pinned at the contact boundary, while the bubble height grew. The contact width then increased suddenly (*e.g.*, at $t = 106$ s) concomitant with a sudden height decrease. Interestingly, these discontinuous changes in bubble morphology were not accompanied by sudden changes in volume. Instead, the bubble volume grew continuously.

Bubble growth could be explained by a simple model. If the bubble primarily grew through diffusion of H_2 gas from the near-surface region of the etchant and this layer remained at constant supersaturation with time, then the bubble growth rate would be

$$\frac{dV}{dt} = a\pi D$$

where V and D are the volume and the contact diameter of the bubble, respectively, and a is a constant. The volume V at any time is therefore

$$V(t) = V(0) + a\pi \int_0^t D(t')dt' .$$

As shown by the fit in Fig. 4.6(c), this model was in good agreement with experiment. In contrast, a model that assumed that H_2 gas diffused through the entire surface of the

bubble did not agree well with the experiment. The agreement of this model with the data showed that the bubble volume growth was unaffected by the discontinuous increase in the contact width.

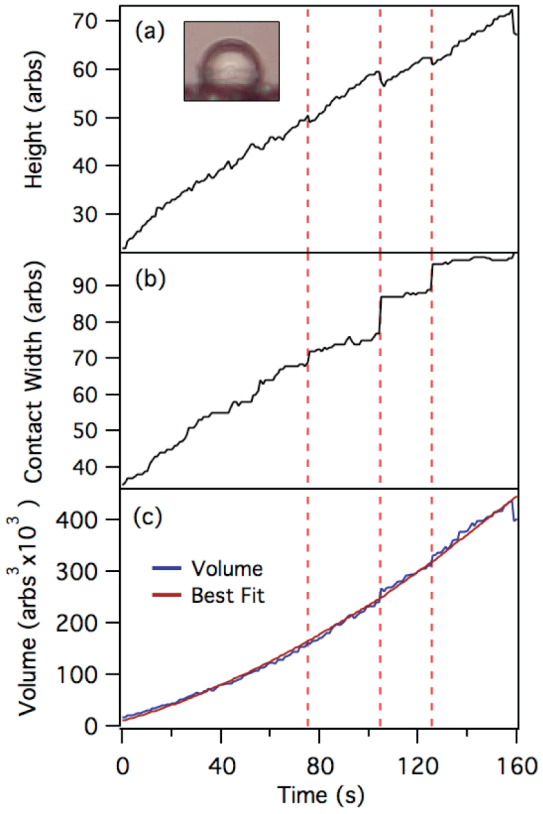

Figure 4.6. (a) Height, (b) contact width, and (c) volume of a single H_2 bubble (inset) on a Si(100) surface during NH_4F etch, obtained from side-profile imaging, plotted as a function of time. The red line in (c) is the best fit to the model described in the text.

As discussed later, discontinuous expansion of the bubbles' contact width led to the formation of the observed nested pillars. Nevertheless, these pillars contributed minimally to the surface roughness, as only the sharp edges were rough. These observations did not explain the primary cause of roughness: the tiny etch pits.

4.3.3. Bubble Coalescence and the Formation of Pits

The growth of bubbles on the etching surface sometimes led to the touching and subsequent coalescence of adjacent bubbles. These coalescence events sometimes

produced tiny droplets of etchant underneath the coalesced bubbles — droplets that subsequently led to the formation of etch pits.

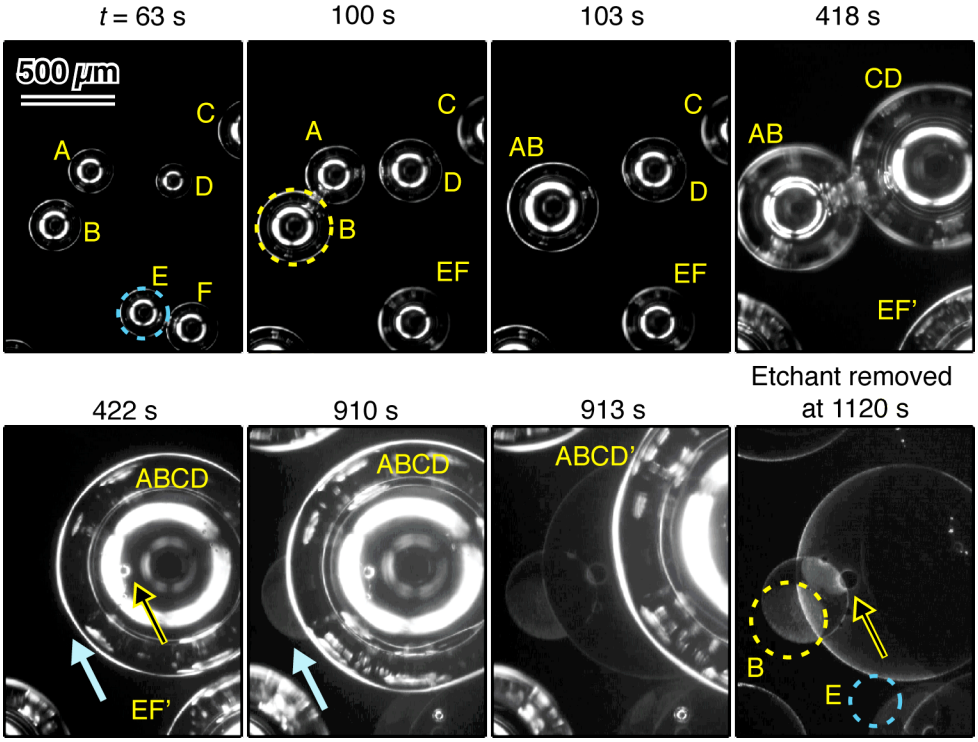

Figure 4.7. Individual frames of a dark-field videomicrograph of H_2 bubbles growing on a Si(100) surface during NH_4F (aq.) etching showing the coalescence of the bubbles. The time labeled is measured from the addition of the etchant. The last image was taken after removal of the etchant. Bubbles are labeled by capital letters, and coalesced bubbled are labeled by combinations of letters of the coalescing bubbles. Bubble coalesced with another bubble outside the image are denoted by a prime.

In some cases, droplet formation could be imaged directly in an optical microscope. For example, Fig. 4.7 shows select frames from a dark-field videomicrograph of an etching surface. The micrographs show six bubbles, labeled **A-F**, growing on the surface after etching for 63 s. As the etching progressed, these bubbles coalesced to form bubbles **EF**, **AB**, and **CD** at t = 100 s, 103 s and 418 s, respectively, then the bubbles **AB** and **CD** further coalesced to form the bubble **ABCD** at t = 422 s. Inside the coalesced bubble **ABCD**, a tiny etchant droplet could be seen**,**

highlighted by the black arrow in Fig. 4.7 at t = 422 s. The droplet was roughly located at the periphery of the circular region that was masked by the bubble **AB** at t ~ 418 s. After about 11 min of further etching, the etchant was removed from this sample. On the etched surface, shown in the last image in Fig. 4.7, circular pillars were observed where formerly the bubbles **AB** and **ABCD** were present. In addition to the pillars, circular etch pits, indicated by the black arrow, were visible at the former location of the tiny droplet under the bubble **ABCD**. These micrographs showed that the etchant droplets etched the underlying surface forming circular etch pits while the surrounding region under the bubble, exposed to the H_2 gas, did not etch.

The videomicrographs (such as shown in Fig. 4.7) also indicated the origin of the micron-size etch pits. These pits, which were visible as light regions in the dark field micrographs, did not develop under every bubble. For example, after the coalescence of bubbles **AB** and **CD** into bubble **ABCD,** approximately one-half of the area formerly under the bubble **AB**, indicated by the blue arrow in Fig 4.7 (t = 422 s), got exposed to the bulk etchant. This region appeared smooth at t = 422 s, but started to develop roughness with etching as indicated in Fig 4.7 (t = 910 s) by a blue arrow. In contrast, when the bubble **B** at t = 100 s coalesced with **A** to form bubble **AB**, approximately one-third of the region masked by **B**, highlighted by a yellow dashed circle, that got exposed to the bulk etchant after its coalescence showed no roughness even after prolonged etching. As shown by the yellow dashed circle in the last image in Fig. 4.7, only the two-thirds of the region that was masked by coalesced bubble **AB** was roughened. Similarly, the region masked by uncoalesced bubble **E** at t = 63 s, highlighted by a blue dashed circle, later got exposed to the bulk etchant, but two-thirds of this region remained smooth even after etching for ~18 min as shown in the last image in Fig. 4.7. These micrographs and many others revealed two trends in the formation of the micron-size pits. First, these pits nucleated under coalesced bubbles

only. Second, these pits grew and became visible in the optical micrographs only after the masked region under the bubble was re-exposed to the etchant, either through bubble migration or through bubble detachment. Based on the above studies, a mechanism explaining the formation of the etch pits is proposed in the discussion section.

Microfaceting of the sub-micron pits was consistent with the observation that these pits grew due to etching by the bulk solution. As mentioned in the introduction, concave features etched in anisotropic etchants evolve to reveal the slow etching face. On Si(100) surface, a concave feature would eventually evolve into a tetrahedral etch pits with {111} sides. If the starting feature were shallow, then stopping the etch before the full evolution of the etch pit would result in formation of a truncated tetrahedron with {111} sides and a (100) bottom.

The bubbles, in general, stayed on the surface for long periods of time. Bubbles detachment was infrequent and only occurred after long etch times. The prolonged stay of the bubbles on the surface caused frequent coalescence events that led to pronounced roughening of the surface.

4.3.4. Symmetry of Microfaceted Pits

The circular shape of the pillars and the larger etch pits was consistent with the (circular) shapes of the bubbles and etchant droplets, respectively, whereas the square shape of the sub-micron pits was consistent with the anisotropic etching of the four-fold-symmetric bulk Si(100) lattice. To verify the correlation of pit shapes with lattice symmetry, experiments were repeated on H/Si(111) and H/Si(110) surfaces, which have three- and two-fold rotational symmetries, respectively.

On long length scales, the etched H/Si(111) and H/Si(110) surfaces displayed circular etch features quite similar to those on the Si(100) surface; however, the three surfaces were very different on the micron scale. Figures 4.8(a) and (c) show optical

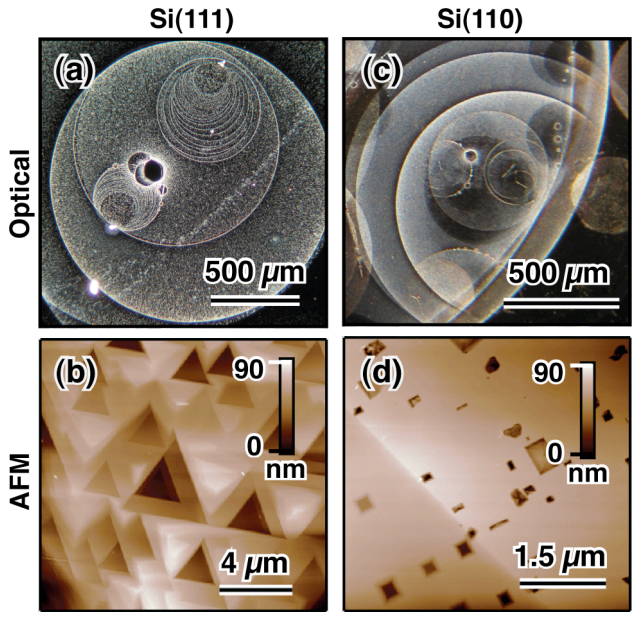

Figure 4.8. (a, c) Dark-field optical micrographs of Si(111) and Si(110) surfaces etched for 1 hr. in 40% NH_4F (aq.). (b, d) AFM images of the rough regions on etched Si(111) and Si(110) surfaces.

micrographs of NH_4F-etched Si(111) and Si(110) surfaces, respectively. The similarity of the circular etch features on the three surfaces suggested a common origin. In contrast, the AFM images in Fig. 4.8(b) and (d) showed the formation of micron-scale pits with triangular and predominantly rectangular habits on the Si(111) and Si(110) surfaces, respectively, which was consistent with the three- and two-fold rotational symmetries, respectively, of these surfaces. These results confirmed that the geometry of small pits was determined by the symmetry of the substrate lattice.

4.3.5. Methods to Prevent Bubble-Induced Roughening

The results in the previous sections showed that tiny etch pits — the principle source of surface roughness — were the result of bubble coalescence events. Any intervention that prevents bubble coalescence would therefore be expected to decrease surface roughness. To test this hypothesis, three methods were investigated.

The first method was to remove bubbles before they coalesced by periodically withdrawing the sample from the etchant every 15 s. This method produced the near-

atomically-flat morphologies on NH_4F-etched Si(100) surfaces described in Chapter 3. The etched surfaces showed no roughness in optical microscopy as well.

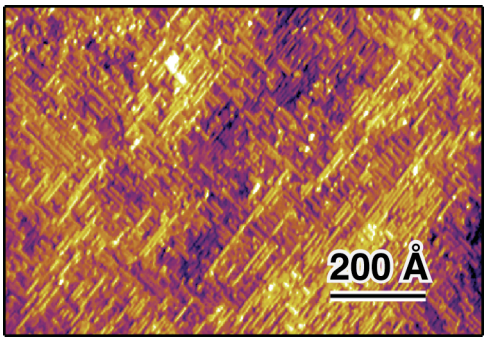

Figure 4.9. STM image of a nominally-flat Si(100) surface etched in 40% NH_4F (aq.) with ultrasonic agitation for 5 min.

In the second method, the sample was agitated with an ultrasonic bath during etching to dislodge the bubbles from the surface. This technique has been previously used to remove bubbles and reduce the formation of etch pyramids during KOH (aq.) etching of Si(100) surfaces;[15] however, in some cases, ultrasonic agitation during etching also induces defect etch pits.[16] In NH_4F etching of Si(100), this method produced near-atomically-flat Si(100) surfaces for etch durations ≤15 min, as shown by the STM image in Fig. 4.9. After extended etching, the surface became mesoscopically rough with a characteristic texture. The mechanism for this texturing was not investigated.

The third method used chemical additives to suppress bubble coalescence. Electrolytes are known to prevent bubble coalescence in aqueous solutions.[17] For example, the formation of foam in the sea water is attributed to this effect. The addition of surfactants to the aqueous Si etchants, however, is also known to produce significant changes in etch morphologies, presumably because the surfactants change the etching chemistry.[18] To test the effects of additives on the NH_4F etching of Si(100) surfaces, several electrolytes, including NaCl, LiCl, ammonium acetate (NH_4OOCCH_3), ammonium phosphate monobasic ($NH_4H_2PO_4$) and ammonium citrate dibasic

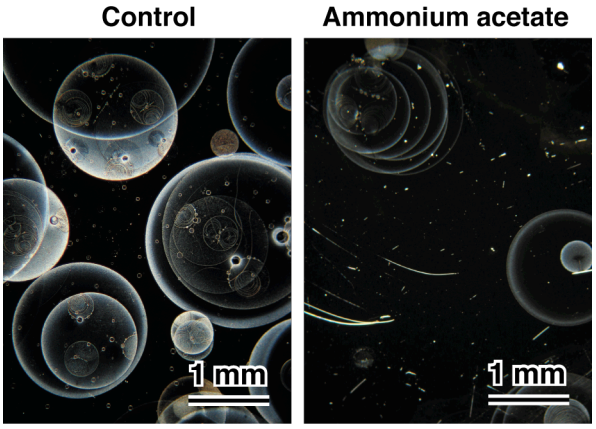

Figure 4.10. Dark-field optical micrographs of Si(100) surfaces etched for 1 hr. in 40% NH_4F (aq.) and 2 M NH_4OOCCH_3, 40% NH_4F (aq.).

$[(NH_4)_2HC_6H_5O_7]$, were added to 40% NH_4F in concentrations of 1 - 2 M. Of these, only ammonium acetate was effective in reducing bubble-induced roughening. When ammonium acetate was added to the etchant, fewer bubbles formed on the surface, and the etched surface had significantly fewer circular pillars and pits as shown by the optical micrographs in Fig. 4.10. The atomic-scale morphology of Si(100) surface etched in NH_4F (aq.) with ammonium acetate, as shown in Fig. 4.11, was identical to that obtained without any additives (Chapter 3). The similarity of the two morphologies strongly suggested that the addition of ammonium acetate did not significantly change the etching chemistry.

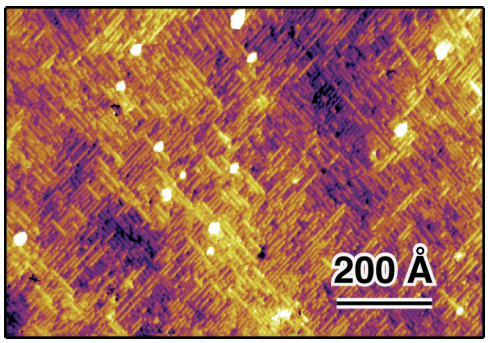

Figure 4.11. STM image of a nominally-flat Si(100) surface etched in 2 M NH_4OOCCH_3, 40% NH_4F (aq.) for 2 min.

The pronounced reduction in bubble formation by ammonium acetate was not due to reduction in the surface etch rate. The addition of ammonium acetate reduced the etch rate (measured gravimetrically) of Si(100) in 40% NH_4F (aq.) by only ~40%, whereas the surfaces obtained after 1 hr. of etching in the acetate-containing NH_4F solution were much smoother than those obtained by 30 min of etching in pure NH_4F (aq.).

4.4. Discussion

These results showed that the evolution of H_2 gas bubbles led to the formation of characteristic surface morphologies on many length scales. The principle morphological features on these surfaces included circular pillars, and circular and microfaceted etch pits, which resulted from the growth and coalescence of bubbles on the surface. Sections 4.4.1 and 4.4.2 discuss two mechanisms that explain the formation of these etch features. These results also explain some of the previous results on NH_4F/Si(100) etching that were inconsistent with the near-atomically flat morphology discussed in Chapter 3. This discussion is presented in Section 4.4.3.

4.4.1. Mechanism for Formation of Pillars

As mentioned in the introduction, pillar formation due to bubble evolution has been previously reported in KOH etching of Si(100) by Palik *et al*.,[12] who proposed a mechanism based on bubble masking of the etching surface. In this mechanism, supersaturation of the solution with H_2 gas produced by the etching reaction leads to nucleation of bubbles on the surface, presumably at surface defects or impurities. The surface underneath the bubbles is blocked from etching, while the surrounding surface continues to etch. This model assumes that the contact area of the bubble remains constant in time (until bubble detachment) and thus predicts the formation of isolated etch pillars.

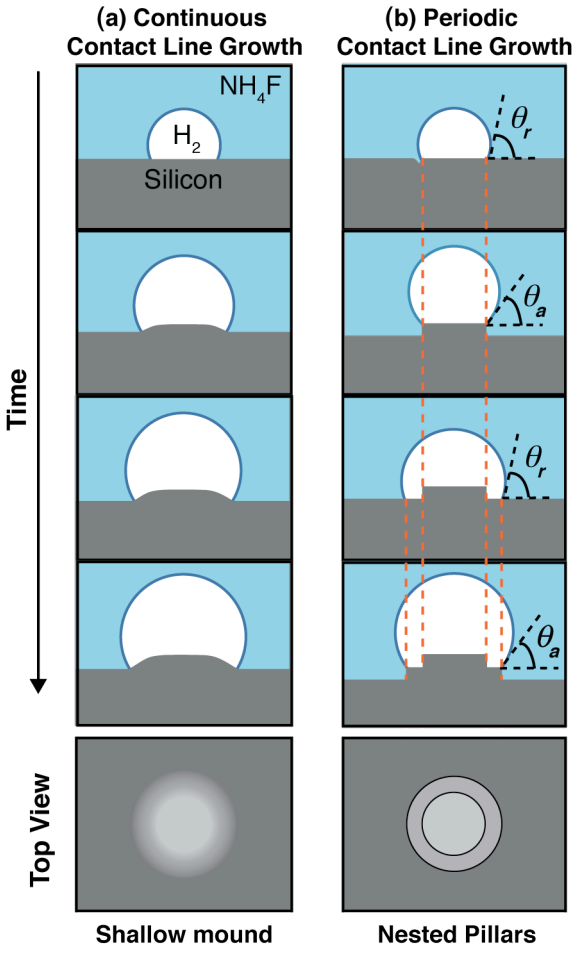

Figure 4.12. Mechanism for the production of (a) gently-curved mounds by continuous growth of the bubble contact line, and (b) nearly concentric, circular etch pillars due to contact line pinning by a defect, followed by periodic growth of the contact line. See text for explanation.

Results presented in previous sections showed that the bubble contact area during NH_4F etching was not stationary, but grew in two different modes. This growth required modification of the Palik *et al*. mechanism. In the first mode, the contact line of the bubble increased steadily with time, as illustrated in Fig. 4.12(a), presumably producing a shallow curved mound on the surface as shown in the bottom panel of Fig. 4.12(a). This mode predominated in early stages of bubble growth. Since shallow mounds lack sharp boundaries, they could not be imaged in optical microscopy. In the second mode, the contact line grew discontinuously, with periodic cycles of no motion

and sudden expansion. This process is illustrated in Fig. 4.12(b). During the period of no motion, constant etching of the surrounding area led to development of a pillar under the masked area, as in the Palik *et al*. mechanism. Successive periods of no motion and sudden expansion led to the formation of nested pillars in a "wedding cake" structure as seen in Figs. 4.1(b) and 4.2(a). Similar features have been reported by Palermo *et al.*[19] during NH_4F etching of doped (*p*-type) Si(100) surfaces.

The discontinuous growth of bubbles requires further explanation. The contact area of a bubble is expected to grow continuously unless it becomes (transiently) pinned at a surface defect or impurity. The pinning of the contact line by surface defects and chemical inhomogeneities is well known in fluid dynamics.[20,21] During continuous growth, the contact angle between the bubble and the surface would be θ_r, the receding contact angle,[20] as defined in Fig. 4.12(b). After the contact line becomes pinned, continued expansion of the bubble volume will lead to a continuous decrease in the bubble contact angle. If bubble growth causes the buoyant force to exceed the adhesive force, the bubble will detach and float to the surface. Alternatively, if bubble growth causes the elastic energy of the bubble to exceed the pinning energy, the contact line will depin, and the bubble will rapidly expand. Because of contact angle hysteresis,[22] the contact angle of the expanded bubble is uncertain but will be bounded by the advancing and receding contact angles — a ~30° range on H-terminated silicon.[23] The H_2 bubble will then increase in volume *without further motion of the contact line* until the contact angle again reaches the receding contact angle. If the contact line remains stationary for a sufficient period of time, the etchant will produce an etch pillar capable of pinning the bubble, starting the cycle of pinning and expansion over again.

This mechanism qualitatively explains the three observed stages of bubble growth. First, small bubbles grow continuously until pinned by a pinning site. Second, once a bubble becomes pinned, expansion of the bubble contact area becomes periodic

due to the combined action of contact angle hysteresis and bubble masking. This mode leads to the production of roughly concentric and equidistantly-spaced etch pillars. Importantly, the bubble volume continues to grow at a constant rate during this phase of growth. Finally, the bubble detaches from the surface once it grows to sufficient size.

4.4.2. Mechanism for Formation of Pits

The origin of the large circular pits was clearly visible in the optical videomicrography of the growing surface. When two nearby expanding bubbles touched each other and coalesced — a violent event — some of the etchant occasionally became trapped inside the coalesced bubble. This mechanism is illustrated in Fig. 4.13 (a). The trapped etchant formed small circular droplets, as illustrated in Fig. 4.13(b), under the coalesced bubble. These droplets were sometimes trapped by surface imperfections, such as pillar edges (*e.g.,* yellow arrow in Fig. 4.7). These droplets formed circular etch pits as sketched in Fig. 4.13(c).

The nucleation of the smaller micron-size microfaceted pits could not be directly imaged in the optical micrographs; however, the videomicrographs showed that these pits were also nucleated under the coalesced bubbles. In the proposed mechanism, the circular and the microfaceted etch pits are both nucleated during a coalescence event by droplets of etchant. The only difference between the two is the size of the droplets. Large droplets lead to circular pits, whereas small droplets (eventually) produce microfaceted pits.

The physical origin of the droplets remains uncertain. During coalescence, microdroplets could form either by the atomization of the etchant or by the dewetting of the thin film of etchant on the hydrophobic surface between the two coalescing bubbles. The breakup of thin films on non-wetting substrates and the resultant droplet pattern is an active area of research.[24] Under some conditions, spinodal dewetting of ultrathin

aqueous films leads to the spontaneous formation of submicron patterns[25] — an effect that has been used to deposit uniform array of particles.[26]

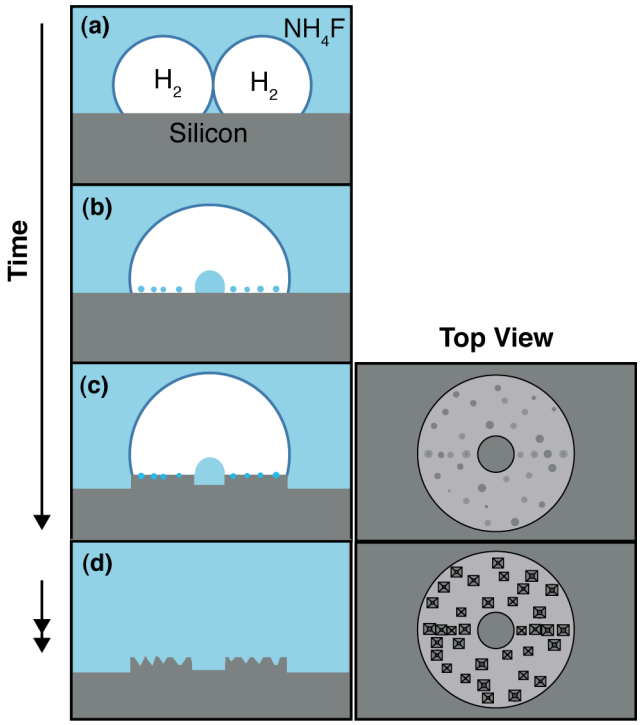

Figure 4.13. Mechanism for the production of circular and microfaceted etch pits. (a) Two nearby bubbles touched and coalesced. (b) The coalescence produced a large number of etchant droplets of varying size under the coalesced bubble. (c) The etchant droplets nucleated circular etch pits. (d) Subsequent exposure of the etch pits to the etchant led to microfaceting of the smaller etch pits.

When the etch pits nucleated under the coalesced bubble were later exposed to the bulk etchant (*e.g.*, due to bubble detachment or migration), the initially circular etch pits were anisotropically etched. This process is illustrated in Fig. 4.13 (d). Depending upon the initial size of the pits and the duration of subsequent etching, the shape of the pits evolved, eventually revealing slow-etching {111} facets. For smaller etch pits, {111} facets formed quickly, leading to rapid formation of tetrahedral pits. In contrast, much more material would have to be removed from the large circular pits to produce faceting. As a result, the pits remained circular for the time scale of the experiment.

4.4.3. Reconciliation With Previous Studies of NH_4F-etched Si(100)

A number of previous studies of Si(100) surfaces etched in NH_4F (aq.) for extended periods of time concluded that prolonged etching resulted in {111} facet formation. The thermal desorption spectroscopy (TDS) and reflection high-energy electron diffraction (RHEED) studies by Thanh *et al.*[27] showed an increase in the density of monohydrides on the NH_4F-etched surface with the etch time. Niwano *et al.*[28] reported the observation of Si-H vibrational bands on NH_4F-etched Si(100) at ~2083 cm^{-1} that grew with etch time — a clear indication of (111) facet formation. Nakamura *et al*.[29] studied etching of Si(100) surfaces in dilute NH_4F solution (~1%) with infrared spectroscopy and observed similar trends. These observations are at odds with the near-atomically-flat Si(100) surfaces produced by NH_4F etching described in Chapter 3. How can these apparently contradictory results be reconciled?

The reported increases in monohydride density with time were consistent with the long-term roughening and (111) microfacet formation due to H_2 bubbles. For example, microfaceting densities as high as 50% were observed on some etched surfaces [*e.g.,* Fig. 4.4(b)].

4.5. Conclusions

When the H_2 gas bubbles formed as a product of the NH_4F etching were allowed to accumulate on an etching silicon surface, three types of characteristic morphological features were observed: circular pillars (both isolated and in nested groups), circular etch pits, and microfaceted etch pits. The symmetry of the surface determined the shape of the microfaceted etch pits. Square, triangular, and rectangular etch pits with predominantly {111} facets were produced on Si(100), Si(111), and Si(110) surfaces, respectively.

Two mechanisms for the formation of bubble-induced morphological features were proposed. In the first, masking of the etching surface by H_2 bubbles produced

circular pillars. The volume of the bubbles grew constantly until detachment from the surface. If the contact line of the growing bubbles became pinned by a surface contaminant or irregularity, the growing bubble would sometimes display periodic cycles of contact line expansion that was attributed, in part, to contact angle hysteresis. This cyclic growth process led to the formation of nested pillars. The second mechanism explained the formation of both circular and microfaceted etch pits. Bubbles growing near to one another sometimes touched and coalesced. The coalescence occasionally produced trapped etchant droplets under the coalesced bubbles. These droplets nucleated etch pits. When the etch pits nucleated under the coalesced bubbles were re-exposed to the bulk etchant, the micron-size pits developed (111) microfacets due to anisotropic etching by the etchant, whereas larger pits remained circular.

Three methods for suppressing bubble-induced roughening were demonstrated: periodic withdrawal of the sample from the etchant, ultrasonic agitation of the etchant, and addition of an electrolyte (ammonium acetate). All three methods produced near-atomically-flat surfaces.

REFERENCES

[1] T. Ohmi, K. Kotani, A. Teramoto, and M. Miyashita, IEEE Electron Device Lett. **12**, 652 (1991).

[2] R. Kuroda, T. Suwa, A. Teramoto, R. Hasebe, S. Sugawa, and T. Ohmi, IEEE Trans. Elec. Dev. **56**, 291 (2009).

[3] G. S. Higashi, Y. J. Chabal, G. W. Trucks, and K. Raghavachari, Appl. Phys. Lett. **56**, 656 (1990).

[4] G. S. Higashi, R. S. Becker, Y. J. Chabal, and A. J. Becker, Appl. Phys. Lett. **58**, 1656 (1991).

[5] J. Flidr, Y.-C. Huang, T. A. Newton, and M. A. Hines, J. Chem. Phys. **108**, 5542 (1998).

[6] H. Zhou, J. Fu, and R. M. Silver, J. Phys. Chem. C **111**, 3566 (2007).

[7] K. Arima, J. Katoh, S. Horie, K. Endo, T. Ono, S. Sugawa, H. Akahori, A. Teramoto, and T. Ohmi, J. Appl. Phys. **98**, 103525 (2005).

[8] M. Elwenspoek and H. V. Jansen, *Silicon Micromachining* (Cambridge Univ. Press, Cambridge, 1998).

[9] P. Jakob and Y. J. Chabal, J. Chem. Phys. **95**, 2897 (1991).

[10] J. Flidr, Y.-C. Huang, T. A. Newton, and M. A. Hines, Chem. Phys. Lett. **302**, 85 (1999).

[11] E. D. Palik, V. M. Bermudez, and O. J. Glembocki, J. Electrochem. Soc. **132**, 871 (1985).

[12] E. D. Palik, O. J. Glembocki, I. Heard, Jr., P. S. Burno and L. Tenerz, J. Appl. Phys. **70**, 3291 (1991).

[13] S. A. Campbell, K. Cooper, L. Dixon, R. Earwaker, S. N. Port, and D. J. Schiffrin, J. Micromech. Microeng. **5**, 209 (1995).

[14] H. Schröder, E. Obermeier, and A. Steckenborn, J. Micromech. Microeng. **9**, 139 (1999).

[15] T. Baum and D. J. Schiffrin, J. Micromech. Microeng. **7**, 338 (1997).

[16] D. G. Schimmel, J. Electrochem. Soc. **126**, 479 (1979).

[17] V. S. J. Craig, B. W. Ninham, and R. M. Pashley, J. Phys. Chem. **97**, 10192 (1993).

[18] R. A. Wind and M. A. Hines (unpublished results).

[19] V. Palermo, E. Susi, and D. Jones, J. Electrochem. Soc. **151**, G554 (2004).

[20] P.-G. de Gennes, F. Brochard-Wyart, and D. Quéré, *Capillarity and Wetting Phenomena: Drops, Bubbles, Pearls, Waves*, translated by A. Reisinger, (Springer-Verlag, New York, 2004), p. 69.

[21] R. H. Dettre and R. E. Johnson, Jr. in *Contact Angle, Wettability and Adhesion*, edited by F. M. Fowkes (Advances in Chemistry, American Chemical Society, Washington DC, 1964), p. 136.

[22] L. Gao and T. J. McCarthy, Langmuir **22**, 6234 (2006).

[23] J.-G. Park and S. Raghavan, J. Adhesion Sci. Tech. **7**, 179 (1993).

[24] R. V. Craster and O. K. Matar, Rev. Mod. Phys. **81**, 1131 (2009).

[25] U. Thiele, M. Mertig, and W. Pompe, Phys. Rev. Lett. **80**, 2869 (1998).

[26] L. V. Govor, R. Reiter, G. H. Bauer, and J. Parisi, Phys. Rev. E **76**, 41609 (2007).

[27] V. L. Thanh, D. Bouchier, and G. Hincelin, J. Appl. Phys. **87**, 3700 (2000).

[28] M. Niwano, Y. Takeda, Y. Ishibashi, K. Kurita, and N. Miyamoto, J. Appl. Phys. **71**, 5646 (1992).

[29] M. Nakamura, M. B. Song, and M. Ito, Electrochim. Acta **41**, 681 (1996).

Chapter 5

Kinetic Monte Carlo Simulations of Anisotropic Si(100) Etching: Modeling the Chemical Origins of Characteristic Etch Morphologies*

An atomistic, chemically realistic, kinetic Monte Carlo simulator of anisotropic Si(100) etching was developed. Surface silicon atoms were classified on the basis of their local structure, and all atoms of each class were etched with the same rate. A wide variety of morphologies, including rough, striped, and hillocked, was observed. General reactivity trends were correlated with specific morphological features. The production of long rows of unstrained dihydride species, recently observed in NH_4F (aq) etching of Si(100), could only be explained by the rapid etching of dihydrides that are adjacent to (strained) monohydrides — so-called "α-dihydrides." Some etch kinetics promoted the formation of {111}-microfaceted pyramidal hillocks, similar in structure to those observed experimentally during Si(100) etching. Pyramid formation was *intrinsic* to the etch kinetics. In contrast with previously postulated mechanisms of pyramid formation, no masking agent (*e.g.,* impurity, gas bubble) was required. Pyramid formation was explained in terms of the slow etch rate of the {111} sides, {110} edges and the dihydride species that terminated the apex of the pyramid. As a result, slow etching of Si(111) surfaces was a necessary, but insufficient, criterion for microfacet formation on Si(100) surfaces.

* Reproduced with permission from the Journal of Chemical Physics **133**, 44710 (2010).

5.1. Introduction

Anisotropic etchants — etchants that selectively attack all faces of a crystal except for one specific face — have long fascinated engineers and scientists. From an engineering perspective, these etchants are highly prized, as they can selectively and inexpensively machine very smooth and precisely aligned planes from bulk material, in some cases producing near-atomically flat surfaces. For example, anisotropic silicon etchants have been used to selectively machine Si{111} faces for everything from ink jet nozzles[1,2] to nanoscale channels for ultrasmall transistors.[3] From a surface chemistry perspective, the high face-specificity of the etchants is fascinating, as it implies that the chemical reactions are highly site-specific, selectively removing defect species while leaving the majority species essentially untouched. Understanding the chemical origins of this high defect-specificity has been challenging, though, as most surface-sensitive analytical techniques cannot detect species present in concentrations less than a few percent of a monolayer.

Scanning tunneling microscopy (STM) is an exception to this rule. Under optimal conditions, atomic-scale defect (*e.g.,* missing atom) densities as low as 0.01% are readily observable. In addition, the highly site-specific chemical reactions involved in aqueous etching produce a wide variety of characteristic, atomic-scale etch morphologies, including straight or faceted steps, smooth terraces, single- or multi-atom-wide stripes, faceted hillocks and symmetrically shaped etch pits. In a sense, etching reactions write a record of their site-specific reactivity into the etched surface. The challenge is in reading this record and in extracting a quantitative understanding of site-specific reaction rates from morphological images. Once quantified, the site-specific reaction rates can be correlated with the structure and bonding of the sites to give insight into chemical reaction mechanisms.[4,5]

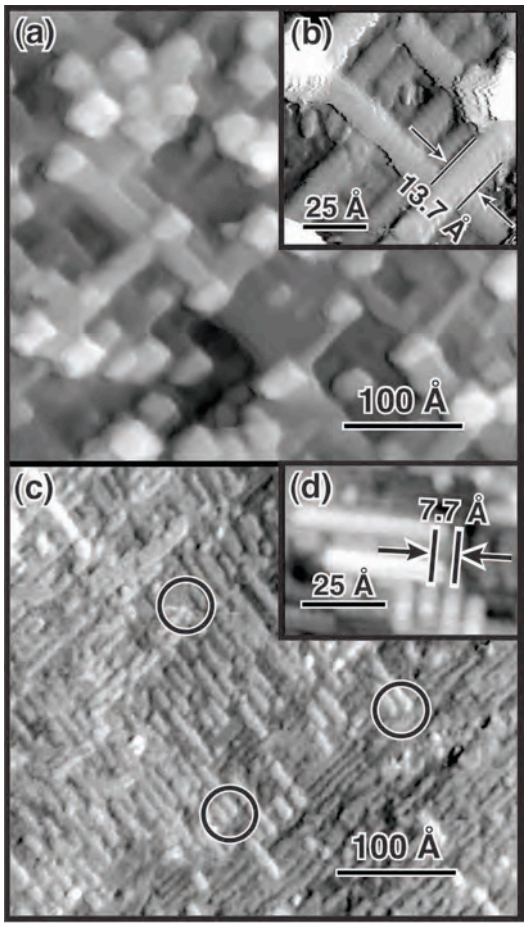

Figure 5.1. Representative STM images of anisotropically etched, H-terminated Si(100) surfaces etched in (a, b) room temperature, deoxygenated H_2O for 11 hr,[6] and (c, d) room temperature, 40% NH_4F (aq.) for 30 s.[7] The circles in (c) highlight the structure of stripe ends (*vide infra*).

This challenge is illustrated by the two STM images of etched Si(100) surfaces in Fig. 5.1. The two surfaces were etched in room temperature aqueous etchants that both produced entirely hydrogen-terminated etched surfaces. The surface in the top images, Figs. 5.1(a) and 5.1(b), was etched in pure (deoxygenated) H_2O,[6] whereas the lower surface, Figs. 5.1(c) and 5.1(d), was etched in an aqueous NH_4F solution (*p*H ~ 7.8).[7] The two morphologies are strikingly different. The top surface is characterized by multi-atom-wide orthogonal "stripes" that intersect to form roughly square pyramidal hillocks. In contrast, the etchant that produced the bottom surface selectively removed every other row of atoms, producing a characteristic cross-hatch pattern of single-atom-

wide stripes. What chemical reactions produced these surfaces? And why do these two etchants produce chemically similar (H-terminated) surfaces with such strikingly different morphologies?

We have developed an atomistic, chemically realistic, kinetic Monte Carlo simulation of the etching of H-terminated Si(100) surfaces that can be used to simulate experimental morphologies and ultimately extract site-specific reaction rates. From a computational perspective, this model is very similar to that developed by Flidr *et al.*[8] for the study of H-terminated, etched Si(111) surfaces. From a chemical perspective, though, the H/Si(111) and H/Si(100) surfaces are very different. The former is essentially unstrained, and most of the reactive sites have a near-bulk geometry. In contrast, the H/Si(100) surface is highly strained by interadsorbate interactions (*vide infra*) which complicate modeling.

The model made a number of assumptions that were well justified for the etching of Si(100) surfaces in many aqueous media. (These assumptions are not universally applicable to all silicon etchants.) First, the model assumed that silicon etching was the only chemical reaction; surface diffusion of silicon atoms was explicitly forbidden, as was the redeposition of etched atoms. These assumptions were justified by previous research. For example on clean (*i.e.,* adsorbate-free) Si(100) surfaces, surface diffusion is not observed over periods of hours at 230 °C,[9] and H-termination is expected to further stabilize the surface against diffusion. Similarly, the deposition of crystalline silicon from aqueous solutions has never been observed.[10] Second, the model assumed that the etching surface remained relatively smooth; undercutting was explicitly forbidden. Since this simulation will be used to model experimental STM images, which typically require a relatively flat surface for imaging, this assumption was also justified. Third, the model assumed that the etching surface was entirely H-terminated at all times; dangling bonds and other adsorbed species (*e.g.,* –OH) were

forbidden. This assumption is consistent with spectroscopic studies of Si(100) surfaces etched in H_2O[6] and NH_4F (aq.),[7] which both produce markedly hydrophobic surfaces. We note, however, that this assumption may not be appropriate for some aqueous etchants, particularly strong bases.[11] Finally, the dimerization of neighboring silicon atoms was forbidden. Although dimerized, H-terminated Si(100) surfaces are produced by some ultrahigh vacuum methods,[12,13] no dimerization has been observed in spectroscopic investigations of Si(100) surfaces etched in aqueous solutions.[6,7]

The model also assumed that the etch rate of any site on the surface was determined solely by the local structure (but not necessarily only the nearest-neighbor structure *vide infra*) of the site. In other words, long-range effects, such as substrate strain and diffusion in the etchant (*i.e.,* reactant depletion and product accumulation), were neglected. Although long-range strain fields[14,15] and diffusional processes[16] are known to produce perturbations in step distributions under some conditions, these are second-order effects.

The model treated the site-specific etch rates as *fully adjustable parameters* to be determined by comparison to experiment. Other approaches are also possible. For example, Gosálvez and coworkers have parameterized the activation barrier of different sites to etching using a bond-counting algorithm[17] that can be supplemented with adjustable site interaction energies.[18] Using this approach, they have successfully reproduced macroscopic etch anisotropies (*i.e.,* face-dependent etch rates) and many morphological features observed in experiment. Direct calculation of all of the necessary activation barriers with accuracy sufficient to reproduce experimental observations appears to be infeasible at this date. Some attempts have been made to base estimates of these activation energies on calculated bond energies; however, some adjustable parameters are still necessary to reproduce experimental observations.[19]

The challenge in developing a chemically realistic model of Si(100) etching is in defining a minimal set of chemically distinct etch sites — a set that captures the essential determinants of chemical reactivity while also keeping the phase space of adjustable parameters small enough for reasonable exploration.

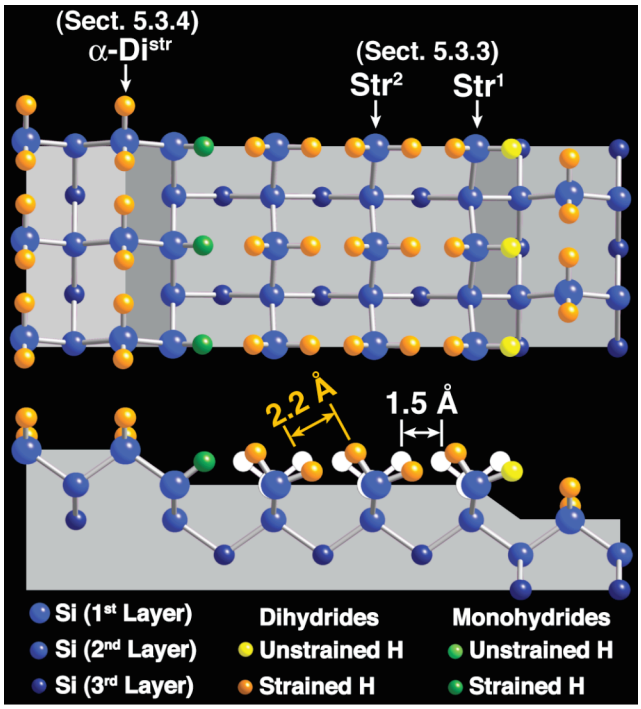

Figure 5.2. Top and side views of the predicted structure of the ideal H-terminated Si(100) surface, showing spontaneous canting of the dihydrides to relieve interadsorbate strain. The bulk-terminated structure is indicated in white for comparison. Different colors are used to represent the strain states of the various H atoms (see key). On this surface, all of the monohydride H atoms are strained. Some of the species introduced in later sections are labeled.

The challenge is illustrated by the stepped H/Si(100) surface in Fig. 5.2. A flat, bulk-terminated H/Si(100) surface would be entirely dihydride terminated. The bulk-terminated terrace geometry is problematic, though, as H atoms on neighboring dihydrides would be only 1.5 Å apart — far below the 2.4 Å van der Waals diameter of H. To partially relieve this interadsorbate strain, simulations of H/Si(100) have predicted a spontaneous canting of the dihydrides,[20–23] as sketched in Fig. 5.2. A flat

H/Si(100) surface was therefore assumed to have a single chemically distinct site — a canted dihydride strained by steric interactions on both sides. All of these sites therefore etch with the same rate.

Steps complicate the structure significantly. As shown in Fig. 5.2, the geometry of the silicon lattice causes dihydrides on adjacent terraces to be rotated by 90°. As a result, there are two step terminations: a highly strained monohydride-terminated step and a dihydride-terminated step. The step dihydride should be chemically distinct from a terrace dihydride, as this species is only strained by interadsorbate interactions on one side. Steps therefore introduce at least two new chemically distinct sites — the step monohydride and the step dihydride — with two different etch rates. This may be an oversimplification, though. The relaxation of the step dihydride will also reduce the strain on the adjacent dihydride. Will this reduced strain introduce a chemically significant change in etch rate? Should a distinct etch rate be used for this species? Similarly, the dihydride that is adjacent to the step monohydride in Fig. 5.2 will be somewhat less strained than a dihydride embedded in an infinite row of strained dihydrides. Should a distinct etch rate be included for this site as well?

A rigorous account of these types of strain-dependent changes in reactivity was far beyond the scope of our simulation. Instead, we took a much simpler tack. We started our investigation with the bare minimum of chemically distinct sites — monohydrides, dihydrides and trihydrides — and explored the morphologies that occurred in this simple parameter space. We then introduced chemical complexity in a stepwise fashion, moving from gross classification strategies (*e.g.,* strained dihydrides versus unstrained dihydrides) to more subtle classifications keeping an eye on our ultimate goal — the simulation of experimentally observed etch morphologies. The site-specific reaction rates extracted from such a simulation will provide chemical

understanding of the effects that control surface reactivity and insights into the relative importance of these effects.

5.2. Computational

Although chemical reactivity is primarily determined by relatively short-range effects, the steady-state morphology of an etched surface is determined by the cumulative effect of many reactions. As a result, etched surfaces often develop morphological features with long characteristic length scales. In extreme cases, anisotropic etching can produce micron-scale features visible under an optical microscope. The development of these features can require extended etching — tens or hundreds of monolayers may need to be removed before the steady-state morphology is reached. These considerations place stringent demands on the speed and efficiency of etching simulators.

The simulator described in the following sections meets these needs. For example, the etching of 100 monolayers from a 1000×1000 Å^2 model surface required less than 5 minutes on a midrange desktop computer (2.16 GHz Intel Core2 Duo running MacOS X). As shown by Fig. 5.3, the calculation time scales as $O(N \ln N)$ where N is the number of atoms in the simulation, making even micron-scale simulations feasible.[24]

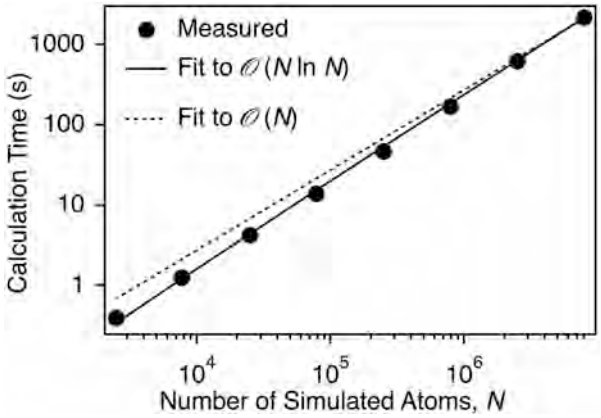

Figure 5.3. The dependence of calculation time on simulation size. The solid and dashed lines represent best fits to $O(N \ln N)$ and $O(N)$ scaling, respectively.

5.2.1. Solid-on-solid model of H/Si(100)

The simulator was based on the solid-on-solid model of surfaces originally developed by Temkin[25] and later extended by others.[26] Our model included the full geometry of the Si(100) lattice, including the 90° rotation of bonds on adjacent terraces, and assumed that each site on the surface was occupied by exactly one silicon atom. In other words, overhangs and inclusions were explicitly forbidden. As a result of this assumption, the three-dimensional etching surface was represented by a two-dimensional array of integers corresponding to the atomic layer of each surface silicon atom. The *x* and *y* directions of the array were aligned with the $[011]$ and $[0\bar{1}1]$ lattice vectors, respectively, as illustrated in Fig. 5.4. When one atom in the surface was etched, a new surface atom that was four atomic layers beneath the original atom was exposed. As a result, the corresponding integer in the array was incremented by four.

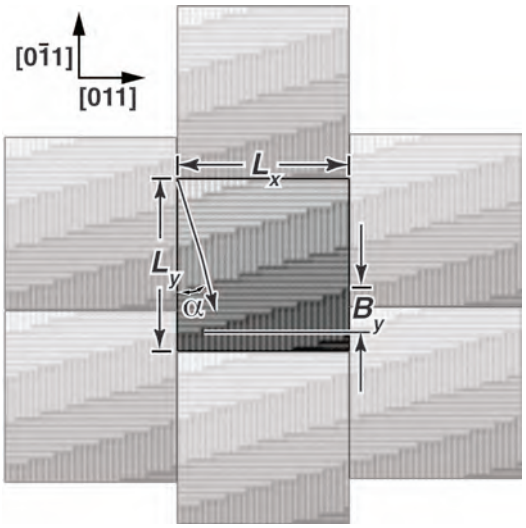

Figure 5.4. Illustration of the boundary conditions used in the simulations. In this grayscale representation of $z(x, y)$, the corrugation of the dihydride rows is visible as faint striations on the terraces.

The model assumed that the surface remained fully H-terminated at all times. When an atom was etched, the dangling bonds created by this process were assumed to be instantly replaced by H atoms. As a result of this assumption, the model did not need to explicitly track the H atoms.

The boundary conditions on the model were chosen to accommodate surfaces of arbitrary miscut angle and miscut orientation, α. An infinite surface was simulated by conformably mapping the finite-sized simulation to the surface of a torus as illustrated schematically by Fig. 5.4. The boundary conditions placed restrictions on the exact size of the surface. Continuity of the simulation across the non-offset boundary required the number of steps in either the *x* or *y* directions, N_x or N_y, be a multiple of four. In Fig. 5.4, this restriction insured that the dihydride rows, visible as lines on the terraces, had the same orientation across the boundaries. In addition, the boundary conditions assumed an integral number of unit cells in both the *x* and *y* directions, which restricted the number of simulated atoms in both the *x* and *y* directions, L_x and L_y, to be even. As a result, the appropriate boundary conditions for the (non-offset) top and bottom boundaries in Fig. 5.4 were

$$h(x,y) = h\left(x, y + L_y\right) + N_y + 1, \tag{1}$$

whereas the appropriate boundary conditions for the (offset) left and right boundaries were

$$h(x,y) = h\left(x + L_x, y - B_y\right) \tag{2}$$

where B_y is the offset in the *y* direction as defined in Fig. 5.4.

A simple grayscale representation of the simulated morphologies had much higher resolution than a typical STM image. For example, the finite radius of an STM tip almost always obscures the corrugation between adjacent dihydride rows on bulk-terminated regions of the surface. To simulate this finite resolution, a pseudo-STM image $I(x, y)$ was defined by

$$I(x,y) = G_5 * z(x,y) \tag{3}$$

where $z(x, y)$ is the height of the surface at position (x, y), G_n is an $n \times n$ Gaussian filter, and * denotes convolution.[27] This processing obscured the small corrugation of a flat surface while preserving single missing rows similar to those seen in Fig. 5.1(c). The

simulated morphologies were sometimes presented in a grayscale representation that combines the linear and differential topographies. This type of "shadowed" representation is commonly used for STM images and emphasizes topological discontinuities (*e.g.,* steps) while also providing information on surface height. The shadowed image $\zeta(x,y)$ is defined by

$$\zeta(x,y) = (1-a)\,I(x,y) + a\,G * \frac{\partial}{\partial \hat{s}} I(x,y) \qquad (4)$$

where *a* is a constant (typically 0.3), and $\hat{s}$ is the direction of the shadow.

5.2.2. Classification of chemically distinct sites

Surface atoms were classified by their local structure, and each class was assigned a class-specific (*i.e.,* site-specific) etch rate prior to any etching. Sites with four bonds to the silicon lattice were assumed to be unreactive. Their etch rate was zero. The etchable sites were first classified on the basis of their local geometry into monohydrides, dihydrides, and trihydrides. These classifications were then further subdivided as needed by the specific simulation. These classifications were always based on local structure *even when the classification was motivated by chemical strain*. For example, dihydrides were sometimes classified into unstrained dihydrides, dihydrides strained by steric interactions on one side, and dihydrides strained by steric interactions on both sides. No attempt was made to calculate the local stress or the distortion of the individual surface sites in making these classifications.

In some simulations, the site classifications became complex, requiring an examination of the surface structure out to the fourth-nearest neighbor. For pedagogical simplicity, these classifications are presented as needed in the Results section.

5.2.3. Etching algorithm

During the simulation, single silicon atoms were randomly removed from the surface in accordance with predefined, site-specific etch rates. Diffusion of surface atoms and redeposition of etched atoms were forbidden. The etch rates were input

parameters to the simulation and were chosen by the user. No attempt was made to calculate or predict the etch rates. The ultimate goal of the simulations is to find regions of the etch rate phase space that reproduce experimentally observed etch morphologies. Examples of this type of analysis on H/Si(111) are given in Refs. 4 and 5.

Monte Carlo algorithms have been extensively reviewed.[28] Qualitatively, there are two types of kinetic Monte Carlo simulations. The first type visits individual sites in some order (possibly randomly). At each site, the simulation computes a random number which is then compared to the site's etch rate to determine whether the site will be etched. Although easy to implement, this algorithm is often very inefficient for anisotropic etching simulations. Since defect (*i.e.,* minority) sites are typically many orders of magnitude more reactive than the majority species, most simulation time is spent visiting sites that do not etch. The second type of simulation uses a random number to calculate which site on the surface will be the next to etch and then removes that site. This algorithm requires significantly more bookkeeping than the first, but is often much faster. Our model used the second algorithm type.

The implementation of the etching algorithm was substantially identical to that described by Flidr *et al.,*[8] so the extensive description of the algorithm included in Ref. 8 will not be repeated.

Most simulations started from a possibly miscut but otherwise defect-free surface. The surfaces were etched until the morphology reached steady state as judged by statistical metrics, such as site densities. To test for possible "memory" effects, a limited number of simulations were started from other morphologies (*e.g.,* a randomly etched surface with the same miscut); however, the steady-state morphologies were always independent of the initial morphology.

5.3. Results[i]

Our exploration of the etch rate phase space started from the simplest possible classification scheme and became increasingly complex. Our goal was the correlation of general reactivity trends with specific types of etch morphologies.

To make the search of a very large phase space manageable, our exploration was guided by experimental observations, particularly with respect to the reactivity of surface monohydrides and trihydrides. Although early spectroscopic investigations suggested that anisotropically etched Si(100) surfaces were covered by a significant density of silicon trihydrides,[29] reanalysis of these data with new techniques has cast doubt on this interpretation. Furthermore, no trihydrides were observed in STM images of Si(100) surfaces etched in water[6] and in NH_4F (aq).[7] The absence (or low density) of trihydrides suggests that these sites are rapidly etched, at least by the etchants examined in STM to date. As a result, all of the following simulations assumed that trihydrides etched much more rapidly than other sites. For simplicity, an infinitely fast trihydride etch rate was assumed.

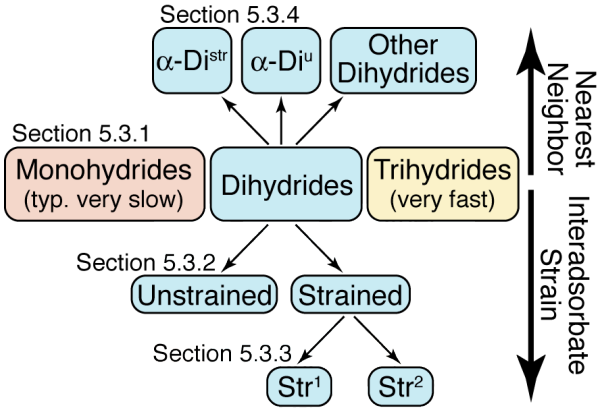

Figure 5.5. A schematic representation of the various classifications of site-specific reactivities used in this study. Sections 5.3.1 - 5.3.3 classify dihydride reactivity on the basis of interadsorbate strain. Section 5.3.4 also considers nearest-neighbor structure.

[i] The list of etch rates used in the simulations in various models are included in Appendix B

Figure 5.5 gives a graphical overview of the structure of this section and the kinetic regimes that have been explored. Previous experimental and computational studies of Si(111) etching have come to the general conclusion that silicon trihydrides are highly reactive and that unstrained monohydrides are fairly unreactive. Much less is known about the reactivity of silicon dihydride species. In the first three sections, dihydride reactivity is assumed to be primarily governed by interadsorbate strain. Although strain is expected to weaken chemical bonds (thereby increasing reactivity), steric effects can also increase reaction barriers (thereby lowering reactivity). For completeness, we allowed interadsorbate strain to either increase or decrease reactivity. In spite of this, models that classified dihydride reactivity solely on the basis of interadsorbate strain were unable to replicate the morphology of NH_4F-etched Si(100). Because of this, the model described in the fourth section classifies dihydride reactivity on the basis of nearest-neighbor bonding, thereby reproducing the most significant morphological features of NH_4F/Si(100) etching.

The morphologies presented in subsequent sections show arbitrary regions of larger (typically 770×770 Å^2) simulations.

5.3.1. Bond-Counting Model of Reactivity

Our simplest model of reactivity was based on bond counting. The etchable sites were divided into three categories: monohydrides, dihydrides, and trihydrides. Since trihydrides were assumed to react infinitely quickly, the morphologies were determined by a single parameter, the ratio of the dihydride and monohydride etch rates k(Di)/k(Mono).[30] This model was similar to that originally introduced by Camon *et al.*[31–33] for the modeling of the face-specific etch rates of silicon.

This simple model invariably led to rough, featureless Si(100) surfaces as illustrated by the representative steady-state morphologies in Fig. 5.6. In the regime where the etch rates followed the rule

Trihydrides >> Dihydrides >> Monohydrides, (5)

the etch rate ratio had only subtle effects on the morphology, and no characteristic etch features developed even when the anisotropy was very large (up to 10^{10}:1).

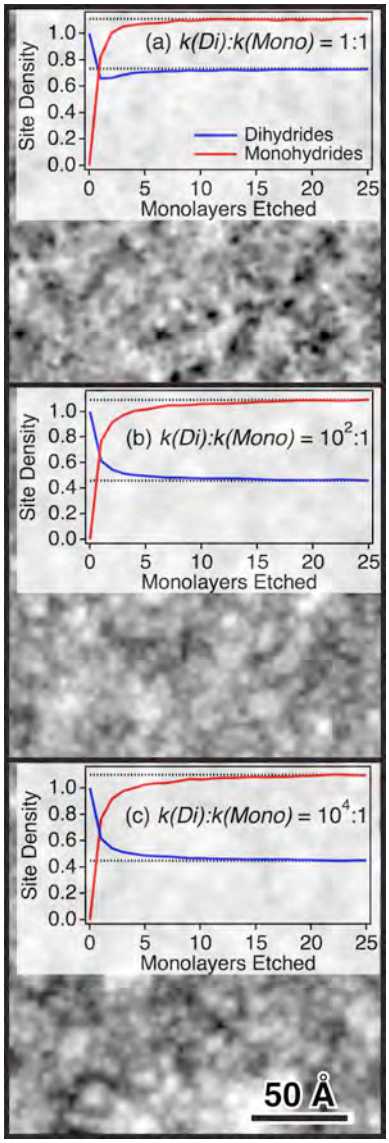

Figure 5.6. Representative morphologies generated by the bond-counting model of reactivity. Trihydrides etched infinitely quickly, whereas the relative etch rates of dihydrides to monohydrides were (a) 1:1, (b) 100:1, and (c) 10,000:1. The site densities (insets) reached steady state after the removal of ~10 monolayers from an initially flat, defect-free surface.

In the regime where k(Mono) >> k(Di), the simulated morphologies became much rougher, as illustrated by the representative cross-sections in Fig. 5.7, but there was still no tendency towards facet formation. This roughness could be rationalized on the basis of the relative unreactivity of the terrace (dihydride) sites. In this regime, the terrace sites effectively act as temporary etch masks that protect the surface underneath, while the high reactivity of the monohydride sites leads to rapid etching of more vertical features. In concert, these two effects produced tall etch spires. Importantly, the near-vertical sidewalls in Figs. 5.7(a) and 5.7(b) strongly suggest that this regime is not appropriately modeled with the solid-on-solid approximation. In this regime, undercutting reactions likely play an important role. By artificially eliminating such reactions, the model likely overestimated the roughness of the etched surface.

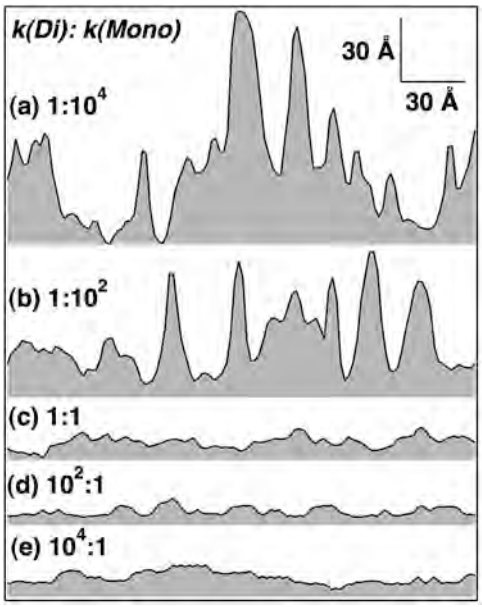

Figure 5.7. Representative cross-sections generated by the bond-counting model of reactivity. The relative etch rates of dihydrides to monohydrides were (a) 1:10,000, (b) 1:100, (c) 1:1, (d) 100:1, and (e) 10,000:1. When monohydrides etched much faster than dihydrides, very rough surfaces were produced, calling the solid-on-solid approximation into question.

From a practical standpoint, the potential failure of the solid-on-solid approximation on very rough surfaces was not too concerning, as our primary goal was

modeling morphologies observed in STM. Because of the finite size of the probe, steeply sloped surfaces are notoriously difficult to image in STM. Thus, experiment and simulation fail under similar conditions.

For the remaining examples, we concentrate primarily on the regime $k(\mathrm{Di}) \gtrsim k(\mathrm{Mono})$ for two reasons. First and most importantly, the most common anisotropic silicon etchants produce near-atomically-flat Si{111} surfaces. Atomic-scale studies of a number of these etchants explained this behavior in terms of the relative unreactivity of the bulk-terminated Si(111) surface, which is terminated by an unstrained monohydride species. For example, aqueous NH_4F solutions etch dihydride defects on Si(111) surfaces five to six orders of magnitude more rapidly than the unstrained monohydride site.[4,5] Second, this restriction avoided the production of very rough surfaces.

5.3.2. Dihydride Strain and Pyramid Formation

The bond-counting model of Si(100) reactivity neglected the potential effects of interadsorbate strain on chemical reactivity. Our next reactivity model introduced strain in the simplest possible fashion by defining four types of surface species: monohydrides, unstrained dihydrides, strained dihydrides, and trihydrides. This model did not distinguish between dihydride species with different amounts of strain (*e.g.,* sites strained by interadsorbate interactions on one or two sides), nor did it distinguish between strained and unstrained monohydrides.

The morphologies generated by this model fell into two general categories: microfaceted and rough. To illustrate this dichotomy, the series of morphologies in Fig. 5.8 were generated by fixing the ratio of the etch rates of the slowest etching dihydrides (*i.e.,* strained or unstrained, depending on the simulation) and the monohydrides to 10^4, and then systematically varying the etch rate of the faster etching dihydrides. When the

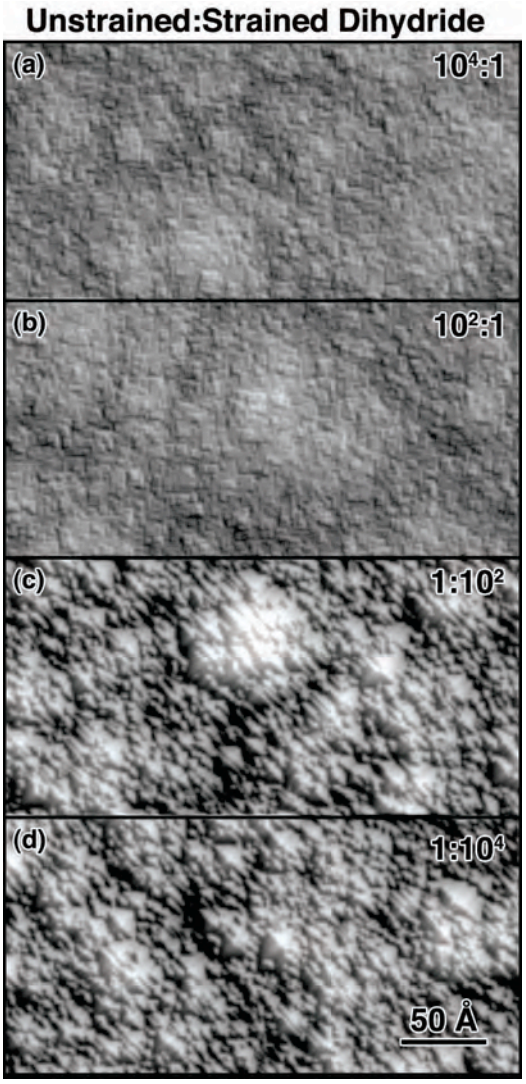

Figure 5.8. Representative morphologies generated by a model with four etchable species: very-fast-etching trihydrides, strained dihydrides, unstrained dihydrides, and slow-etching monohydrides. As described further in the text, the relative etch rates of the unstrained: strained dihydrides were (a) 10,000:1, (b) 100:1, (c) 1:100, and (d) 1:10,000. When the unstrained dihydrides etched more slowly than the strained dihydrides, pyramidal hillocks were formed.

unstrained dihydrides etched much faster than the strained dihydrides, the steady-state morphologies were rough and featureless, as illustrated by Fig. 5.8(a) and 5.8(b). In contrast, when the strained dihydrides etched significantly faster than the unstrained dihydrides, the surface spontaneously formed roughly tetrahedral hillocks, as shown by Figs. 5.8(c) and 5.8(d). The pyramidal shape of the hillocks is more easily visualized in

Fig. 5.9 which shows a three-dimensional image of a small region of the simulated surface. The size and shape of the hillocks were relatively insensitive to the anisotropy of the dihydride etch rates.

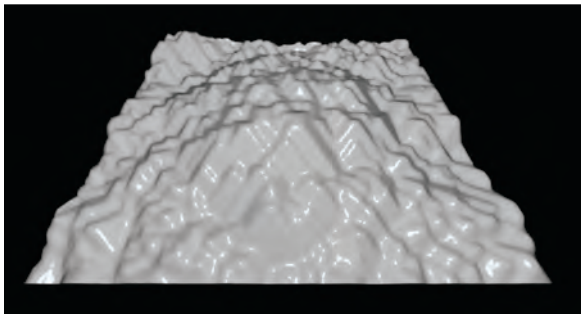

Figure 5.9. Three-dimensional rendered image of a small region (80 Å × 90 Å) of the surface in Fig. 5.8(c) showing the microfaceted hillock structure.

Table 5.1: Relative densities of sites on a (111)-microfaceted etched surface such as that in Fig. 5.9. Both (111)-like and (110)-like monohydrides are unstrained.

Site Type		Density
Monohydrides	(111)-like	23.2%
	(110)-like	50.2%
	Strained	20.5%
Dihydrides	Unstrained	6.0%
	Strained	0.005%
Trihydrides	All	0.0%

The nature of the faceted surface was best understood from the types of sites expressed on the surface as shown in Table 5.1.[34] In general, when the etch rates followed the paradigm

Trihydrides >> Strained dihydrides >> Unstrained dihydrides >> Monohydrides, (6)

the etched surface spontaneously formed {111}-faced pyramidal microfacets. The edges of the microfacets were decorated with chains of silicon monohydrides that resembled the bulk-terminated Si(110) surface, whereas the bases of the pyramids were primarily terminated by strained monohydride species. The micropyramid tops were terminated

by a single unstrained dihydride. This structure is illustrated by the site map in Fig. 5.10. Even though the pyramids were {111}-faced, (110)-like monohydrides outnumbered (111)-like monohydrides by a factor of two. This conundrum was explained by the relatively high density of monohydrides on (110)-faces (represented by red dots in Fig. 5.10) as well as the small height of the micropyramids.

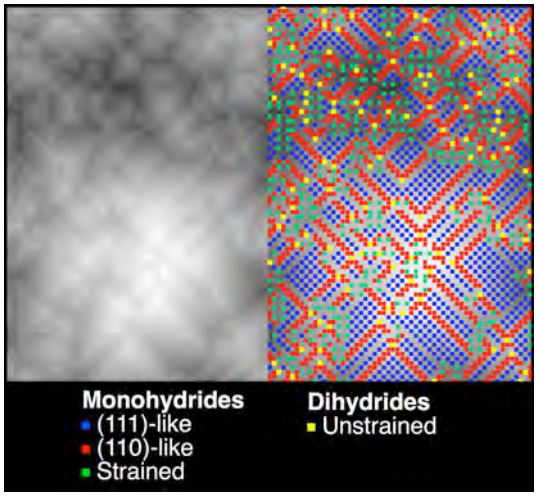

Figure 5.10. The pyramidal structure of the hillocks is shown in (left) grey-scale representation of 110 Å × 160 Å region of the surface in Fig. 5.8(c) and (right) same region of surface with overlay of all silicon hydride species. The {111} faces and {110} edges are decorated with (111)- and (110)-like monohydrides, respectively. The hillock apices are terminated by a single unstrained dihydride.

Since the microfaceted surface was almost entirely devoid of strained dihydride sites, one might reasonably ask whether this morphology was sensitive to the etch rate of the strained dihydride. For example, if this surface were placed in an etchant that attacked all dihydrides at the same rate, would the surface remain microfaceted or would it revert to the rough morphology discussed in the previous section?

To answer this question, we first etched 250 monolayers from an initially flat surface under the conditions described by Eq. (6) to form a microfaceted surface. We then abruptly reduced the rate of strained dihydride etching to equal that of unstrained dihydride etching [*i.e.,,* Eq. (5)]. The results of this experiment are shown in Fig. 5.11.

The change in etch kinetics resulted in a rapid and dramatic change in the etched surface morphology. The microfacets were rapidly removed and replaced by a rough, featureless morphology. For comparison, an initially flat surface was etched using the second set of kinetics [*i.e.,* Eq. (5)] until the site densities reached steady state. The steady-state densities are indicated by the dotted lines in Fig. 5.11. A comparison of the solid and dotted lines in Fig. 5.11 confirmed that the two surfaces reached the same steady-state morphology irrespective of the starting surface.

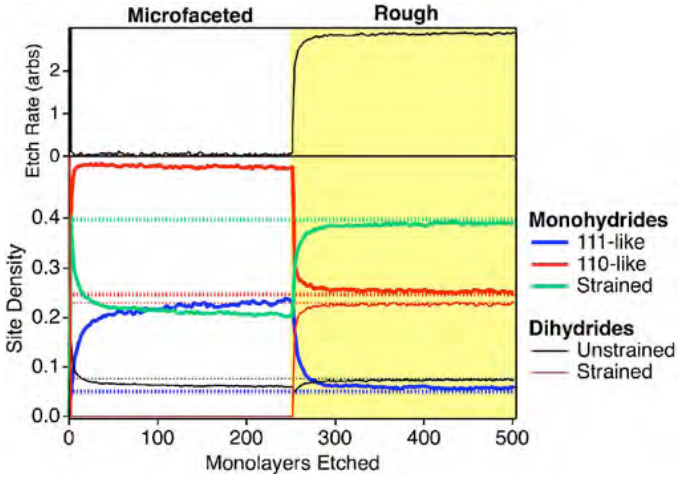

Figure. 5.11. The (top) etch rates and (bottom) site densities of various surface species (solid lines) as a function of etch depth. Starting from a flat, defect-free surface, atoms were removed using the kinetics of Eq. (6), and a microfaceted morphology developed. After 250 monolayers were removed, the kinetics were instantaneously changed to match Eq. (5). The surface quickly assumed a rough morphology. The dotted lines represent the steady-state site densities of a flat, defect-free surface etched solely using the kinetics of Eq. (5).

To conclude this section, we note that this reactivity model cannot reproduce the variety of morphologies observed experimentally. Although Si(100) surfaces etched in pure deoxygenated H_2O develop hillocks with four-fold symmetry [see Fig. 5.1(a)] that could conceivably be related to the microfacet formation observed in Fig. 5.9, a larger parameter space is clearly needed to reproduce the entire morphology.

5.3.3. Dihydride Strain and Strained Row Formation

Our next model of reactivity drew inspiration from the morphology of NH_4F-etched Si(100) surfaces shown in Fig. 5.1(c). The production of long, unbroken rows of silicon atoms implied that the etchant attacked row-end sites much faster than mid-row sites. One plausible explanation for this differentiation could be the amount of strain in different dihydride species. For example, Fig. 5.2 suggests there are at least three different types of dihydride species: unstrained dihydrides, dihydrides strained by interadsorbate interactions on one side (Str^1-Di), and dihydrides strained on both sides (Str^2-Di). Our next model of reactivity accounted for these differences by defining two types of strained dihydrides with independently adjustable etch rates. Again, we concentrated on the regime where trihydrides were much more reactive than other species, and monohydrides were the least reactive species.

The morphologies generated by this model fell into three general categories: striped (*S*), microfaceted (*M*) and rough (*R*). Although these morphologies could typically be distinguished by eye, they could also be distinguished by the density of (111)- and (110)-like monohydrides on the etched surfaces. These types of sites were in the majority on microfaceted surfaces (≥50%), in the minority on striped surfaces (≤ 15%), and represented a significant fraction (~1/3) of rough surfaces.[35] To illustrate this, the series of morphologies in Fig. 5.12 were generated by fixing the ratio of the etch rates of the unstrained dihydrides and the monohydrides to 10^4, and then systematically varying the etch rate of the Str^1 and Str^2 dihydrides. The transitions between the morphological categories were not sharp; they occurred over a range of etch rates. For example, the morphology in Fig. 5.12(a4) was dominated by stripes; however, a few microfaceted hillocks were also observed.

Three general rules emerged from these simulations (and many others). First, microfaceted hillocks formed whenever the unstrained dihydrides were less reactive

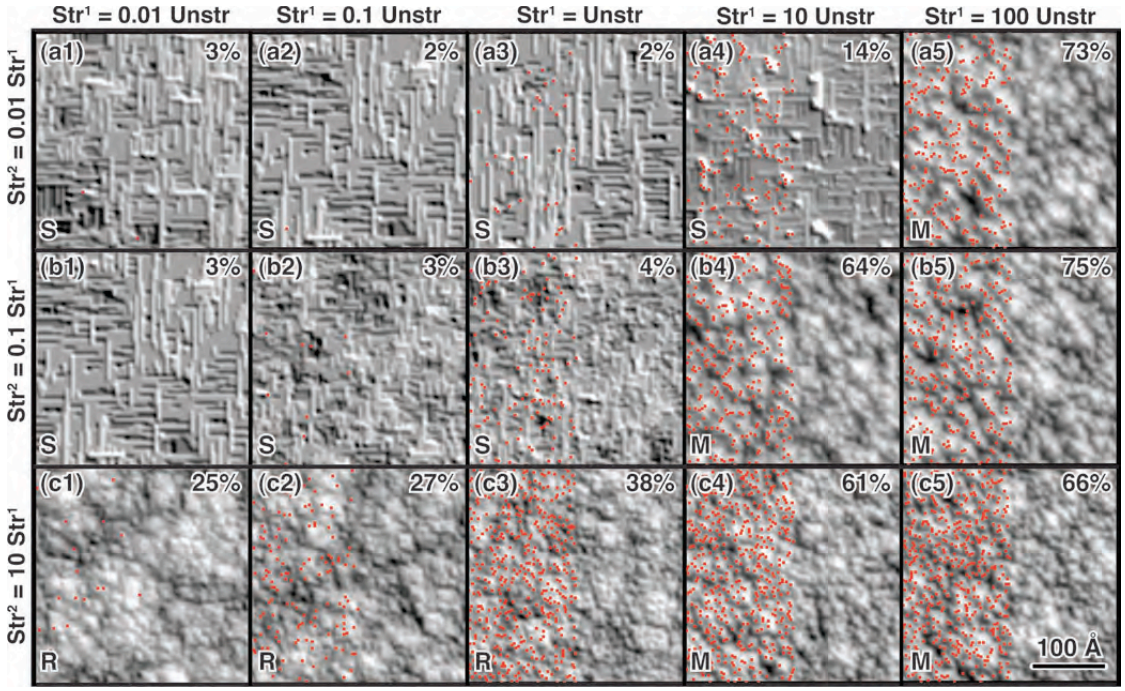

Figure. 5.12: Representative morphologies generated by a model with five species: very-fast-etching trihydrides, unstrained dihydrides, dihydrides strained by interadsorbate interactions on one side (Str^1-Di), dihydrides strained on both sides (Str^2-Di), and slow-etching monohydrides. The red dots on the left-hand side of each morphology indicate the positions of all unstrained dihydrides. The density of (111)- and (110)-like monohydrides are indicated by the percentages in the upper-right-hand corner of each image, whereas the letters indicate striped (*S*), microfaceted (*M*) and rough (*R*) morphologies. This model lead to the production of stripes of *strained* dihydrides.

than the strained dihydrides. This stability criterion was explained by the structure of the pyramidal hillocks: four {111} faces intersecting in four {110} edges and capped by a single unstrained dihydride. Under the conditions studied here, the faces and edges of the pyramids were always very unreactive, as they were terminated by unstrained monohydrides. The pyramid stability criterion also dictated that the apex site, an unstrained dihydride, had to be relatively unreactive. Second, if the etch kinetics did not favor microfacet formation, stripes would form if Str^1-dihydrides etched more quickly

than Str^2-dihydrides. For example, stripes sometimes formed in rows (a) and (b) of Fig. 5.12, but never in row (c). In plain language, this criterion simply required row-end sites to etch more quickly than mid-row sites. Finally, if the etch kinetics favored stripe formation, the average stripe length was controlled by the relative etch rates of the row-end (Str^1-Di) and mid-row (Str^2-Di) etch rates. For example, the stripes in Figs. 5.12(a2) and 5.12(a3) were longer than the stripes in Figs. 5.12(b2) and 5.12(b3), respectively.

The morphology in Fig. 5.12(a4) is an interesting intermediate case. In this case, the unstrained dihydrides, which terminated pyramid apices, were somewhat more reactive than the Str^2-dihydrides, which formed the mid-row sites in stripes. As a result, the morphology was dominated by stripes; however, a few microfaceted hillocks also formed. This morphology had some similarities to those observed on Si(100) surfaces etched in deoxygenated H_2O [see Fig. 5.1(a)]; however, more work is needed to determine whether this similarity is more than coincidental.

Although the striped morphologies in Fig. 5.12 bore some resemblance to those generated by NH_4F etching [see Fig. 5.1(c)], they differed in one very important respect. The stripes generated by the simulations in this section were composed of strained dihydrides, whereas spectroscopic investigation of the NH_4F-etched surface[7] showed the surface was terminated by single-atom-wide rows of unstrained dihydrides. For example in Fig. 5.12, all of the unstrained dihydrides in the left half of each image are indicated by small red dots. The strained nature of the single-atom-wide stripes is reflected in the near-complete absence of red dots on the stripes.

5.3.4. α-Dihydrides and Unstrained Row Formation

Our final model of reactivity was designed to produce single-atom-wide rows of unstrained dihydrides similar to those produced by NH_4F etching. The structure of these rows is shown in the top panel of Fig. 5.13. As discussed in the previous section, stripe formation implies that row-end sites etch faster than mid-row sites; however, the

identity of the fast etching site is unclear from Fig. 5.13. Does the etchant attack the terminal monohydride or the dihydride adjacent to the terminal monohydride?

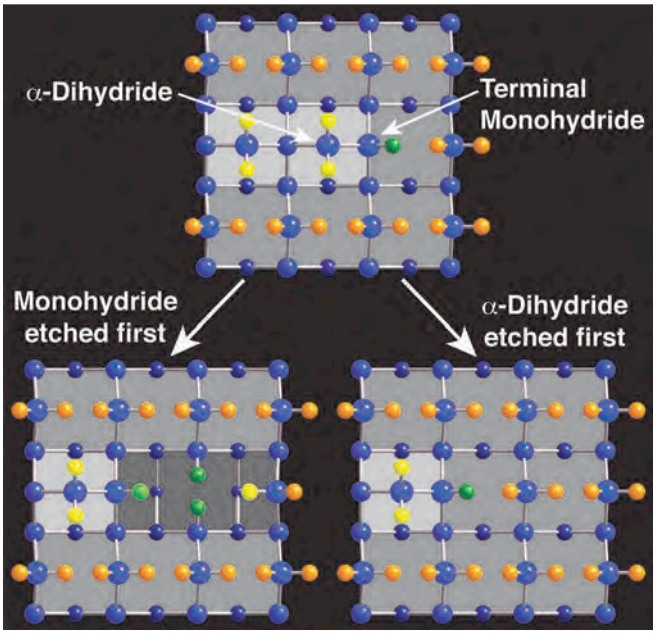

Figure 5.13. The two possible pathways for etching the end of an unstrained dihydride row. If the row-end monohydride was etched first, two monolayers would be removed, whereas if the α-dihydride site was etched first, a single monolayer would be removed. Only the latter pathway is consistent with the circled regions in Fig. 5.1(b).

For the case of NH_4F etching, this question can be answered unambiguously from the steady-state morphology in Fig. 5.1(c). The clue was the production of stripes of alternating orientation in near vicinity to one another as indicated by the circles in Fig. 5.1(c). If the terminal monohydride site were the first to etch, etching of this site would cause the adjacent dihydride to become a trihydride. This site would then rapidly etch. As a result of these two events, etching of the terminal monohydride would lead to the removal of two atomic layers — the unstrained dihydride layer and the monohydride layer as seen in Fig. 5.13. This was not observed. Instead, stripe etching revealed new stripes with an orthogonal orientation *one layer below*— clear evidence of single-atomic-layer etching. The second possibility was consistent with this type of etching. If the dihydride adjacent to the terminal monohydride were the first to etch, the

terminal monohydride would be converted to a dihydride in the plane below the stripe. In contrast with a trihydride, this site would not (necessarily) etch immediately. As a result, only the second mechanism — rapid etching of the dihydride adjacent to the row-end monohydride — was consistent with layer-by-layer etching.

The distinguishing characteristic of the row-end dihydride is its proximity to a monohydride. In analogy with organic chemistry nomenclature, we call these sites "α-dihydrides" as they occupy the α position with respect to a monohydride. For lack of a better term, we refer to dihydrides that are not α to a monohydride as "normal" dihydrides.

Our final model of reactivity explored the effects of α-dihydride etching by defining two types of α dihydrides with independently adjustable etch rates: dihydrides that were α to an unstrained monohydride (α-Di^{u}) and dihydrides that were α to a strained monohydride (α-Di^{str}). For these exploratory simulations, the potential effects of dihydride strain were ignored: Strained and unstrained dihydrides were assumed to etch with identical rates. As in previous sections, we concentrated on the regime in which trihydrides were much more reactive than other species, and monohydrides were the least reactive species.

As in the previous section, the morphologies generated by this model fell into three general categories: striped (*S*), microfaceted (*M*) and rough (*R*). To illustrate the regimes, the series of morphologies in Fig. 5.14 were generated by fixing the ratio of the etch rates of the unstrained dihydrides to the monohydrides at 10^4, and then systematically varying the etch rate of the α-Di^{u} and α-Di^{str} dihydrides. To aid in the interpretation of these morphologies, all of the unstrained dihydrides in the left half of each image are indicated by small red dots. As in the previous case, the transitions between the morphologies were not sharp; they occurred over a range of etch rates. For

example, the morphology in Fig. 5.14(a5) was dominated by stripes; however, a few microfaceted hillocks were also observed.

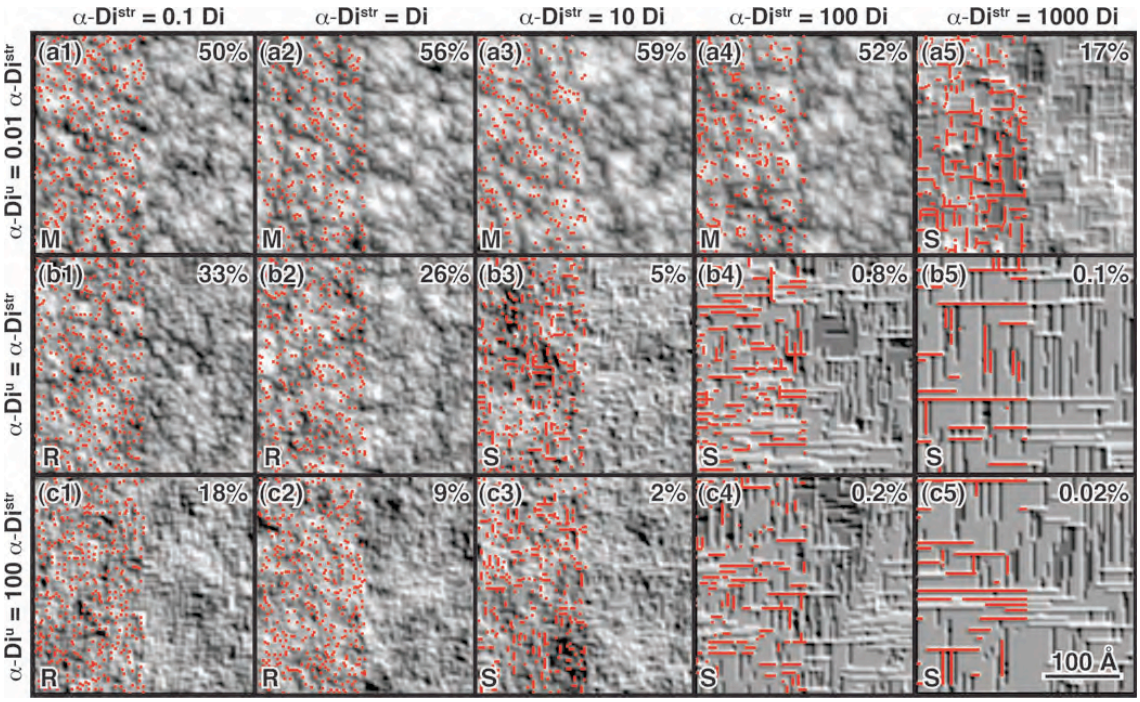

Figure 5.14. Representative morphologies generated by a model with five species: very-fast-etching trihydrides, dihydrides that were α to an unstrained monohydride (α-Di^{u}), dihydrides that were α to a strained monohydride (α-Di^{str}), "normal" dihydrides, and slow-etching monohydrides. In this model, dihydride strain had no effect on etch rate. The annotations and red dots have the same meaning as in Fig. 5.12. This model lead to the production of stripes of *unstrained* dihydrides.

A number of general rules emerged from these simulations (and others). First, the formation of microfaceted hillocks required the apex site, an α-Di^{u} site, to be relatively unreactive compared to all other dihydride species. This criterion is essentially the same as noted in Section 5.3.3. and was met by the simulations in Figs. 5.14(a1) – (a4). In this regime, $k(\alpha\text{-Di}^{u}) \leq k(\text{Di})$. Second, if the etch kinetics did not favor microfacet formation, stripes formed when the α-Di^{str} sites etched faster than "normal" dihydrides. In other words, stripes formed when row-end sites (α-Di^{str}) etched faster than the mid-row sites (Di). As in the previous section, the average stripe length

was controlled by the relative etch rates of the row-end (α-Di^{str}) and mid-row (Di) sites, with faster row-end etching favoring longer stripes. Finally, if the etch kinetics did not favor microfacet formation, the etch rate of unstrained α-dihydrides had only subtle effects on the etch morphology.

The principal difference between this model and the previous model was the structure of the stripes. This model generated stripes terminated with unstrained dihydrides, whereas the previous model generated stripes of strained dihydrides. This difference is almost impossible to distinguish by eye from the simulated or the experimental morphologies; however, the two cases can be distinguished experimentally using polarized infrared absorption spectroscopy.[7]

Although some of the simulations in Fig. 5.14 bear a resemblance to those generated by NH_4F (aq.) etching [see Fig. 5.1(c)], significant differences remain. Most notably, NH_4F (aq.) preferentially removes alternating rows of dihydrides on the etching surface leading to a "missing row" morphology. In contrast, the etch kinetics described in this section etch dihydride rows randomly; there is no correlation between the missing rows and no propensity for an alternating row morphology. In addition, NH_4F (aq.) etching does not produce the significant regions of flat Si(100) observed in Fig. 5.14.

5.3.5. More Complicated Models of Reactivity

The simple models described in the previous sections cannot adequately reproduce all aspects of the experimental morphologies observed to date. The next step in complexity would be to define a model that distinguishes between strained and unstrained dihydrides as well as between "regular" and α-dihydrides. At a minimum, such a model would have to include six types of dihydride species (Di, Str^1-Di, Str^2-Di, α-Di, α-Str^1-Di, α-Str^2-Di) and potentially more. While computationally quite tractable (and indeed already implemented), this extension expands the phase space of kinetic

parameters tremendously. A general exposition on this expanded phase space (such as that presented in the previous sections) would be quite tedious. Simulations of specific surface morphologies, such as those presented in Fig. 5.1, require a targeted approach that will be discussed in subsequent manuscripts.

5.4. Discussion

The simulations presented in the previous section were illustrative, not exhaustive, and focused on regions of kinetic phase space suggested by previous studies of aqueous anisotropic silicon etchants. In particular, most of these etchants produce flat or nearly flat Si(111) surfaces, so unstrained monohydride species were assumed to etch very slowly. Similarly, trihydrides have not been definitively observed on etched silicon surfaces, so these sites were assumed to etch very quickly. In spite of these restrictions, a variety of etch morphologies were observed.

5.4.1. α-Dihydrides and the Reactivity of Other Si Faces

The most interesting (and unexpected) conclusion to emerge from these studies is that some etchants discriminate between "normal" dihydrides and those that are α to a monohydride. For example, a cursory comparison of the morphology of Si(100) surfaces etched in NH_4F (aq.) solutions [Fig. 5.1(c)] and our simulations in Fig. 5.13 suggests (but does not prove) that this solution etches α-dihydrides *orders of magnitude faster* than normal dihydrides.

Although unexpected, this conclusion is supported by observations on other silicon faces. For example, when Si(110) surfaces are etched in NH_4F (aq.) solutions, the etched surfaces are characterized by long chains of silicon monohydrides.[36–38] As in our simulations, the production of long chains implies that the row-end species, which is an α-dihydride on Si(110) surfaces, etches much more quickly than the mid-row sites, which are monohydrides. Although detailed simulations of the etching of Si(110) surfaces have yet to be performed, the experimental data lead us to predict that the α-

dihydride is one of the fastest etching sites on the Si(110) surface.[39] Similarly, when Si(111) surfaces are etched in aqueous NH_4F solutions, the most reactive stable site[39] on the surface is a "kink" site, which consists of a strained dihydride that is α to a monohydride.[40] Although structural considerations have led previous researchers to suggest that the monohydride etches before the α-dihydride,[5] the converse cannot be definitively ruled out. Although more work is clearly needed, we tentatively suggest that the highly anisotropic etching of the three major silicon faces in NH_4F (aq.) solutions may be explained in large part by the high reactivity of α-dihydride sites.

5.4.2. Etch Rates and Facet Formation

A second interesting conclusion is that the low chemical reactivity of monohydride sites — and, by extension, of the monohydride-terminated ideal Si{111} and Si{110} faces — leads to the formation of microfaceted pyramidal hillocks under some, *but not all,* conditions. This observation is more than an intellectual curiosity, as the silicon solar cell industry is actively searching for inexpensive, environmentally friendly means of producing pyramidally textured, low reflectance Si(100) surfaces.[41–43] The nanoscale pyramids produced by these simulations are smaller than envisioned for these applications, so further research into the mechanisms that control pyramid size are warranted. We caution that nanoscale pyramidal texturing may be difficult to observe with scanned probe microscopies because of tip size effects. Infrared absorption spectroscopy of the sharp vibrational resonances associated with the Si–H monohydride stretch mode[44–46] on Si{111} and Si{110} may be a more reliable monitor.

The formation of microfaceted pyramidal hillocks during etching of Si(100) has been observed in a variety of etchants and under a variety of conditions; however, this effect has usually been attributed to local masking of the surface by deposited impurities,[47] etch products[48–50] or gas bubbles.[51–54] These mechanisms assume that the apex of every pyramid is decorated by an adsorbed impurity or a gas bubble. A different

mechanism was operative in our simulations — a mechanism that is *intrinsic* to the etchant, requiring no impurity or bubble formation. In our mechanism, the apex of each hillock was decorated with a slow etching species (an unstrained dihydride in Section 5.3.3 and an α-Di^{u} in Section 5.3.4). This site had a finite etch probability; however, subsequent etching of the hillock typically led to the creation of a new slow-etching site of the same type. As a result, the hillocks were dynamic and self-propagating.

The formation of facets on crystals *in equilibrium* has been extensively studied both experimentally and theoretically.[55] Given sufficient time, a crystal will adopt an equilibrium shape that minimizes its surface tension (*i.e.,* its surface free energy per unit area). This shape can be predicted from a polar plot of surface tension using the Wulff construction.[56] Similarly, an initially flat surface will spontaneously facet if this restructuring leads to a lower surface tension.[57] Therefore, the structure of the faceted surface can also be predicted from the orientation-dependent surface tension.

Etched surfaces are not, however, in equilibrium, and the steady-state etch morphology is kinetically, not thermodynamically, determined. Nevertheless, the elegant interconnection between equilibrium crystal shape and surface tension raises the question as to whether some orientation-dependent parameter, such as etch rate, plays an analogous role in determining the steady state morphology. Indeed, face-dependent etch rates have been used to explain the stability of micron-scale etch hillocks and pits during etching.[58] On the basis of these ideas, Jaccodine[59] suggested that the steady-state etch morphology will minimize the total "etch action," defined by

$$\int k_{\mathbf{n}}\, dA \tag{7}$$

where $k_{\mathbf{n}}$ is the etch rate in direction **n**, for a fixed total volume. Using similar reasoning, others suggested that the exceedingly slow etch rate of some anisotropic etchants towards Si(111) leads to (111)-microfaceting of etched Si(100) surfaces.[44,60]

Our simulations show that the steady state morphology *does not necessarily* minimize the etch action at the atomic scale. The corollary to this is that the existence of a very slow etching face will not necessarily lead to the etching-induced faceting of other faces. For example, consider the experiment described by Fig. 5.11 in which one set of kinetics was used to prepare a microfaceted surface, then the etch rates were changed instantaneously after 250 monolayers of etching. Immediately after the change, the surface had a calculated etch rate of 0.693 (in arbitrary units). The morphology then evolved in response to the changed kinetics, causing the etch rate to *rise* to 2.89. In this case, the steady state morphology had a higher etch action than the "initial" surface, directly contradicting the etch action theorem.

Although simulations show that the steady state etch morphology did not minimize the etch action, we have yet to find a simple, generalizable predictor of the steady-state etch morphology. Simulations show that the steady-state morphology is often sensitive to the etch rate of species that make up a small fraction of the surface.

5.4.3. Unique Determination of Etch Rates

A major outstanding question is to what extent (and under what conditions) site-specific etch rates can be uniquely determined from experimental investigations of anisotropically etched crystals, as many different sets of etch rates led to similar final morphologies. Two points are clear. First, the etchant must generate characteristic features (as opposed to randomly rough surfaces) for this approach to be viable. Second, even under the best circumstances, experimental morphologies will be consistent with a range of etch rates, not a specific set of etch rates. Additionally, kinetic investigations have well known difficulties quantifying the rates of rapid reactions that occur subsequent to a slow (*e.g.,* rate-determining) reaction. For example, kinetic investigations may only be able to put a lower bound on the reactivity of silicon trihydrides.

Our simulations clearly showed that morphological investigations of a single surface do not *in general* contain sufficient information for the unique determination of site-specific etch rates. For example, nearly identical morphologies with single-atom-wide stripes were formed from the rapid etching of Str^1-dihydrides (Section 5.3.3) or α-dihydrides (Section 5.3.4). Most morphological probes cannot distinguish between these two cases. (Under very favorable conditions, silicon dihydrides appear elliptical in STM images, with the long axis of the ellipse being parallel to the plane of the dihydride.[7,22])

Nevertheless, many of these limitations can be counteracted experimentally. First, information gained from structural and chemical probes, such as vibrational spectroscopy, complements the information contained in the morphology. Such information can significantly limit the phase space to be searched. Second, this initial investigation concentrated on the etching of flat surfaces, but even more information can be obtained from the etching of vicinal surfaces. In a sense, vicinal surfaces place different boundary conditions on etching, as these surfaces are constrained to have an increased concentration of certain types of defect sites (*e.g.,* step sites). In some cases, vicinal surfaces may etch in an entirely different manner than flat surfaces (*e.g.,* step flow etching versus pit nucleation and growth). For the specific case of Si(100) etching, step doubling has been observed on NH_4F-etched surfaces miscut by 3.5° towards the [011] direction. Does this behavior provide additional clues to the underlying chemistry, perhaps indicating a particularly stable step edge structure? Finally, investigations can be guided by the study of a number of low-index faces. For example, chains of unstrained monohydrides appear on flat Si(110) surfaces, the step edges of Si(111) surfaces miscut in the $\langle \bar{1}\bar{1}2 \rangle$ direction, and on the edges of micropyramidal hillocks on Si(100) surfaces. Presumably all of these sites etch with comparable etch rates.

5.5. Conclusions

An atomistic and chemically realistic kinetic Monte Carlo simulator of the anisotropic etching of flat and vicinal Si(100) surfaces was developed. The model classified silicon atoms on the basis of their local structure; all atoms of each class were etched with the same rate. The challenge was in defining a minimal set of chemically distinct etch sites that captured the essential determinants of chemical reactivity while also keeping the phase space of adjustable parameters small enough for reasonable exploration.

A model of reactivity based solely on bond counting (i. e., number of hydrogens bound to a site) could not reproduce the diversity of morphologies observed experimentally. For example, the production of long rows of unstrained dihydride species, recently observed in NH_4F (aq) etching of Si(100), could only be explained by the rapid etching of dihydrides that are adjacent to (strained) monohydrides — so-called "α-dihydrides."

Under some conditions, the etching surface spontaneously formed microfaceted pyramidal hillocks characterized by four Si{111} faces intersecting in four Si{110} edges and capped by a single unstrained dihydride. Similar (albeit significantly larger) pyramids have been observed experimentally on etched Si(100) faces. In contrast with previously postulated mechanisms, pyramid formation was *intrinsic* to the etch kinetics; no masking agent (*e.g.,* impurity, gas bubble) was required. Pyramid formation was explained in terms of the slow etch rate of the sides, edges and apex of the pyramid. As a result, slow etching of Si(111) surfaces was a necessary, but insufficient, criterion for microfacet formation on Si(100) surfaces. Interestingly, microfaceted surfaces displayed a higher density of Si(110)-like monohydrides than Si(111)-like monohydrides, in spite of the {111} faceting. This observation was explained in terms of the relatively high density of hydrides on the {110}-terminated edges.

5.6. Acknowledgments

This work was supported by the National Science Foundation (NSF) under Award CHE-0911405 and the Cornell Center for Nanoscale Systems under NSF Award EEC-0646547. B. S. A. gratefully acknowledges support from the NSF IGERT program (NSF Award DGE-0654193).

REFERENCES

[1] P. Krause, E. Obermeier, and W. Wehl, Sensor Actuat. A **53**, 405 (1996).

[2] T. Diepold, E. Obermeier, and A. Berchtold, J. Micromech. Microeng. **8**, 144 (1998).

[3] J. Knoch, J. Appenzeller, B. Lengeler, R. Martel, P. Solomon, P. Avouris, C. Dieker, Y. Lu, K. L. Wang, J. Scholvin, and J. A. del Alamo, J. Vac. Sci. Technol. A 19, 1737 (2001).

[4] M. A. Hines, Int. Reviews in Phys. Chem. **20**, 645 (2001).

[5] M. A. Hines, Annu. Rev. Phys. Chem. **54**, 29 (2003).

[6] M. F. Faggin, S. K. Green, I. T. Clark, K. T. Queeney, and M. A. Hines, J. Am. Chem. Soc. 128, 11455 (2006).

[7] I. T. Clark, B. S. Aldinger, A. Gupta, and M. A. Hines, J. Phys. Chem. C **114,** 423 (2010).

[8] J. Flidr, Y.-C. Huang, T. A. Newton, and M. A. Hines, J. Chem. Phys. **108**, 5542 (1998).

[9] B. S. Swartzentruber, and M. Schacht, Surf. Sci. **322**, 83 (1995).

[10] R. C. DeMattei and R. S. Feigelson, in *Electrochemistry of Semiconductors and Electronics*, edited by J. McHardy, and F. Ludwig (Noyes, Park Ridge, NJ, 1992), p. 1.

[11] G. J. Pietsch, G. S. Higashi, and Y. J. Chabal, Appl. Phys. Lett. **64**, 3115 (1994).

[12] Y. J. Chabal and K. Raghavachari, Phys. Rev. Lett. **53**, 282 (1984).

[13] Y. J. Chabal and K. Raghavachari, Phys. Rev. Lett. **54**, 1055 (1985).

[14] M. B. Webb, F. K. Men, B. S. Swartzentruber, R. Kariotis, and M. G. Lagally, Surf. Sci. **242**, 23 (1991).

[15] M. B. Webb, Surf. Sci. **299**, 454 (1994).

[16] S. P. Garcia, H. Bao, and M. A. Hines, Phys. Rev. Lett. **93**, 166102 (2004).

[17] M. A. Gosálvez, R. M. Nieminen, P. Kilpinen, E. Haimi, and V. Lindroos, Appl. Surf. Sci. **178**, 7 (2001).

[18] M. A. Gosálvez and R. M. Nieminen, New J. Phys. **5**, 100.1 (2003).

[19] M. A. Gosálvez, A. S. Foster, and R. M. Nieminen, Europhys. Lett. **60**, 467 (2002).

[20] S. Ciraci and I. P. Batra, Surf. Sci. **178**, 80 (1986).

[21] J. E. Northrup, Phys. Rev. B **44**, 1419 (1991).

[22] K. Endo, K. Arima, K. Hirose, T. Kataoka, and Y. Mori, J. Appl. Phys. **91 (7)**, 4065 (2002).

[23] U. Freking, P. Krüger, A. Mazur, and J. Pollmann, Phys. Rev. B **69**, 035315 (2004).

[24] The algorithm stores the locations and identities of all defects in a binary tree. This tree must be searched after every etch,[8] which accounts for the ln(N) term in the scaling.

[25] D. E. Temkin, in *Crystallization Processes*, edited by N. N. Sirota, F. K. Goorskii, and V. M. Varikash (Consultants Bureau, New York, 1966), p. 169.

[26] J. D. Weeks and G. H. Gilmer, Adv. Chem. Phys. **40**, 157 (1979).

[27] J. C. Russ, *The Image Processing Handbook*, 2nd ed. (Chemical Rubber, Boca Raton, FL, 1994), Chap. 3.

[28] *Monte Carlo Methods in Statistical Physics,* edited by K. Binder (Springer, Berlin, 1986).

[29] Y. J. Chabal, G. S. Higashi, K. Raghavachari, and V. A. Burrows, J. Vac. Sci. Technol. A **7**, 2104 (1989).

[30] Although subscripts are more commonly used, we introduce the nomenclature $k(x)$ for the etch rate of site x to avoid the use of superscripted subscripts in later sections.

[31] H. Camon, M. Djafari-Rouhani, D. Estéve, A. M. Gué, and Z. Moktadir, Microsyst. Technol. **1**, 163 (1995).

[32] H. Camon and Z. Moktadir, Sensor Actuat. A **46-47**, 27 (1995).

[33] H. Camon, Z. Moktadir, and M. Djafari-Rouhani, Mat. Sci. Eng. B **37**, 142 (1996).

[34] If an unstrained monohydride site had at least one neighboring monohydride, the site was classified as (110)-like. In contrast, if the nearest neighbors of an unstrained monohydride site were not hydrides, the site was classified as (111)-like.

[35] Although other statistical parametrizations of morphology can be defined, the densities of (111)- and (110)-like monohydrides are particularly easy to measure with infrared absorption spectroscopy due to the narrow linewidth of the Si–H stretch vibrational resonances of these species.

[36] J. H. Ye, K. Kaji, and K. Itaya, J. Electrochem. Soc. **143**, 4012 (1996).

[37] K. Arima, J. Katoh, and K. Endo, Appl. Phys. Lett. **85**, 6254 (2004).

[38] K. Arima, J. Katoh, S. Horie, K. Endo, T. Ono, S. Sugawa, H. Akahori, A. Teramoto, and T. Ohmi, J. Appl. Phys. **98**, 103525 (2005).

[39] Technically, silicon trihydride species are likely the most reactive sites, as they are not observed in morphological or spectroscopic investigations.

[40] The structure of the Si(111) kink site is shown in Fig. 4 of Ref. 5.

[41] J. M. Rodriguez, I. Tobias, and A. Luque, Sol. Energy Mater. **45**, 241 (1997).

[42] Z. Xi, D. Yang, and D. Que, Sol. Energy Mater. **77**, 255 (2003).

[43] P. Papet, O. Nichiporuk, A. Kaminski, Y. Rozier, J. Kraiem, J. F. Lelievre, A. Chaumartin, A. Fave, and M. Lemiti, Sol. Energy Mater. **90**, 2319 (2006).

[44] G. S. Higashi, Y. J. Chabal, G. W. Trucks, and K. Raghavachari, Appl. Phys. Lett. **56**, 656 (1990).

[45] P. Jakob, Y. J. Chabal, K. Kuhnke, and S. B. Christman, Surf. Sci. **302**, 49 (1994).

[46] S. Watanabe, Surf. Sci. **351**, 149 (1996).

[47] M. A. Gosálvez, K. Sato, A. S. Foster, R. M. Nieminen, and H. Tanaka, J. Micromech. Microeng. **17**, S1-S26 (2007).

[48] S. Tan, M. L. Reed, and R. Boudreau, Journal of Microelectromech. Sys. **5**, 66 (1996).

[49] H. Tanaka, Y. Abe, T. Toneyama, J. Ishikawa, O. Takenaka, and K. Inoue, Sensor Actuat. A **82**, 270 (2000).

[50] A. J. Nijdam, E. Van Veenendaal, H. M. Cuppen, J. Van Suchtelen, M. L. Reed, J. G. E. Gardeniers, W. J. P. Van Enckevort, E. Vlieg, and M. Elwenspoek, J. Appl. Phys. **89**, 4113 (2001).

[51] E. D. Palik, O. J. Glembocki, J. Heard, I., P. S. Burno, and L. Tenerz, J. Appl. Phys. **70**, 3291 (1991).

[52] S. A. Campbell, K. Cooper, L. Dixon, R. Earwaker, S. N. Port, and D. J. Schiffrin, J. Micromech. Microeng. **5**, 209 (1995).

[53] T. Baum, J. Satherly, and D. J. Schiffrin, Langmuir **14**, 2925 (1998).

[54] H. Schröder, E. Obermeier, and A. Steckenborn, J. Micromech. Microeng. **9**, 139 (1999).

[55] For a review, see M. Wortis, in *Chemistry and Physics of Solid Surfaces,* vol. 7, edited by R. Vanselow and R. F. Howe (Springer, Berlin, 1988), p. 367.

[56] G. Wulff, Z. Kristallogr. Mineral. **34**, 449 (1901).

[57] C. Herring, Phys. Rev. **82**, 87 (1951).

[58] B. W. Batterman, Appl. Phys. Lett. **28**, 1236 (1957).

[59] R. J. Jaccodine, J. Appl. Phys. **33**, 2643 (1962).

[60] V. Le Thanh, D. Bouchier, and G. Hincelin, J. Appl. Phys. **87**, 3700 (2000).

Chapter 6

Simulating the Vibrational Spectrum of H/Si Surfaces With Density Functional Theory

6.1. Introduction

The infrared spectrum of H-terminated Si surfaces has received a tremendous amount of attention in the past three decades.[1] In an experimental and theoretical *tour de force*,[2-11] the highly polarized and well-resolved vibrational resonances observed on flat and vicinal H/Si(111) and H/Si(110) surfaces enabled the extraction of an unprecedented level of structural and dynamical information from these surfaces, including insights into defect structures, phonon coupling, and terrace width distributions. The vibrational spectrum of the industrially important H/Si(100) surface, which displays broad, weakly polarized resonances, has proven to be much more complicated. In the late 80's, researchers at Bell Labs used molecular clusters to model the infrared spectrum of etched H/Si(100) surfaces.[2] On the basis of these models, they inferred that the surfaces were atomically rough and covered with mono-, di-, and trihydride species. This spectral interpretation served as the basis for many subsequent analyses.

In a surprising turn of events, the data reported in Chapter 3 conclusively overturned the Bell Labs analysis and lead to a very different understanding of the H/Si(100) surface and its infrared spectrum. These findings did not necessarily imply that the Bell Labs spectral simulations were wrong, just that the wrong species were modeled. One of the difficulties in obtaining a full understanding of the H/Si(100) surface has been interadsorbate strain. As shown later, point defects alter the long-range strain fields on surface and lead to significant structural changes and complex spectra. This chapter therefore addresses an unresolved question: Can modern computational

methods simulate the vibrational spectrum of a highly strained H/Si surface with sufficient accuracy to enable definitive vibrational mode assignments?

The theoretical methods that have been developed for vibrational energy calculations are broadly of three types: phenomenological methods, first-principles methods, and semi-empirical methods.[12] Phenomenological methods require structural parameters, such as bond lengths, and additional fitting parameters derived from experiments or other theoretical data. For example, phenomenological methods based upon force-constant[13] and bond charge[14] models have been used to calculate the surface phonons and dispersion curves of flat H/Si(111) from the data on the bulk Si phonon spectra and electron energy loss spectra, respectively. The semi-empirical methods are fundamentally phenomenological in nature, but use first-principle methods with certain fitting parameters to determine the structure and vibrational properties of the system. This approach can reduce the computational demands of a fully first-principles approach but does not fully incorporate electronic effects in the phonon calculations. In cases such as the H/Si(100) surface, where the bonding geometry of surface atoms is not known and the electronic effects of strain on vibrational dynamics are not well understood, first-principles methods must be used to adequately simulate the surface structure and its spectra.

First-principles methods can be broadly classified into two categories: those based upon the Hartree-Fock[15] approach and those based upon density functional theory (DFT). Hartree-Fock-based methods, which are based on atomic orbitals, were developed for molecules, whereas DFT was developed for solids and periodic systems. In recent years, both approaches have been applied to solids and molecular systems. The choice of method is determined by the system, the properties to be studied, and the computational expense, which in turn depends upon the level of approximation, the size of the basis set, and the model being used.

Two types of systems have been used in simulations of surfaces: molecular clusters and periodic slabs.[16,17] Clusters are designed to simulate the local chemical environment of the surface and have the advantage of being simple and computationally inexpensive. The cluster approach assumes that the electronic states of a bulk solid can be well described by localized chemical bonds — an assumption that can be applied reasonably well to semiconductors. This approach, however, cannot simulate long-range surface effects, such as strain fields, realistically with a small number of atoms. In slab models, the surface is simulated by an infinitely repeating "supercell" that consists of a finite number of substrate layers typically capped with an adsorbate layer on both sides and a finite-thickness vacuum layer. Periodic boundary conditions are applied to the supercell in three dimensions, making the surface infinite and continuous in two dimensions. An infinite array of parallel slabs are separated by layers of vacuum in the third dimension. The advantage of slabs is that they can be used to model the local chemical environment as well as long-range effects on surfaces. Slab models, however, can be computationally more expensive. Also, inter-slab interactions in these models are a potential source of errors.

For H/Si surfaces, the first quantum-mechanical vibrational energy calculations were reported by Chabal *et al.* from Bell Labs in 1984.[18,19] They used small clusters to simulate the 2 × 1 and 3 × 1 reconstructed H/Si(100) surfaces with Hartree-Fock-based methods. Using the same approach, they later modeled H/Si(111) and H/Si(100) surface sites[2,3] and calculated the equilibrium geometry and vibrational modes for these sites. Their calculations predicted the vibrational mode splittings of unstrained sites accurately to within 3 cm^{-1} (experimental splittings ~10 cm^{-1}) and of strained dihydride on vicinal H/Si(111) surfaces to within ~10 cm^{-1} (experimental splittings ~40 cm^{-1}); however, the energies of these modes were not very accurate.

The first slab calculations of a H/Si surface was reported by Kaxiras *et al.*[7] who modeled H/Si(111) surface with a six-layer-thick slab and simulated its surface phonon spectrum with a fully-self-consistent calculation using DFT. Their calculations predicted mode energies for the Si-H stretch vibrations ~ 5% (100 cm^{-1}) lower than experiments. This surface was later simulated within the frozen-phonon approximation using DFT with anharmonic corrections by Li *et al.*[8] and Honke *et al*.,[20] which yielded Si-H stretch mode energies ~6% lower and ~1% higher, respectively, than experiments. Li *et al*. also modeled dihydride steps on vicinal H/Si(111) surface[9] using the same methodology and reproduced the mode splittings observed in experiments. (Absolute mode energies were not reported.) Using a semi-empirical approach, Sandford *et al.*[10] calculated the phonon spectrum of H/Si(111) surface using a 14-layer slab and obtained the Si-H stretch mode energy to within 1% (20 cm^{-1}) of the experimental values. With the same technique, Gräschus *et al.*[11] obtained absolute mode energies for H/Si(110) surface also to same accuracy, but their calculations could not accurately predict the Si-H stretch mode splittings — the calculations predicted a splitting of <1 cm^{-1} whereas the experimental mode splitting is ~19 cm^{-1}.

The bulk-terminated H/Si(100) surface, an entirely dihydride terminated surface, has been studied with slab models by many researchers using first-principles DFT methods[21-25] as well as empirical tight-binding methods.[26,27] The first-principles methods consistently predict a canting of the dihydrides to relieve surface strain. The mode energies predicted by these calculations, however, have significant discrepancies. Two separate tight-binding calculations by Tagami *et al*.[26,27] predicted the stretch of the lower Si-H of the dihydride (the "down" mode) to be lower in energy than the stretch mode of the upper Si-H (the "up" mode), with splitting values of 0 and 194 cm^{-1}, respectively. DFT calculations by the same authors[24] predicted this mode splitting to be 48 cm^{-1}. DFT calculations by other researchers[25,28] predicted the reverse mode ordering,

with splittings ranging from 65 cm^{-1} to 121 cm^{-1}. The bulk-terminated surface has not been observed experimentally, and therefore the accuracy of these calculations cannot be evaluated.

Since the actual structures of etched H/Si(100) surfaces were only recently uncovered,[29,30] few simulations of these structures exist. Endo *et al.*[23] calculated the energy of two possible missing-row structures on H/Si(100) surface (they did not incorporate canting of the dihydrides) and predicted the structure terminated by alternating rows of strained and unstrained dihydrides (similar to the NH_4F-etched surface) as thermodynamically more stable among the two structures. No studies of the vibrational spectrum of etched H/Si(100) surfaces have been reported.

This chapter presents the results of a comprehensive study of the vibrational mode and energies of a wide variety of H-terminated Si surfaces, including H/Si(111), H/Si(110) and H/Si(100) surfaces. The models were designed to simulate experimentally observed morphologies produced by NH_4F etching. As such, surface reconstruction was not allowed. All calculations were performed with DFT-based methods and slab geometries. Where appropriate, the calculated vibrational energies were compared to experimental spectra to judge the accuracy of the models.

The first step in this study was optimizing the simulation parameters. The pseudopotentials and exchange correlation functionals (*vide infra*) were chosen based on their accuracy in calculating the vibrational energies of H/Si(111) and gas phase silane. The minimum acceptable slab size and spacing were ascertained from simulations of H/Si(111). These results guided the choice of parameters for subsequent calculations.

In addition to improved accuracy over previous works, these simulations led to a number of new insights. The simulations predicted the spectral bands observed due to defect modes observed on vicinal H/Si(111) surfaces with reasonable accuracy,

including the energy shifts in the vibrational modes of terrace vibrations with changes in the terrace size. Simulations of the missing-row morphology observed on the NH_4F-etched H/Si(100) confirmed recent assignments and clarified the role of point defects on band broadening.

6.2. Computational

This section first gives a brief overview of the DFT formalism and relevant approximations used in the electronic structure simulations. The computational methods used for modeling the surfaces, optimizing their structures, and simulating their vibrational modes are then presented.

6.2.1. Theoretical Formalism

The density functional theory, as formulated by Kohn and Sham,[31] describes a system in terms of its ground state electron density, which, in principle, uniquely determines the ground state wavefunction and properties. The ground state electron density of a system can be obtained as the self-consistent solution of the Kohn-Sham equations;[31] however, the solution of this equation poses a practical challenge: the general form of the exchange correlation functional of the electron density (which is required to solve the equation) is not known except for special cases like the homogeneous electron gas. The simplest approximation that can be used to find the density functional of a system is the local density approximation (LDA), which uses the exchange correlation functional of the homogeneous electron gas. The next level of approximation is known as the generalized gradient approximation (GGA), which includes both the local electron density as well as its gradient. Although this approximation includes more information, there is no systematic evidence showing that GGA always gives more accurate results than LDA.[32] Therefore, the performance of different density functionals must be tested for every system and property of interest.

Since most chemical and physical properties depend upon the valence electrons, considerable computational savings can be realized by replacing the (nearly invariant) core electrons with an effective potential. This idea is incorporated into DFT using the pseudopotential method.[33] In this approach, the core electrons are replaced with an angular-momentum dependent potential that accounts for the nuclear potential and the effect of "frozen" core electrons on the valence electrons. The pseudopotentials are constructed using a cut-off radius such that outside the cut-off radius, the wavefunctions of the valence electrons in the pseudopotential match the all-electron wavefunction. Inside the cut-off radius, the pseudo-wavefunctions differ from the all-electron wavefunctions. The pseudo-wavefunctions are nodeless and therefore amenable to simulations by a relatively small number of basis functions (*e.g.,* plane-waves). Pseudopotentials with small cut-off radii more accurately simulate bonding effects in diverse chemical environments than those with larger cut-off radii — a property known as the transferability of the pseudopotentials. Not surprisingly, pseudopotentials with small cut-off radii, known as "hard" pseudopotentials, require larger basis sets than "soft" versions. Blöchl[34] and later Kresse *et al.*[35] developed a generalization of the pseudopotential approach, known as the projector augmented wave (PAW) formulation, which typically has increased transferability over "traditional" pseudopotentials with similar cut-off radii. The PAW potentials, however, allow a variable cut-off radius, which is often used to optimize the accuracy of calculations for available computational resources.

The representation of (spatially) extended electronic states in a periodic system such as the slab geometry is practically implemented by using the Bloch theorem.[36] This theorem states that the electronic eigenstates of a periodic system, ψ_i, can be expressed in terms of a cell-periodic component, φ_i, and a plane-wave component according to

$$\psi_i = \varphi_i e^{i\mathbf{k}\cdot\mathbf{r}}.$$

The cell-periodic components can be expanded in terms of a discrete plane-wave basis set (used in this study, *vide infra*), which can be truncated at some minimum wavelength that is typically expressed as an (maximum) *energy cut-off* corresponding to the highest kinetic energy of the plane waves. The Kohn-Sham potential and the total energy are obtained using an integral over the Brillouin zone that is performed using special sets of *k*-points in the Brillouin zone. The optimum energy cut-off and set of *k*-points balance computational accuracy against computational resources.

6.2.2. Computational Methods

All calculations used the Vienna *ab-initio* simulation package[37-40] (VASP, version 5.2) running on an Opteron Blade Cluster, consisting of IBM LS21 blade servers with two dual-core 2.6 GHz Opteron processors located at the Rensselaer Polytechnic Institute. The exchange correlation functionals corresponding to both LDA, as developed by Ceperly and Alder[41] and parameterized by Perdew and Zunger,[42] and GGA, as developed by Perdew, Burke and Ernzerhof (PBE),[43] were tested for their performance on the H/Si(111) surface and the silane molecule to chose the functional for the subsequent calculations. For GGA functionals, both the PBE functional[43] and its variation PBEsol,[44] which is designed to yield more accurate results for systems with wide ranging density gradients, were tested.

Projector Augumented Wave (PAW) pseudopotentials with a plane-wave basis set, as developed by Kresse and Joubert,[35] were used for all calculations. Both normal and hard-core versions of the PAW pseudopotentials, corresponding to different cut-off radii, were tested for performance. The reciprocal-space projector scheme of the PAW pseudopotentials was used for all structures, except for the large 4 × 2 supercells (*vide infra*) of the H/Si(100) surface, where the real-space projector scheme[45] was used for computational efficiency. The kinetic energy cut-offs used for the plane-wave basis set

were based on the convergence results for the cell energy and vibrational energies of bulk silicon.

6.2.2.1. The Supercells and *k*-Point Meshes

The slab models are typified by Fig. 6.1, the slab used to represent the H/Si(111) surface. The principal surface axis [*e.g.,* (100) or (111)] was aligned with the *z*-axis, and the surface model was constructed on the upper surface. A few of the bottom-most Si layers (*vide infra*) were frozen to their bulk lattice positions, which were obtained from the bulk Si simulations performed with the same pseudopotentials and exchange correlation functional. Dangling bonds on the lower surface were terminated with H atoms. Periodic boundary conditions were applied in all three dimensions, making the

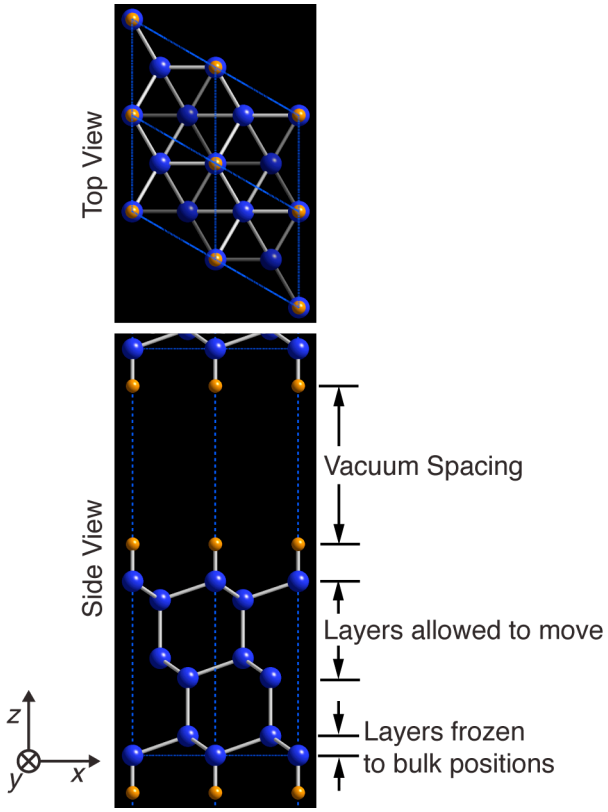

Figure 6.1. Slab model of a flat Si(111) surface. The Si atoms are shown in blue, the H atoms are shown in orange, and the supercell edges are shown by the blue dashed lines. This convention is used for all figures in this chapter. The Cartesian axes are defined with respect to the side view.

slab infinite in two dimensions. The total number of Si layers, the number of layer frozen, and the vacuum spacing were optimized using the H/Si(111) slab. The lower H atoms were allowed to move during structural optimization, but were frozen during the vibrational energy calculations for computational efficiency. With optimized parameters, freezing of the lower H atoms during structural optimizations and vibrational mode calculations resulted in negligible shifts in vibrational energies (≤ 2 cm^{-1}) compared to the calculation with these H atoms unfrozen.

Simulations of gas phase silane used one molecule in the center of a cubic unit cell with 15 Å sides.

The Monkhorst-Pack (MP) scheme[46] was used to generate all *k*-point meshes. A gamma-centered grid was used for the Si(111) calculations, since low-symmetry systems (such as hexagonal) are not appropriately represented by the original MP scheme. The requisite number of *k*-points depended on the size and symmetry of the supercell. Sometimes, structual relaxation or atomic displacements during vibrational dynamics simulation lowered the supercell symmetry, thereby increasing the required number of *k*-points. Therefore, the *k*-points were chosen after investigating the convergence of relaxed structure energy as well as the vibrational energies with respect to the *k*-points.

6.2.2.2. Structural Optimization and Vibrational Analysis

Each simulation had three stages. First, the total energy of the system was minimized to obtain the equilibrium structure. Second, the vibrational modes and their energies were calculated from the equilibrium structures. Third, the transition dipole moment of each normal mode was estimated from the displacement vectors.

For the structural relaxation and the vibrational dynamics calculations, the total cell energies were calculated using two methods, depending on the number of *k*-points. For small supercells that had more than one *k*-point in at least two of the three

dimensions, the total energy calculations used the tetrahedron method with Blöchl correction,[47] as recommended for semiconductor and insulators by the VASP developers. For silane and other large supercells, where the number of *k*-points was one in two or three dimensions, the tetrahedron method could not be used due to the insufficiency of *k*-points. For those structures, the Gaussian smearing technique of Methfessel and Paxton[48] was employed with a smearing width of $\sigma = 0.1$. The two methods yielded nearly-identical vibrational energies, as evidenced by calculations on one of the vicinal H/Si(111) surface reported in Appendix C.

The structure relaxations were performed using the conjugate gradient method.[49] All structures were relaxed until forces on the (non-frozen) atoms were $\lesssim 10^{-3}$ eV/Å, and the total energy change between successive optimization steps was $<10^{-5}$ eV. The cell volume was allowed to change during relaxation of the bulk Si structure, but not during relaxation of the slab structures.

Vibrational mode energies were calculated using density functional perturbation theory (DPFT) as developed by Baroni *et al*.[50] The mode energies were obtained in the harmonic approximation by diagonalization of the Hessian matrix (*i.e.,* the second-order derivative tensor with respect to nuclear coordinates) of the Born-Oppenheimer energy. This calculation is included in VASP 5.2. Calculated mode energies are reported without any correction factors. Only the infrared-active modes, defined as the modes with non-zero transition dipole moments (*vide infra*), are reported.

Transition dipole moments for the vibrational modes were estimated under the assumption that every Si-H unit has the same (static) dipole moment. In this approximation, the transition dipole of a vibrational mode is proportional to the vector sum of the Si-H bond displacements. The atomic displacement vectors for each normal mode vibration were normalized to the root-sum-square of the atomic displacement vectors. The relative intensities of the normal modes were assumed to be proportional to

the square of the transition dipoles. No attempt was made to calculate the amplitude of motion for each mode. As a result, the relative intensities of modes with very different energies (*e.g.,* stretch and bend modes) may not be directly comparable.

Appendix D discusses an alternate approach for calculating the transition dipole moments using the Born effective charges, similar to the method used by Lee *et al.*[51] The convergence of Born effective charges, however, required many more *k*-points and a much larger vacuum spacing than what was realistically possible with current resources. The results of the convergence studies and future perspectives for this approach are included in the Appendix.

6.3. Results

The first part of this section describes the protocols that were used to optimize and verify the many simulation parameters, including the choice of exchange-correlation functional, pseudopotential, and slab parameters. The second part presents the results of simulation of the principal H-terminated faces of silicon: H/Si(111), H/Si(110), and H/Si(100).

6.3.1. Optimization of Computational Parameters

Although the accuracy of observables (such as supercell energy) in simulations, in general, increases with higher orders of approximations (*e.g.,* larger energy cut-off or *k*-points), the dependence of observables on the computational parameters must be studied before choosing the values of these parameters for two reasons. First, the convergence of observables with the increasing level of approximation need not be monotonic. This can be important in some cases (*vide infra*), where the "converged" observable, which would be obtained from exact calculations, are not available to know the accuracy of calculations at given values of the parameters. In these situations, the converged observables were *estimated* from simulations performed with relatively high level of approximations. Secondly, different system properties have different

dependence on the computational parameters, and therefore a single default set of parameters cannot be used for all calculations. For example, the vibrational energy depends on the change in energy with respect to atomic displacements. Therefore, accurate calculations of vibrational energy typically require higher level of approximation (*e.g.,* energy cut-off) than the supercell energy calculations. Therefore, convergence of the vibrational energies, the observable of interest, was used as the criterion for parameter optimizations.

To insure accuracy while keeping computational requirements reasonable, various electronic structure parameters and slab parameters were optimized using bulk Si, H/Si(111) and gas phase sliane as test systems. The electronic structure parameter included the energy cut-off, the *k*-points, the exchange correlation functionals, and the pseudopotentials, and the slab parameters included the slab size and inter-slab spacing. The optimization tests on bulk Si and the H/Si(111) surface were performed with PBE functionals and normal PAW pseudopotentials as these simulations required smaller energy cut-off than the hard versions.

6.3.1.1. Energy Cut-off and *k*-points

The dependence of total cell and vibrational energies on the energy cut-off and *k*-point mesh was assessed on bulk Si, as this system could be simulated with relatively large values of these parameters. Trends observed from this system guided the optimization of these parameters for the slab structures.

The total cell energy of the smallest unit cell of bulk Si with 2 atoms per unit cell was calculated as a function of energy cut-off and the *k*-points mesh, as shown in Fig. 6.2. The cell energy decreased monotonically with both *k*-points and energy cut-off and appeared to converged asymptotically. The total energy per atom reached 0.01 eV of the minimum calculated energy at an energy cut-off of 250 eV. Similarly, a *k*-point mesh of 6 × 6 × 6 led to energy within 0.02 eV of the observed minimum.

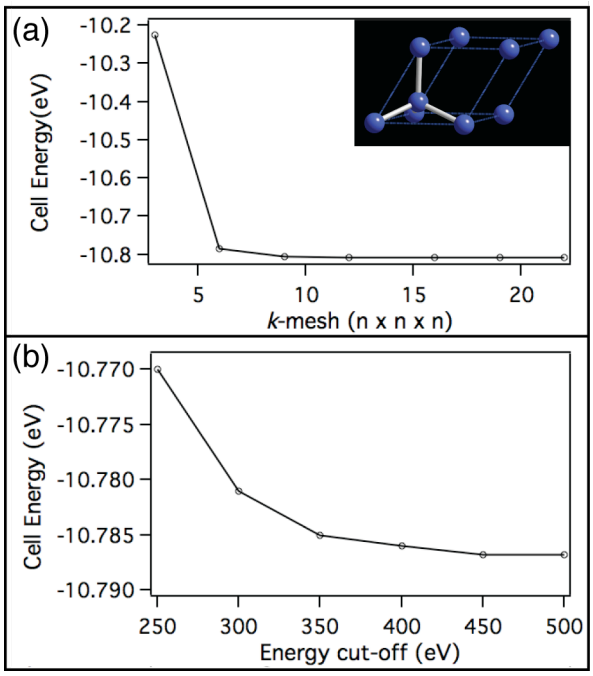

Figure. 6.2. Variation of the total cell energy for a 2-atom bulk Si unit cell (inset) after structural optimization. The energy cut-off in (a) was 350 eV, and the *k*-point mesh in (b) was 6 × 6 × 6.

The bulk phonon spectrum of Si was calculated as a function of energy cut-off and *k*-point mesh using the 8-atom unit cell shown in Fig. 6.3 (inset). For this unit cell, 21 vibrational modes were observed. The energies of the lowest and highest modes are plotted in Fig. 6.3. The energies did not converge monotonically with increasing sophistication; however, the energy variations decreased to less than 1 cm^{-1} for simulations with a *k*-point mesh and energy cut-off greater than or equal to 6 × 6 × 6 and 400 eV, respectively.

These results showed that the vibrational mode energies varied differently than the total cell energy with respect to the energy cut-off and the *k*-point density, but reasonable convergence of the mode energies (~1 cm^{-1}) was obtained with energy cut-off close to the recommended value of 245 eV for Si atoms with normal PAW pseudopotential and a reasonable *k*- point mesh.

The energy cut-off and *k*-point meshes for the H/Si surface slabs were also optimized to obtain Si-H vibrational energies within ~1 cm^{-1} of the calculated minima.

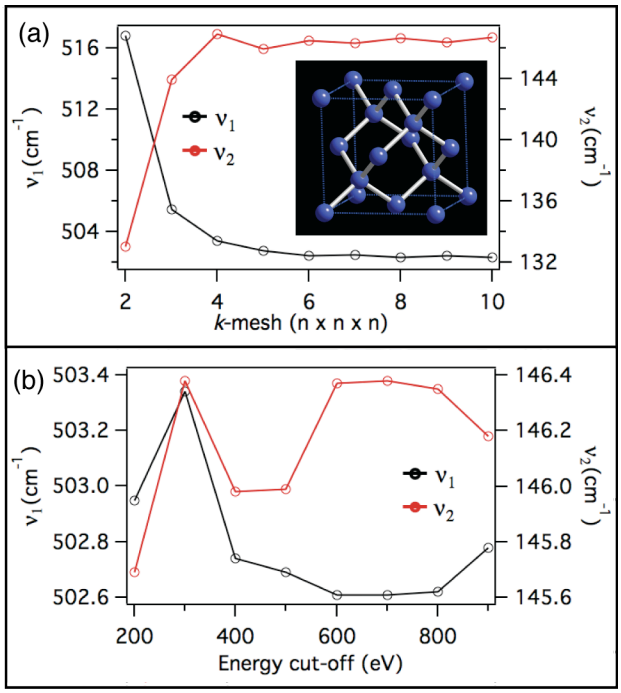

Figure 6.3. Variation of the highest ν_1 and lowest ν_2 phonon energies, of bulk silicon (inset) as a function of *k*-point mesh and energy cut-off. The bulk silicon lattice was relaxed with an energy cut-off of 800 eV and *k*-point mesh of 5 × 5 × 5. For phonon calculations, the energy cut-off in (a) was 400 eV, and the *k*-point mesh for (b) was 5 × 5 × 5.

For the supercells used for the slabs, this level of convergence was similarly obtained with energy cut-offs close to the recommended values (250 eV and 700 eV for systems with H + Si atoms using the normal and hard PAW pseudopotentials, respectively). The *k*-points mesh requirements showed significant dependence on the supercell size and symmetries. In general, the requisite *k*-points decreased with increasing in supercell dimensions. The optimizations of energy cut-off and *k*-points performed for various slab structures are included in Appendix C. The energy cut-offs and *k*-point meshes used in each calculation are noted in figure and table captions.

6.3.1.2 Slab Parameters

For slabs, the important parameters were the number of frozen and movable layers in the slab and the vacuum spacing. The slabs needed to have enough bulk Si layers to effectively simulate the electronic environment of the surface. The atoms near

the surface of the slab had to be free to move from their bulk positions for accurate modeling of surface relaxations and coupling between surface and bulk phonons. In addition, the vacuum spacing controlled the through-space interaction of the top and the bottom surfaces, which had to be minimized.

The optimization tests for these slab parameters were performed using the H/Si(111) slab shown in Fig. 6.1. Since these tests were performed using the PBE functional and regular PAW potentials, the bottom Si layers of the slab were frozen to the bulk Si lattice constant value of 5.473 Å obtained with the same functional and pseudopotentials (*vide infra*).

In comparing energies of supercells with different number of atoms, comparisons of energy per atom are more appropriate than those of total cell energy. The situation is complicated by varying densities of dissimilar atoms (here, Si and H atoms). In spite of this complication, the energy per atom is used as an approximate indicator of performance and is defined as the cell energy divided by the total number of Si and H atoms.

Table 6.1. Si-H stretch and bend mode energies for H/Si(111) slabs, typified in Fig. 6.1, of varying thickness. The calculations had a vacuum spacing of 7 Å and a *k*-point mesh of 5 × 5 × 2. Energy cut-off for the structural relaxation was 800 eV and for the vibrational energy calculation was 700 eV.

Total Si Layers	Unfrozen Si Layers	Si-H stretch (cm^{-1})	Si-H bend (cm^{-1})
4	2	2111.39	615.37
6	4	2107.65	615.20
6	2	2107.80	613.59
8	4	2107.45	614.47

The variation of the Si-H stretch and bend energies for the H/Si(111) surface with the varying numbers of frozen and unfrozen Si layers is shown in Table 6.1. These data showed that simulations with four unfrozen and two frozen Si layers resulted in vibrational energy convergence to within 1 cm^{-1}.

Interestingly, the Si-H stretch and bending modes were sensitive to different parameters. The stretch mode energy was primarily sensitive to the total number of layers, whereas the bend mode energy was primarily sensitive to the number of unfrozen layers. This observation suggests that the bend mode couples significantly to the bulk phonons (~514 cm^{-1}), whereas the stretch mode does not — a trend in keeping with the relative energies of these modes.

On the basis of these results, a total of six bulk layers, with two bottom layers frozen to bulk positions, were taken as the optimum thickness of slab structures. This result was also confirmed on calculations of a highly strained surface obtained by miscutting a H/Si(111) surface by 19.4° towards the $\langle \bar{1}\bar{1}2 \rangle$ direction. The results of this calculation are included in Appendix C.

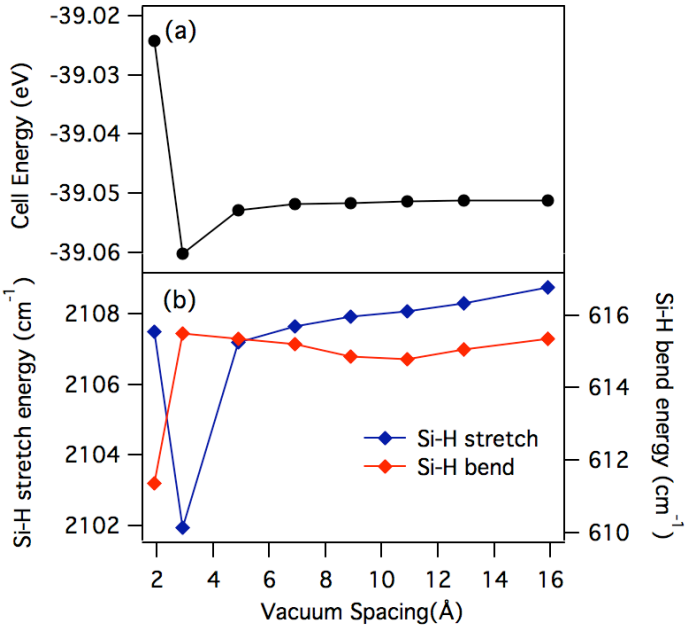

Figure 6.4. The dependence of the supercell and the Si-H stretch and bend mode energies of the H/Si(111) surface slab shown in Fig. 6.1 on the vacuum spacing.

The effect of vacuum spacing on the total cell and the Si-H vibrational energies for the H/Si(111) surface is shown in Fig. 6.4. For vacuum spacing ≥ 7 Å, the variation in cell energy was less than 0.001 eV (~0.1 meV per atom), and the variation in the

vibrational energies was ~1 cm^{-1}. Therefore, a vacuum spacing of 7 Å was used for all subsequent calculations. For vicinal H/Si(111) surfaces with a miscut angle α, the slab spacing along the ⟨111⟩ direction was increased by a factor of $1/\cos(\alpha)$ to maintain the requisite vacuum spacing.

6.3.1.3. Choice of Exchange-Correlation Functional and Pseudopotential

The performance of different exchange-correlation functionals and pseudopotentials was assessed from the simulated Si-H vibrational energies of a H/Si(111) slab and a gas-phase silane molecule.

For the slab calculations, the bulk Si lattice constant was first calculated with each of the functionals and the normal and hard PAW pseudopotentials; the calculated values are listed in Table 6.2. The pseudopotentials yielded lattice constant values that were within 0.01 Å (~0.1%) of those calculated by Hennig *et al.*[52] using an all-electron potential with the three functionals (LDA = 5.403 Å, PBE = 5.472 Å, and PBEsol = 5.434 Å).

Table 6.2. The bulk Si lattice constants calculated with different functionals and regular and hard PAW pseudopotentials.

LDA (Å)		PBE (Å)		PBEsol (Å)	Experimental[53] (Å)
Regular	Hard	Regular	Hard	Regular	
5.407	5.407	5.473	5.468	5.440	5.431

Table 6.3. Si-H vibrational energies of H/Si(111) surface in Fig. 6.1 computed using LDA, PBE and PBEsol functionals with regular and hard versions of PAW pseudopotentials. Experimental mode energies (stretch and bend mode energies at T = 130 K and T = 293 K, respectively) are included for comparison. The energy cut-off for the structure relaxation was 800 eV, and for vibrational energy calculation was 700 eV. A k-point mesh of 5 × 5 × 2 was used for all calculations.

Mode	LDA (cm^{-1})		PBE (cm^{-1})		PBEsol (cm^{-1})	Experimental (cm^{-1})
	Regular	Hard	Regular	Hard	Regular	
Si-H stretch	2096.8	2101.7	2107.6	2109.4	2100.1	2085.5[54]
Si-H bend	598.1	596.6	615.3	612.1	600.2	626.7[55]

Table 6.3 compares the calculated Si-H vibrational energies of a H/Si(111) surface with the experimentally observed values. The hard and soft versions of the PAW pseudopotentials (with a given functional) yielded vibrational energies with differences of < 5 cm^{-1}, which was insufficient to merit the choice of one versus the other. Among the functionals, LDA and PBEsol predicted the Si-H stretch energy with slightly better accuracy than the PBE, but grossly underestimated the bending mode energies.

Table 6.4 presents a similar comparison of calculated and experimental vibrational energies for a gas-phase silane molecule. Two trends were evident in this data. First, the PBEsol functional significantly underestimated the energies of stretch vibrations. Second, simulations that used the PBE functional generated the most accurate energies for scissor modes.

Table 6.4. Vibrational energies of silane molecule placed at the center of a 15 Å × 15 Å × 15 Å box with periodic boundary conditions. The calculations used a *k*-mesh of 1 × 1 × 1, and energy cut-off of 700 eV.

Mode	LDA (cm^{-1})		PBE (cm^{-1})		PBEsol (cm^{-1})	Experimental[56] (cm^{-1})
	Regular	Hard	Regular	Hard	Regular	
ν_1 (sym stretch)	2176.9	2183.7	2177.6	2176.3	2168.4	2185.7
ν_2 (sym scissor)	933.4	931.9	946.7	950.8	932.1	972.1
ν_3 (asym stretch)	2190.8	2198.3	2191.8	2190.6	2181.5	2189.1
ν_4 (asym scissor)	854.6	850.0	877.6	877.4	876.2	913.3

Based on these tests, the PBE functional was chosen for all subsequent calculations. The choice of pseudopotential was less obvious, as no systematic trend in accuracy of the two pseudopotentials was observed. For rest of the calculations, the hard PAW pseudopotential was chosen due to its better transferability (*vide supra*) than the normal one.

6.3.1.4. Effect of Supercell Size

The numerical accuracy and effects of supercell size were assessed from simulations of the Si-H vibrational energies on the H/Si(111) slab illustrated in Fig. 6.1. The results are given in Table 6.5. The cell energy per 1 × 1 unit of the slab were constant to within 5 meV with changes in supercell size. The supercell size had little effect (< 0.1 cm^{-1}) on the Si-H stretching mode, but the smallest supercell resulted in an anomalously low (~ 3 cm^{-1}) bend mode energy. The origin of this discrepancy is unclear.

Table 6.5. The supercell and the Si-H vibrational energies for different supercells of the H/Si(111) slab shown in Fig. 6.1. The calculations had a vacuum spacing of 7 Å, energy cut-off of 800 eV.

Supercell (*k*-points)	Cell Energy (eV)	Si-H stretch (cm^{-1})	Si-H bend (cm^{-1})
1 × 1 (6 × 6 × 2)	-39.228	2109.38	611.67
1 × 2 (6 × 3 × 2)	-78.456	2109.39	614.84
2 × 2 (3 × 3 × 2)	-156.925	2109.43	614.79

6.3.2. The Principle H-terminated faces of Si

6.3.2.1. H/Si(111) surfaces

In addition to the flat H/Si(111) surface discussed in previous sections, two principal vicinal H/Si(111) surfaces, with miscuts towards the $\langle \bar{1}\bar{1}2 \rangle$ and $\langle 11\bar{2} \rangle$ directions, have been extensively studied experimentally. The steps on these two miscut surfaces are terminated with strained dihydride and monohydride species, respectively. As such these vicinal surfaces are often used as well-defined models for surface roughness. The structure and vibrational modes of both miscuts were modeled computationally.

1) Miscut towards the $\langle 11\bar{2} \rangle$ direction

The Si-H vibrational modes of H/Si(111) surfaces miscut towards the $\langle 11\bar{2} \rangle$ direction were studied on two slabs with different terrace widths. The first slab had two terrace atoms (corresponding to a 15.8° miscut), whereas the second had four (10.0°

Figure 6.5. (a, b) Slab structures for simulation of H/Si(111) surfaces miscut towards the $\langle 11\bar{2} \rangle$ direction. (c) Calculated vibrational modes and experimental energies (at T = 90 K and room temperature for the stretch and bend modes, respectively). The transition dipole orientation is measured with respect to the $\langle 111 \rangle$ direction, shown by dashed line, and is given for the 10.0° miscut surface. The relative intensities are indicated in parentheses. Both structures were relaxed with a k-point mesh of 2 × 4 × 1 and energy cut-off of 800 eV. The vibrational mode energies for the 15.8° and 10.0° miscut slabs were calculated with 2 × 4 × 1 and 1 × 4 × 1 k-point meshes, and 750 eV and 700 eV energy cut-offs, respectively.

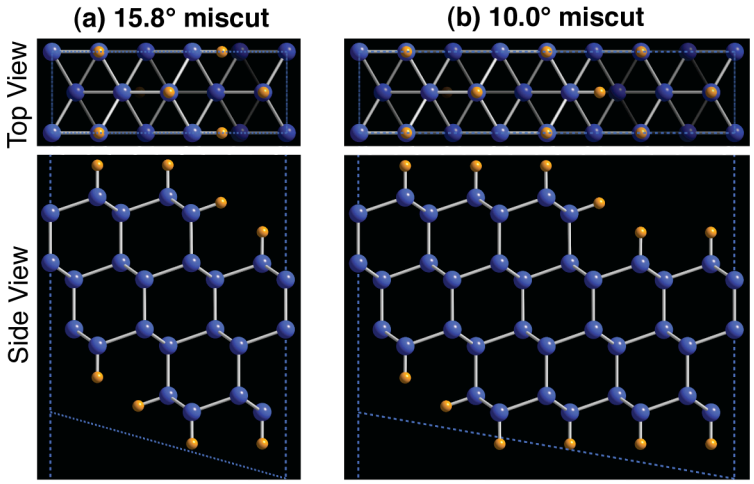

(c) Vibrational Mode Energies

Band	Mode	Transition Dipole Orientation	Energy (cm^{-1}) and (Rel. Intensity)		Experimental - 9.0° miscut (cm^{-1})	% Error
			15.8° miscut	10.0° miscut		
B_2	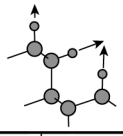		2114.7 (3.3)	2113.3 (3.9)	2089.1[6]	1.2
B_1	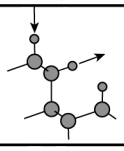		2100.0 (0.6)	2101.9 (0.9)	2072.7[6]	1.4
B_3	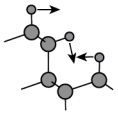		640.9 (0.6)	641.4 (0.6)	-	-
B_4	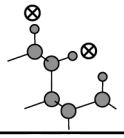	⊗	601.4 (4.1)	595.2 (3.2)	614[55]	3.1
B_5	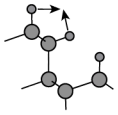		600.0 (1.0)	600.3 (1.0)	-	-
A_1			-	2107.2 (2.8)	2085.6[6]	1.0
A_3	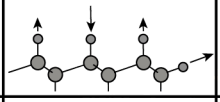	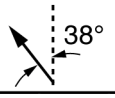	2105.2 (1.5)	2101.6 (0.4)	-	-
A_2			611.8, 617.9 (0.9, 3.2)	609.1, 615.6 (4.0, 5.4)	625.3, 628.7[55]	2.6, 2.1

miscut). The optimized structures for the two slabs and their infrared-active Si-H vibrational modes are presented in Fig. 6.5. The energy minimized structures were nearly identical to the bulk-terminated structure. The absence of significant substrate relaxation was consistent with the unstrained nature of the step termination and the comparable electronegativities of silicon and hydrogen. [The labels for the principal stretch modes (A_1, B_1, and B_2) follow the convention of Ref. 6, whereas the principal bend modes (A_2, B_3, and B_4) follow Ref. 5.]

Five infrared-active step modes, labeled $B_1 - B_5$, were predicted; two of these modes (B_2, B_3) were strongly coupled to an adjacent terrace atom. Comparing the results of the simulated 10° miscut surface with experiments on a 9° miscut H/Si(111) surface,[6] the simulations overestimated the stretch mode energies by ~1.3%; however, both the ordering and splitting (~11.4 cm^{-1}) of the symmetric (B_2) and the asymmetric (B_1) step stretch modes were in reasonable agreement with the experiment (16.4 cm^{-1} splitting). Experimentally, a single wag mode is observed at 614 cm^{-1} on 9° miscut surface,[55] whereas two nearly-degenerate modes at 595.2 cm^{-1} and 600.3 cm^{-1} were predicted on the 10.0° miscut surface. This corresponds to a ~2.7% underestimation of the wag mode energy. In addition, the simulations predicted the appearance of a significantly weaker mode at 641.4 cm^{-1}, which has not been observed on vicinal H/Si(111) surfaces.

The infrared-active terrace modes, labeled A_1 - A_3, were also predicted. Comparing the results of simulated 10° miscut surface with experiments on a 9° miscut surface, the simulation overestimated the energy of the in-phase terrace monohydride vibration A_1 by ~1%. A second weakly allowed terrace stretch mode, labeled A_3, was also predicted; however, this mode has not been observed experimentally. Two nearly degenerate wag modes at 609.1 cm^{-1} and 615.6 cm^{-1} were predicted. Although the polarizations of these modes are in good agreement with the 625.3 cm^{-1} and 628.7 cm^{-1}

modes observed experimentally,[55] the simulations overestimated the experimental energies by ~2.4%.

In conclusion, the simulations were in reasonable agreement with experiment. The simulations systematically overestimated the absolute energies of the stretch vibrations by ~1.2% (~25 cm^{-1}) and systematically underestimated the bend vibrations by ~2.6% (~15 cm^{-1}). The predicted mode orderings and polarizations were in good agreement with experiment.

2) Miscut towards $\langle \bar{1}\bar{1}2 \rangle$ direction

The Si-H vibrational modes of H/Si(111) surfaces miscut along the $\langle \bar{1}\bar{1}2 \rangle$ direction were also studied on two slabs with different terrace sizes: two terrace atoms (corresponding to a 19.4° miscut) and four terrace atoms (a 11.4° miscut). The optimized structures for the two slabs and their infrared-active Si-H vibrational modes are presented in Fig. 6.5. [The band nomenclature follows Ref. 6 for the four observed stretch modes (A_1, C_1, C_2, C_3) and Ref. 5 for the three observed wag modes (A_2, C_4, C_5).]

Severe interadsorbate strain between the step dihydride and the monohydride on the lower terrace led to significant structural relaxation as shown in Fig. 6.6(c). In the optimized structure, the step dihydride was titled from its bulk-terminated position by ~12.5°, leaving the Si-H_C bond 18.9° from the vertical. This value of the Si-H_C tilt angle was significantly lower than the 22° predicted by the cluster simulations of Raghavachari *et al.*,[57] but also significantly larger than the 3° rotation predicted by the slab calculations of Li *et al*.[9] In contrast, the strained monohydride (Si-H_A) tilted ~2° from the vertical, while remaining terrace monohydrides remained essentially in their bulk-terminated positions.

In agreement with experiment, three infrared-active step modes involving the coupled motion of the step dihydride and strained monohydride were predicted. The

Figure 6.6. (a, b) Slab structures for simulations of H/Si(111) surfaces miscut towards the $\langle \bar{1}\bar{1}2 \rangle$ direction. (c) The relaxed structure of the step dihydride; the bulk-terminated positions of dihydride atoms is shown in grey outline. (d) Calculated vibrational modes and experimental energies (at T = 90 K and room temperature for the stretch and bend modes, respectively). The transition dipole orientation is measured with respect to the $\langle 111 \rangle$ direction, shown by dashed line, for 11.4° miscut surface. The relative intensities are indicated in parentheses. Both structures were relaxed with a *k*-point mesh of 2 × 4 × 1 and energy cut-off of 800 eV. The vibrational mode energies for 19.4° and 11.4° miscut slab were calculated with 2 × 4 × 1 and 1 × 4 × 1 *k*-point meshes, and 750 eV and 700 eV energy cut-offs, respectively.

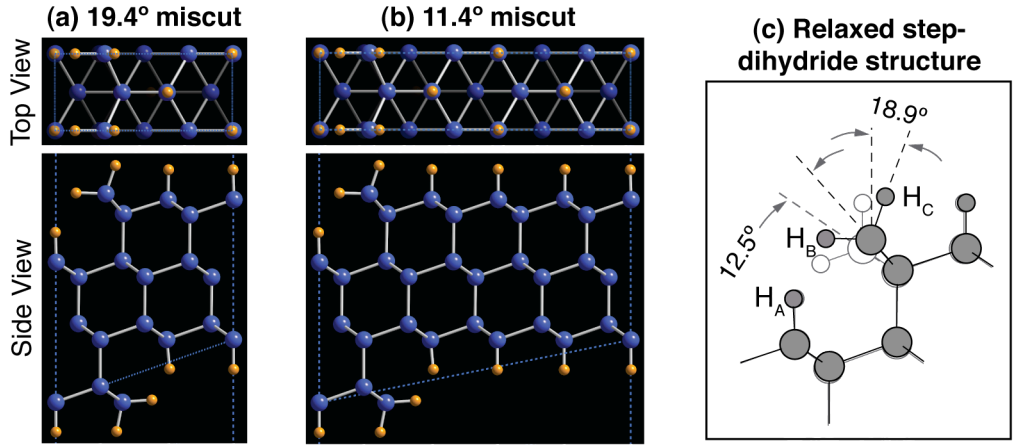

(d) Vibrational Mode Energies

Band	Mode	Transition Dipole Orientation	Energy (cm^{-1}) and (Rel. Intensity)		Experimental- 9° miscut (cm^{-1})	% Error
			19.4° miscut	11.4° miscut		
C_3	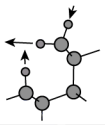	 93°	2152.5 (1.4)	2150.9 (1.4)	2135.7[6]	0.7
C_2	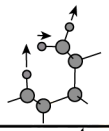	 6°	2122.4 (2.3)	2122.4 (2.8)	2102.5[6]	0.9
C_1	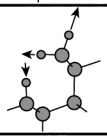	 2°	2126.3 (1.1)	2127.6 (0.9)	2095.6[6]	1.5
C_4	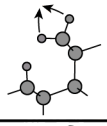	 36°	892.4 (1.7)	892.0 (1.7)	913[5]	2.3
C_5	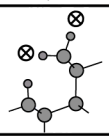	⊗	636.7 (3.2)	635.1 (3.4)	655.5[55]	3.1
C_6	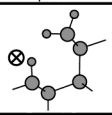	⊗	600.3 (0.6)	605.3 (0.5)	-	-
A_1		 1°	2105.1 (0.6)	2108.9 (2.6)	2081.4 (2 terr.), 2083.8 (4 terr.)[3]	1.1, 1.2
A_3	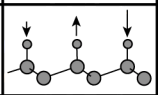	 1°	-	2102.3 (0.3)	-	-
A_2	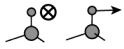	⊗ 	614.4, 621.8 (0.7, 2.3)	612.3, 614.7; 616.3 (1.2, 1.6; 4.3)	626.7, 628.6[55]	1.9, 2.0

near-degeneracy of two lowest energy modes led to some ambiguity in the assignment of these modes, which were originally named in order of increasing energy in the experimental spectrum. Since infrared absorption[6] and Raman scattering experiments[58] were performed on samples with a 9° miscut, and therefore the results of simulations of the 11.4° miscut surface (*i.e.,* exactly 4 terrace atoms) are quoted in the following. The highest energy mode at 2150.9 cm^{-1} was assigned to the highest energy experimental mode, C_3, as this mode was polarized in the plane of the surface and perpendicular to the step edge — in good agreement with both the infrared absorption and Raman experiments. The two remaining stretch modes corresponded primarily (but not exclusively) to the stretch bonds Si-H_A at 2122.4 cm^{-1} and Si-H_C at 2127.6 cm^{-1}. Experimentally, the C_2 mode has a near-vertical polarization in infrared absorption, as evidenced by the relative insensitivity of this mode to step orientation (*i.e.,* Fig. 5 in Ref. 6). This was consistent with a mode primarily arising from the motion of Si-H_A, the undistorted terrace monohydride. In contrast, infrared absorption data showed that the C_1 mode was entirely polarized in a plane perpendicular to the step edge, with significant normal and in-plane components. This was consistent with a mode primarily arising from the motion of Si-H_C. On the basis of these data, the mode at 2127.6 cm^{-1} was assigned to C_1, and the mode at 2122.4 cm^{-1} was assigned to C_2. Comparing the results of the simulated 11.4° miscut surface with experiments on a 9° miscut surface, the simulation overestimated the vibrational energies by ~1.1%, and reversed the ordering of the C_1 and C_2 modes.

Three low-frequency step bending modes were also predicted. The dihydride scissor and wag modes had energies of 892.0 cm^{-1} and 635.1 cm^{-1}, which were ~2.3% and 3.1% lower in energy than modes experimentally observed[5] at 913 cm^{-1} and 655.5 cm^{-1}. The wag mode of the strained monohydride Si-H_A, had an energy of ~605.3 cm^{-1}; however, no corresponding experimental mode was observed. This band may have been

obscured by the more intense terrace monohydride wag modes near 627 cm^{-1} (*vide infra*).

Three infrared-active terrace modes, labeled A_1 - A_3, were also predicted. Comparing the results of the simulated 11.4° miscut surface with experiments on a 9° miscut surface, the simulation overestimated the energy of the in-phase terrace monohydride vibration A_1 by ~1.2%. The calculated energy of the A_1 mode decreased with the terrace size, which was consistent with the experimental studies of Jakob *et al*.[3] A second weakly-allowed terrace stretch mode, labeled A_3, was also predicted; however, this mode has not been observed experimentally. Two nearly degenerate wag modes at 612.3 cm^{-1} and 614.7 cm^{-1} polarized parallel to the step edge and a single wag mode at 616.3 cm^{-1} polarized perpendicular to the step edge were predicted. Although the polarizations of these modes were in good agreement with the 626.7 cm^{-1} and 628.6 cm^{-1} modes observed experimentally,[55] the simulations underestimated the experimental energies by ~2.0%.

In conclusion, the simulations were in reasonable agreement with experiment. The simulations systematically overestimated the absolute energies of the stretch vibrations by ~1.1% (~23 cm^{-1}) and systematically underestimated the bend vibrations by ~2.4% (16 cm^{-1}). The predicted mode orderings and polarizations were in good agreement with experiment.

6.3.2.2. H/Si(110) surface

The Si-H vibrations on H/Si(110) surfaces were modeled by a vicinal H/Si(111) slab miscut by 35.2° towards the $\langle 11\bar{2} \rangle$ direction. The optimized structure of the slab and its infrared-active Si-H vibrational modes are shown in Fig. 6.7. The modes are labeled $E_1 - E_5$ in analogy with the $B_1 - B_5$ modes tabulated in Fig. 6.5 and observed on H/Si(111) slabs miscut by a less steep angle towards the $\langle 11\bar{2} \rangle$ direction. As expected

for a H-terminated surface with little interadsorbate strain, the optimized structure was nearly identical to the bulk geometry.

(a) Slab structure

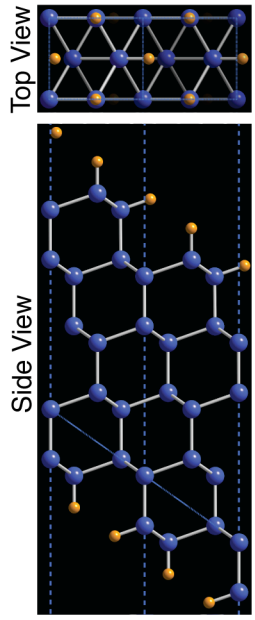

(b) Vibrational Mode Energies

Band	Mode	Transition Dipole Orientation	Energy (cm^{-1}) and (Rel. Intensity)	Experimental[59] (cm^{-1})	% Error
E_2	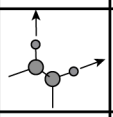	 3°	2115.7 (1.8)	2089.4	1.3
E_1	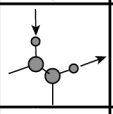	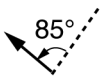 85°	2098.1 (0.9)	2070.8	1.3
E_3	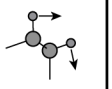	 91°	627.0 (1.6)	637, 649?	-
E_5	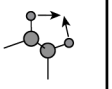	 1°	605.6 (0.9)	-	-
E_4	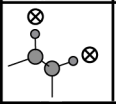	⊗	601.0 (2.8)	612	1.8

Figure 6.7. (a) Slab structure used for simulation of H/Si(110) surface, obtained as a H/Si(111) slab miscut by 35.2° towards the $\langle 11\bar{2} \rangle$ direction. (2 supercells are shown for clarity). (b) Calculated vibrational modes and experimental energies. The orientation of transition dipole vectors is sketched with respect to $\langle 110 \rangle$ direction, indicated by the dashed line. The relative intensities are indicated in parentheses. All calculations used a *k*-point mesh of 3 × 4 × 1 and energy cut-off of 800 eV.

Five infrared-active Si-H modes were predicted. The two highest energy modes corresponded to the symmetric, E_2, and asymmetric, E_1, monohydride stretch modes at 2115.7 cm^{-1} and 2098.1 cm^{-1} which were polarized perpendicular to and in the plane of the surface, respectively. Experimentally,[59] two modes with identical polarizations are observed at 2089.4 cm^{-1} and 2070.8 cm^{-1}, implying that the simulation overestimated the stretch mode energies by ~1.3%. The three lowest energy modes corresponded to wagging modes of the monohydrides. The E_5 mode was polarized normal to the surface with an energy of 605.6 cm^{-1}. The accuracy of this predicted energy could not be judged, as the low-frequency spectrum of H/Si(110) has only been measured with

radiation in the plane of the surface. The simulations predicted two modes polarized in the plane of the surface: the E_4 mode at 601.0 cm^{-1} corresponding to a vibration parallel to the $\langle 1\bar{1}0 \rangle$ direction and the E_3 mode at 627.0 cm^{-1} corresponding to a vibration parallel to the $\langle 001 \rangle$ direction. The polarization of the E_4 mode was in good agreement with the band observed experimentally at 612 cm^{-1}, suggesting that the simulation underestimated the experimental energy by ~1.8%. The experimental assignment of the E_3 mode is problematic, though, as two modes of the appropriate polarization were observed at 637 cm^{-1} and 649 cm^{-1}, respectively. One of these modes is presumably a defect mode; however, a definitive assignment cannot be made without additional data.

In conclusion, the simulations were in reasonable agreement with experiment. The simulations systematically overestimated the absolute energies of the stretch vibrations by ~1.3% (~27 cm^{-1}) and systematically underestimated the bend vibrations by ~1.8% (~11 cm^{-1}). The predicted mode orderings and polarizations were in very good agreement with experiment.

6.3.2.3. H/Si(100) surfaces

Although severe interadsorbate strain has prevented the experimental observation of the flat H/Si(100) surface, this structure has attracted a great deal of attention in simulation. The bulk-terminated H/Si(100) surface therefore served as a benchmark for comparison of present theoretical results with previous simulations. To understand the vibrational modes of the NH_4F-etched Si(100) surface, the missing-row morphology described in Chapter 3 was simulated. To understand the heterogeneous broadening observed on this surface, the effects of a variety of defects on H/Si(100) were also studied.

1) Bulk-terminated H/Si(100)

A single terrace on a bulk-terminated H/Si(100) surface has two-fold rotational symmetry; however, previous simulations[21-25] suggest that the ground state structure of

this surface would have dihydrides canted to relieve interadsorbate strain. To study these two structures, the flat H/Si(100) surface was simulated in two configurations: a symmetric configuration with externally imposed two-fold rotational symmetry and a relaxed configuration that allowed dihydride canting.[60] The relaxed structures for these configurations are shown in Fig. 6.8. The energy of the canted structure was lower than the symmetric structure by 0.14 eV per unit cell (which contained a single surface dihydride). The inter-hydride distance between H atoms on adjacent dihydrides was 1.574 Å in the symmetric configuration and 2.140 Å for canted dihydrides. The canting was also accompanied by an increase in H-Si-H bond angle from 101.3° to 104.8° and an increase in the bond lengths of the lower and upper Si-H bonds, b_1 and b_2, by 0.01 Å and 0.02 Å, respectively.

Four infrared-active modes were predicted for each configuration, as also shown in Fig. 6.8. The symmetric and antisymmetric stretch modes of the symmetric configuration, D^{s}_{ss} and D^{s}_{as}, respectively, were split by 20 cm^{-1} and had absolute energies ~100 cm^{-1} higher than the predicted energies for the strained dihydrides on vicinal H/Si(111) surface (*vide supra*) or observed on etched H/Si(100) surfaces (*vide infra*). The scissor and bend modes of the symmetric configuration, D^{s}_{s} and D^{s}_{w}, respectively, had predicted energies of 985.1 cm^{-1} and 624.5 cm^{-1}.

The vibrational modes and energies of the canted configurations were significantly different, displaying two independent stretches of the nearly-vertical and nearly-horizontal Si-H bonds, D^{c}_{up} and D^{c}_{dn}, respectively. The absolute energies of these modes were much smaller than the energies of the symmetric configuration, although the splitting of these modes (55.8 cm^{-1}) was much larger. The scissor and wag modes of this configuration, D^{c}_{sr} and D^{c}_{w}, respectively, were predicted at 887.2 cm^{-1} and 633.5 cm^{-1}.

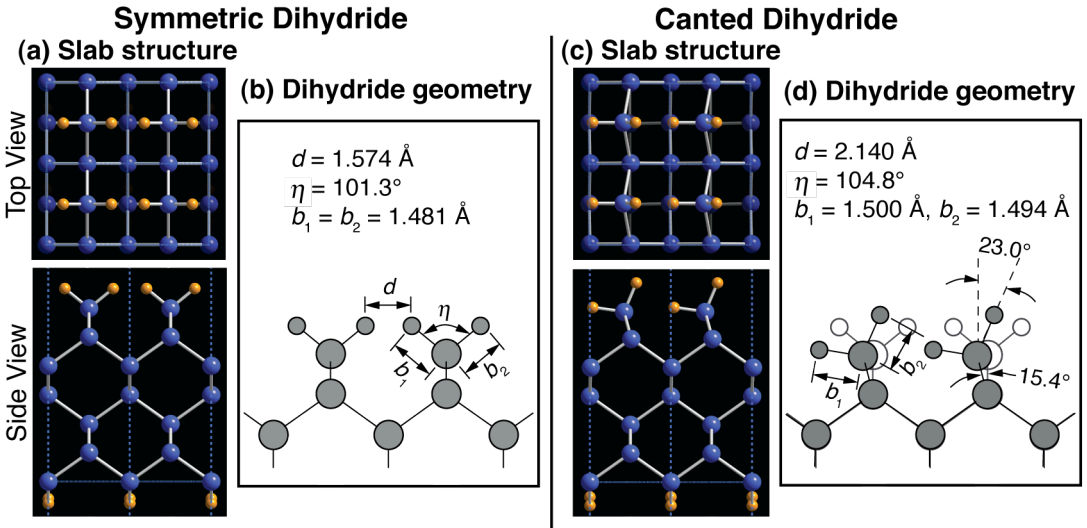

(e) Vibrational mode energies

Band	Mode	Transition Dipole Orientation	Energy (cm^{-1}) and (Rel. Intensity)
D^s_{ss}			2229.6 (0.9)
D^s_{as}			2209.8 (1.7)
D^s_{s}			985.1 (1.5)
D^s_{w}		⊗	624.5 (2.1)

(f) Vibrational mode energies

Band	Mode	Transition Dipole Orientation	Energy (cm^{-1}) and (Rel. intensity)
D^c_{up}		23°	2155.0 (1.4)
D^c_{dn}		82°	2099.2 (1.2)
D^c_{s}		29°	887.2 (1.8)
D^c_{w}		⊗	633.5 (2.2)

Figure 6.8. (a, d) The slab structures for simulation of bulk-terminated H/Si(100) surface in symmetric and canted configurations. (b) The relaxed dihydride geometry for the symmetric structure, and (e) the canted dihydrides (The symmetric dihydride structure is shown in grey outline for comparison). (c, f) Vibrational modes for the two structures. The atomic distances, labeled in (b) and (e), were calculated with the hard PAW potentials and PBE functionals, and are likely overestimated by 0.7% (error in the bulk Si lattice constant value). The *k*-mesh for all calculations was 8 × 8 × 2 and energy cut-offs for the structure relaxation and the vibrational energy calculations were 850 eV and 750 eV, respectively.

In summary, simulations of the flat H/Si(100) surface predicted canting of the dihydrides to relieve interadsorbate strain, which was consistent with the predictions of previous researchers. These predictions could not be compared to experimental observations, as atomically flat H/Si(100) surfaces have never been prepared.

2) Missing-row morphology on H/Si(100)

The missing-row morphology observed on NH_4F-etched H/Si(100) surfaces and discussed in Chapter 3 was simulated with a 2 × 1 supercell of the H/Si(100) cell. In the optimized structure shown in Fig. 6.9,[61] the unstrained dihydrides had a H-Si-H bond angle of 109° and the Si-H bond length of 1.500 Å. In contrast, the strained dihydrides were canted, and the canting angle was ~1° larger than that of canted dihydrides on flat H/Si(100) surface [the "up" Si-H bond in this structure was tilted by 21.9° from the vertical, compared to the 23.0° tilt on the flat Si(100) surface]. This difference in canting angle led to an interhydride spacing of 2.174 Å among the strained dihydrides — 0.034 Å larger than the spacing predicted for the canted dihydrides on a flat H/Si(100) terrace.

(a) Slab structure

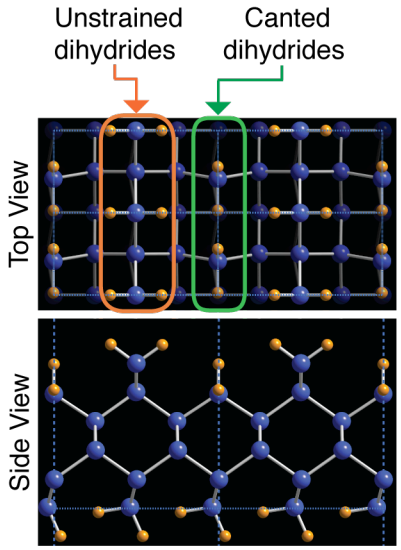

(b) Vibrational Mode Energies

Band	Predicted Energy (cm^{-1})	Experimental (cm^{-1})	% Error
D^{c}_{up}	2142.9	2143.5	0.0
D^{u}_{as}	2138.4	2112.2	1.2
D^{u}_{ss}	2126.9	2103.5	1.1
D^{c}_{dn}	2076.7	2083.3	0.3
D^{u}_{s}	892.2	917.0	2.7
D^{c}_{s}	873.4	906.4	3.6
D^{c}_{w}	646.6	659.6	2.0
D^{u}_{w}	635.3	655.7	3.1

Figure 6.9. (a) Slab structure for the simulation of missing-row morphology observed on NH_4F-etched H/Si(100) surface. (b) Calculated vibrational modes and the experimental energies (from Chapter 3). The mode definitions are similar to those shown in Fig. 6.8; the modes for unstrained dihydrides are denoted with the superscript "u" and are identical to the modes of symmetric dihydride structure. The structural optimization and vibrational energy calculations used 4 × 8 × 2 and 3 × 6 × 1 *k*-point meshes, and 850 eV and 750 eV energy cut-offs, respectively.

Four infrared-active stretch modes were predicted. The simulation overestimated the energies of the symmetric and antisymmetric stretch of the unstrained dihydride, D_{ss}^{u} and D_{as}^{u}, respectively, by ~1.2%. The ordering and the 11.5 cm^{-1} splitting of these modes were in good agreement with the ordering and 8.7 cm^{-1} splitting observed experimentally. Somewhat surprisingly, the simulation slightly underestimated the energies of both the "up" and the "down" stretch modes, D_{up}^{c} and D_{dn}^{c}, respectively, by ~0.2%. This stood in stark contrast to the uniform overestimation of stretch mode energies on other H-terminated surfaces of silicon. The ordering and the 66.2 cm^{-1} splitting of these modes were also in good agreement with the ordering and 60.2 cm^{-1} splitting observed experimentally.

Four low-frequency modes were also predicted. The scissor modes of the unstrained and strained canted dihydrides, D_{s}^{u} and D_{s}^{c}, had energies of 892.9 cm^{-1} and 873.4 cm^{-1}, which underestimated the experimental values by 2.7% and 3.6%, respectively. The wag modes of the unstrained and strained canted dihydrides, D_{w}^{u} and D_{w}^{c}, had energies of 646.6 cm^{-1} and 635.3 cm^{-1}, which underestimated the experimental values by 2.0% and 3.1%, respectively.

In conclusion, the simulations were in reasonable agreement with experiment; however, the stretch modes of the strained species were anomalously low in comparison to all other stretch modes. Because of this, the splitting between strained and unstrained stretch vibrations (*i.e.,* the splitting between D_{ss}^{u} and D_{dn}^{c} or D_{up}^{c} and D_{as}^{u}) were in poor agreement with experiment. No similar trend was observed in the energies of the low frequency modes.

3) Defects on H/Si(100)

The effects of point defects on the vibrational spectrum of NH_4F-etched Si(100) were studied by removing Si atoms from ideal slabs. Due to computational constraints arising from the large number of atoms in these structures, the calculations were

performed with a real-space projector basis. Therefore, the absolute mode energies may not be comparable to those reported in previous sections, which used a reciprocal-space projector basis.

a) Defects in strained dihydride rows

To simulate the effects of point defects on strained dihydride rows, Si atoms were sequentially removed from the 4 × 2 supercell of flat H/Si(100) shown in Fig. 6.10(a). Three defective structures were generated, corresponding to the removal of one, two, or three adjacent dihydrides to generate one, two, or three pairs of highly strained opposing monohydrides as shown in Fig. 6.10 (b - d). With the imposition of periodic boundary conditions, these structures represent surfaces with alternating infinite and defective rows of strained dihydrides.

The finite rows of strained dihydrides displayed significantly different cant angles and lattice relaxations than the infinite rows. As expected, the strained dihydrides on opposite ends of the two- and three-atom-long defective dihydride rows canted in opposite directions. Interestingly, the canting was not symmetric; it was influenced by the canting of the adjacent infinite dihydride rows. As a result, the end dihydride that was canted in the same direction as the infinite row was canted by a significantly larger angle than the dihydride at the other end of the row. Thus, interadsorbate strain in one row significantly affected the structure of adjacent rows. This effect was also seen in the cant angles. For example, strained dihydrides in the infinite row that were adjacent to defects (*i.e.,* missing dihydrides) were canted by ~2° less than those adjacent to dihydrides.

The opposing monohydrides generated by the removal of dihydrides were highly sterically strained. The distance between the two monohydride H atoms was 1.68 Å, far below the 2.16 Å spacing predicted for adjacent H atoms in the strained, canted

dihydride rows. This spacing was also much smaller than the 2.4 Å van der Waals diameter of hydrogen.

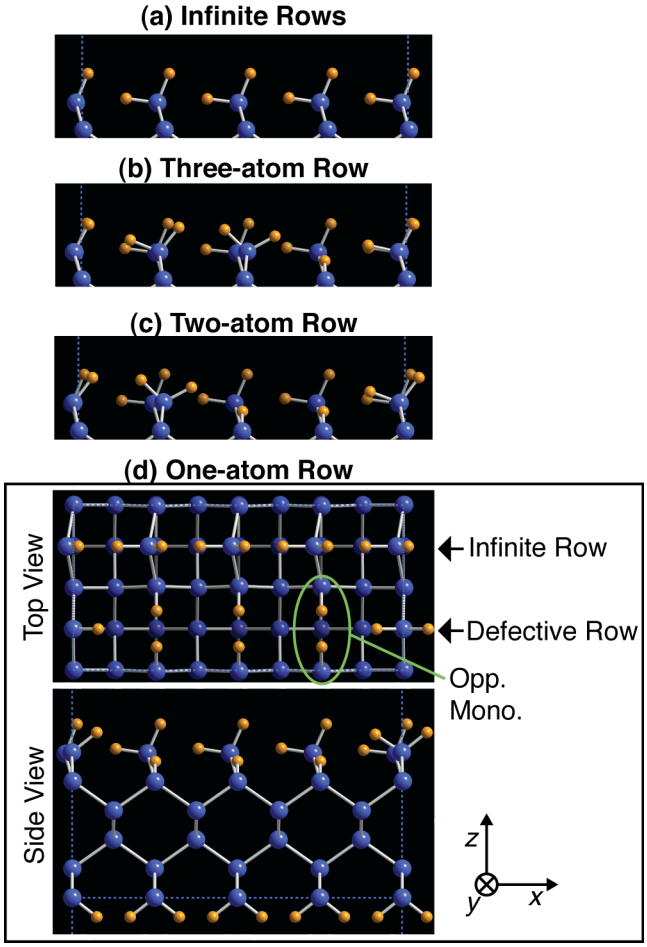

Figure 6.10. (a - d) The 4 × 2 H/Si(100) supercell structures used to simulate the effects of point defects on strained dihydride rows. For (a - c), only top section of the side view is shown; the remainder is identical to (d). The structural optimization and vibrational energy calculations used 2 × 3 × 2 and 1 × 2 × 1 *k*-point meshes and 850 eV and 750 eV energy cut-offs, respectively. The Cartesian axes are defined with respect to the side view.

Figure 6.11 shows the Si-H stretch region of the simulated spectra of the four structures shown in Fig. 6.10 (a - d). The spectrum of the defect-free structure consisted of two principle modes: the in-phase vibrations of the "down" and "up" Si-H bonds at 2102 cm^{-1} (*x*-polarized spectrum) and 2149 cm^{-1} (both *x*- and *z*-polarized spectra). The small band at 2098 cm^{-1} in the *x*-polarized spectrum was nominally an out-of-phase

stretch mode of "down" Si-H bonds. Although this mode is formally symmetry forbidden, numerical inaccuracies resulted in finite oscillator strength.

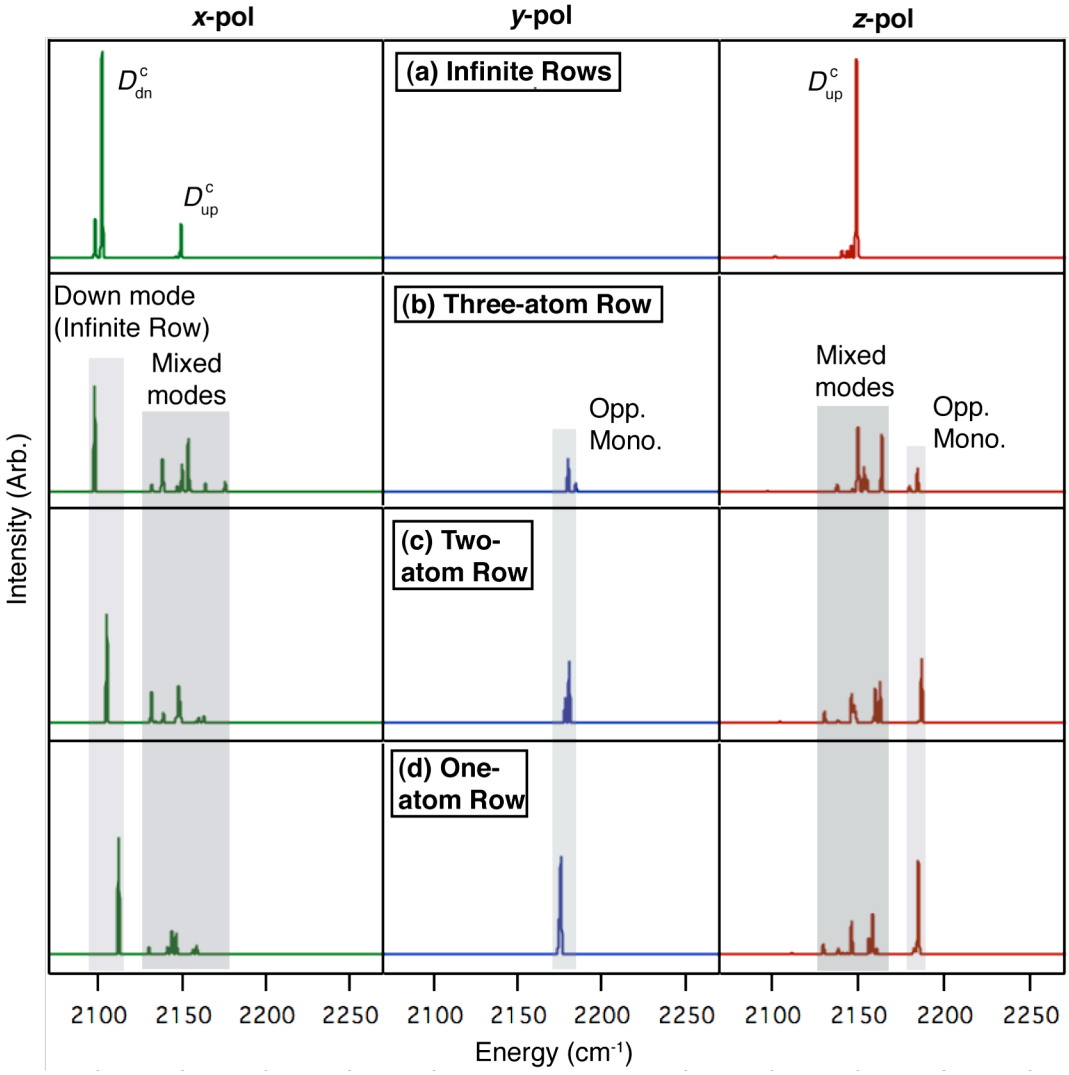

Figure 6.11. Calculated polarization-resolved spectra in the Si-H stretch region for the 4 × 2 H/Si(100) structures shown in Fig. 6.10 (a - d). The axes are defined in Fig. 6.10(d). A 0.9 cm^{-1} homogenous linewidth and a 1.0 dielectric constant of the adsorbate layer were assumed.

The removal of a single strained dihydride in the supercell (to create an infinite array of three-atom-long rows of strained dihydrides) induced a dramatic spectral change. First, a well-defined mode corresponding to the in-phase stretch of the "down" Si-H bonds in the infinite (defect-free) row was observed at 2097 cm^{-1}. Second, a large

number of infrared-active modes appeared in the 2140-2175 cm^{-1} range. These modes consisted primarily of Si-H stretch vibrations in the three-atom-long rows; however, modes in the 2149-2155 cm^{-1} range also had significant contributions from the "up" Si-H bonds in the infinite row. As a result, a well-defined mode corresponding to the in-phase stretch of the "up" Si-H bonds was *not observed*. Finally, two new modes corresponding to the antisymmetric and symmetric stretches of the two highly strained, opposing monohydrides appeared at 2180 cm^{-1} (*y*-polarized spectrum) and 2184 cm^{-1} (*z*-polarized spectrum), respectively.

Removal of a second and third strained dihydride in the supercell had much less dramatic effects. The most notable was a blue shift of the energies of the in-phase vibration of "down" Si-H bonds in the infinite dihydride row to 2105 cm^{-1} (two-atom chain) and 2112 cm^{-1} (isolated dihydride). In contrast, the mixed modes with significant contributions from the "up" Si-H bonds in the infinite dihydride row showed no systematic shift, although their energy range broadened to ~2145-2160 cm^{-1}. Small changes in the energies of other modes were also observed.

A number of important conclusions can be drawn from these simulations. As expected, point defects in strained dihydride rows enabled significant structural relaxations within the row that were accompanied by the appearance of new infrared-active vibrational modes. On average, the new modes appeared at somewhat higher energies than on the perfect structure. A bit more surprisingly, point defects led to significant shifts in the vibrational energies of adjacent dihydride rows. Finally, Si-H stretch vibrations of the highly strained monohydrides had very high energies, ~20-25 cm^{-1} higher than that of the highest strained dihydride stretch modes. This contradicts the common assumption that the vibrational energies of monohydride species are always less than those of dihydride species.

b) Defects in unstrained dihydride rows

To simulate the effects of point defects on the missing-row structure, adjacent unstrained dihydrides were sequentially removed from the initially ideal 4 × 2 supercell shown in Fig. 6.12(a) to generate the three defective structures shown in Fig. 6.12 (b - d). The removal of one unstrained dihydride generated two highly strained opposing monohydrides, as shown in Fig. 6.12(b). The removal of a second or third unstrained

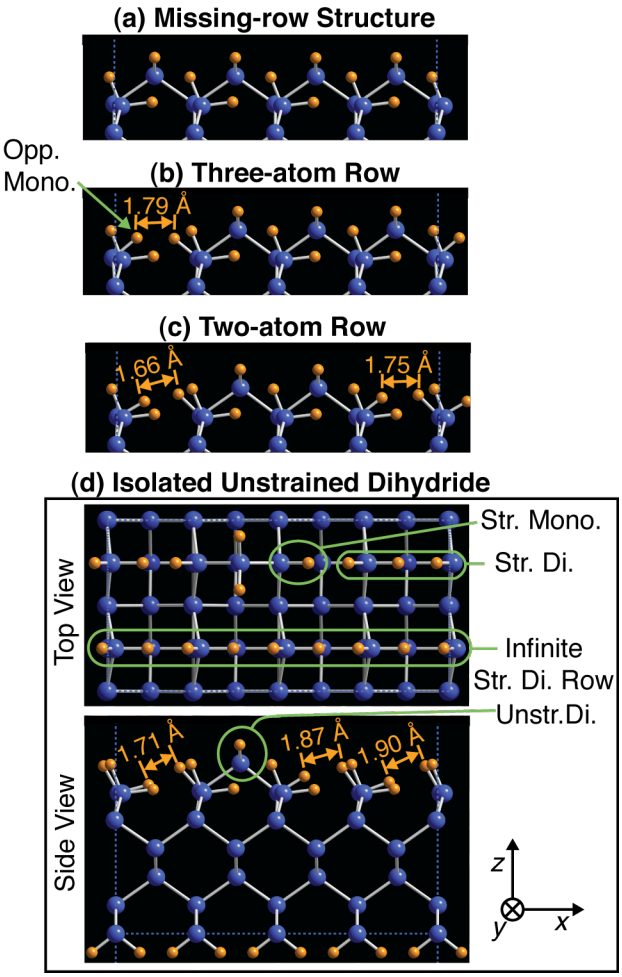

Figure 6.12. (a - d) The 4 × 2 H/Si(100) supercells used to investigate the effects of point defects on the missing-row structure. For (a - c), only the side view is shown; the remainder is identical to (d). (e) The structural optimization and vibrational energy calculations used 2 × 3 × 2 and 1 × 2 × 1 *k*-point meshes and 850 eV and 750 eV energy cut-offs, respectively. The Cartesian axes are defined with respect to the side view.

dihydride produced one or two strained dihydrides, respectively, "trapped" between the opposing strained monohydrides as shown in Fig. 6.12 (c, d). As expected, the "trapped" dihydrides canted to relieve interadsorbate strain. Nevertheless, these species were highly strained, as the rigid monohydrides prevented these species from relaxing as much as the infinite rows of strained dihydrides. For example, the average interhydride spacing in the defective row in Fig. 6.12(d) was 1.83 Å, far shorter than the 2.17 Å interhydride spacing in the infinite strained dihydride row.

Figure 6.13 shows the Si-H stretch region of the simulated spectra of the four structures shown in Fig. 6.12 (a – d). As expected, the spectrum of the defect-free structure consisted of four principal modes: the symmetric (*z*-polarized) and antisymmetric (*y*-polarized) Si-H stretches of the unstrained infinite row at 2130 cm^{-1} and 2144 cm^{-1}, respectively, and the in-phase vibrations of the "down" (*x*-polarized) and "up" (*z*-polarized) Si-H bonds in the strained rows at 2085 cm^{-1} and 2146 cm^{-1}, respectively. As in the previous case, numerical inaccuracies resulted in a number of formally symmetry-forbidden modes having small but finite oscillator strengths.

The sequential removal of unstrained dihydrides from the supercell had surprisingly small effects on the original modes. As shown in Fig. 6.13, disorder had a negligible effect on the energies of the symmetric and antisymmetric Si-H stretches of unstrained dihydrides (~2 cm^{-1}). The mode energies of the infinitely long, strained dihydride rows were somewhat more affected. The energy of the in-phase vibration of the "down" Si-H bonds varied by ~14 cm^{-1} while remaining a single, well-defined mode, whereas the "up" Si-H bonds contributed to a number of normal modes in the 2142–2149 cm^{-1} range.

The largest changes in the Si-H spectrum were due to the introduction of the highly strained monohydride and dihydride species in the defective species. As seen in Fig. 6.13 (b - d), these species led to highly blueshifted modes. The energies of these

modes were highly structure dependent. In general, the stretch vibrations of the strained monohydrides had energies in the range of 2150-2190 cm^{-1}, whereas those of the strained dihydrides had energies in the range 2160-2260 cm^{-1}.

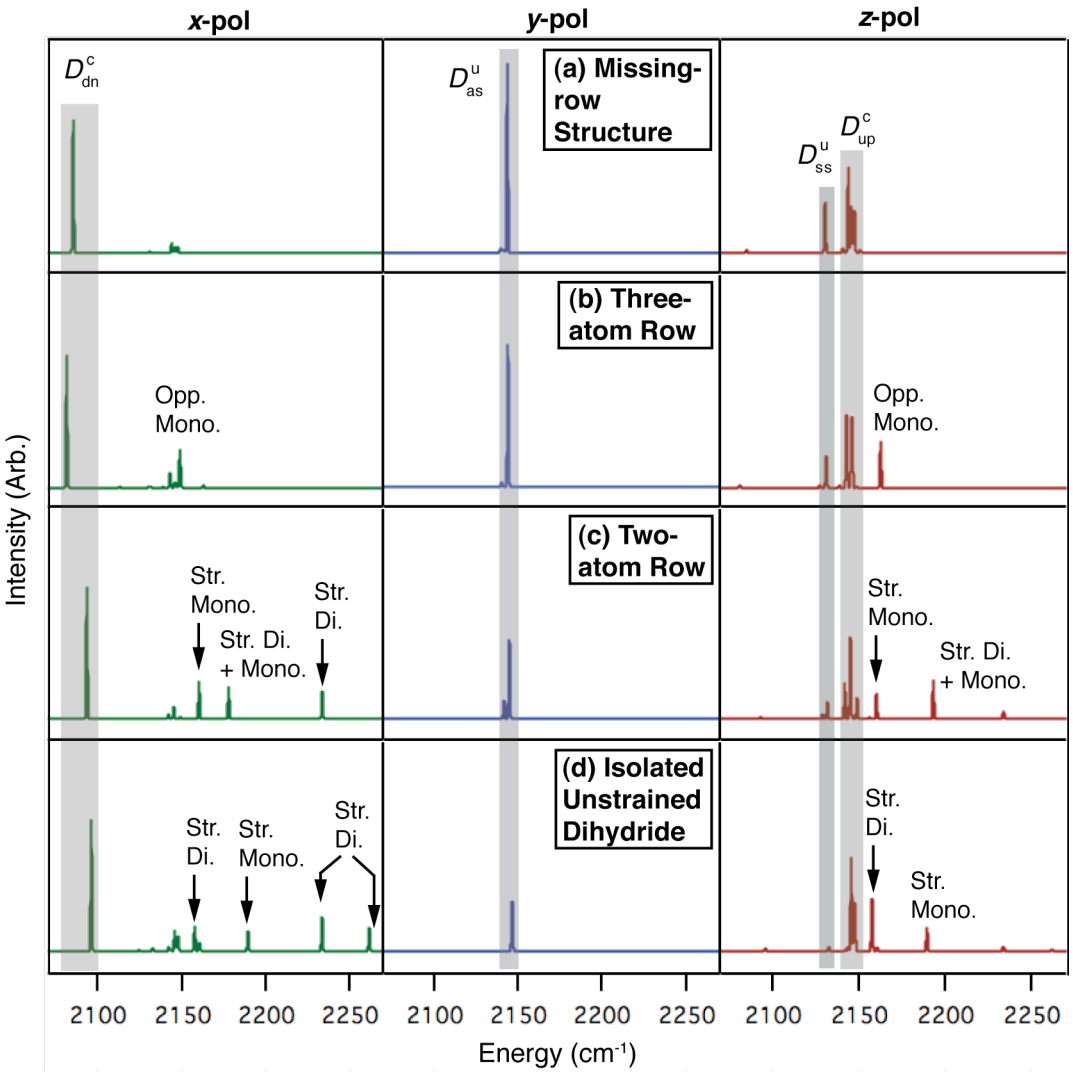

Figure 6.13. Calculated polarization-resolved spectra for the 4 × 2 H/Si(100) surface structures shown in Fig. 6.12 (a - d). A 0.9 cm^{-1} homogeneous linewidth and 1.0 dielectric constant of the adsorbate layer were assumed.

In conclusion, point defects in the unstrained dihydride rows of the missing-row structure led to modest (~10 cm^{-1}) blueshifts in the D^c_{dn} mode while introducing new defect modes corresponding to the vibration of highly strained monohydrides and

dihydrides. The Si-H stretch modes associated with the (highly strained) defect had energies that were uniformly higher than those on the defect-free surface.

c) Monohydride defects

To investigate the relative energies of a variety of strained and unstrained monohydride species, the two 4 × 2 defective H/Si(100) supercells in Fig. 6.14 (a, b) were constructed. From left to right, each structure contains a monohydride strained by an adjacent dihydride, two highly strained opposing monohydrides, and an unstrained monohydride. The two structures differ in the relative orientation of the dihydride cant

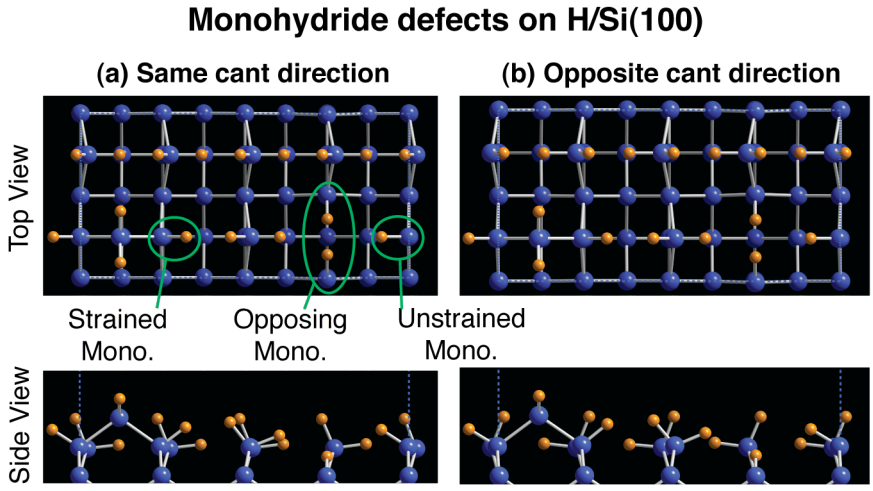

(c) Monohydride stretch energies and interhydride distances

Mode	Energy (cm^{-1})		Interhydride distance (Å)	
	Same	Opposite	Same	Opposite
Opposing Mono. symmetric stretch	2188.0	2187.2	1.68	1.69
Opposing Mono. antisymmetric stretch	2182.9	2181.9		
Strained Mono. stretch	2142.9	2142.6	2.10	2.10
Unstrained Mono. stretch	2105.6	2114.6	2.96	2.89

Figure 6.14. (a, b) The 4 × 2 H/Si(100) supercells used to simulate the vibrational modes of a variety of strained and unstrained monohydrides. (c) Monohydride Si-H stretch energies and interhydride distances.

angles in the defective and defect-free rows. The dihydride in the defective row cants in the same direction as those in the defect-free row in the structure in Fig. 6.14(a) and in opposite direction in the structure in Fig. 6.14(b).

The relative steric strains on the monohydrides are reflected in the interhydride distances tabulated in Fig. 6.14(c). The ~2.9 Å separation between the unstrained monohydrides and their nearest hydrogen neighbor is far above the 2.4 Å van der Waals diameter. Monohydrides strained by a neighboring dihydride have an intermediate strain as shown by their 2.10 Å interhydride separation. In contrast, the opposing monohydrides are severely sterically strained with a 1.69 Å interhydride spacing.

Increasing steric strain led to a dramatic blueshift in the monohydride Si-H stretch modes.[62] The unstrained monohydrides had an average Si-H stretch mode energy of 2110 cm^{-1} which was in good agreement with the 2109 cm^{-1} predicted energy of the (unstrained) H/Si(111) stretch mode discussed in Section 6.3.2.1. This energy is blueshifted by ~33 cm^{-1} when the monohydride is strained by an adjacent dihydride and by ~75 cm^{-1} in the highly strained opposing monohydride configuration.

Interestingly, the unstrained monohydrides were much more sensitive to small structural changes in the adjacent rows than the strained species. Changing the cant orientation of the adjacent row resulted in ≤1 cm^{-1} shifts in Si-H stretch energies of the strained species, but a 9 cm^{-1} shift in the energy of the unstrained monohydride stretch vibrations.

6.4. Discussion

The calculations presented in previous section predicted the vibrational energies for various H/Si(111), H/Si(110), and H/Si(100) surfaces in agreement with the experimental values to within ~1.3% (26 cm^{-1}) for the stretch modes and within ~3.0 % (20 cm^{-1}) for the bending modes. The errors were predominantly systematic and were dependent on the strain of the site (*vide infra*). With this accuracy and the nature of

systematic errors, the simulations could explain the profound line broadening observed in the of NH_4F-etched Si(100) spectra due to point defects on the surface.

This section first presents a comparison of the accuracy of present simulations to previous simulations on these surfaces in Section 6.4.1. The strain-dependence of errors of the vibrational mode energies observed in the results, and its implications are then discussed in Section 6.4.2. Section 6.4.3 discusses the effects of point defects on the spectral band broadening for the H/Si(111) and H/Si(100) surfaces. Finally, potential sources of error in the vibrational energy calculations, and the future directions to improve on these calculations are discussed in Section 6.4.4.

6.4.1. Comparison with previous works

In previous simulations of H/Si surfaces, different quantities have been used to judge the accuracies of vibrational energy calculations. For the H/Si(111) surface, which have only a single stretch and bend modes, absolute errors have been used to estimate the theoretical accuracy. For other modes such as defect modes on H/Si(111), the mode ordering and splittings of different modes have been used as the important indicators of accuracy. In the following, the absolute energies or the energy splittings of the modes have been used to compare present simulations with previous simulations depending on the system.

The accuracy of the two vibrational energies of H/Si(111) surface in present work (~1%, ~3%) was comparable to the calculations of Sandford *et al.*[10] (~1%, ~2%), and much better than that of Honke *et al.*[20] (~1%, ~9%), Li *et al.*[8] (~6%, ~9%), and Kaxiras *et al.*[7] (~5%, ~9%). For H/Si(110) surface, present simulation accurately reproduced the mode splitting between the two Si-H stretch modes with highly accurate absolute energies, whereas the semi-empirical simulations of Graschus *et al.*[11] did not accurately yield the mode splitting even though they obtained highly accurate mode energies.

The incorrect ordering of step-dihydride modes (C_1, C_2, C_3) of vicinal H/Si(111) surface in present work was an exception to previous studies by Raghavachari *et al*.[4] and Li *et al*.,[9] which predicted correct mode ordering of these modes with mode splittings much closer to the experimental values. Raghavachari *et al*. obtained C_1-C_2 and C_2-C_3 splittings of 30 cm^{-1} and 16 cm^{-1}, respectively, compared to the experimental values of 33 cm^{-1} and 7 cm^{-1}, and Li *et al*. calculated these values to be 33.5 cm^{-1} and 11.6 cm^{-1}. The absolute energies, however, were not reported in these calculations. The incorrect mode ordering in present results can be explained by the strain dependence of errors (*vide infra*).

For H/Si(100) surface, the ordering of the two canted dihydrides stretch modes was consistent with the simulations of Freking *et al.*[25] and Arnold *et al.*;[28] however, the mode splitting of 56 cm^{-1} was much smaller than the 96 cm^{-1} and 65 cm^{-1} splittings obtained by these researchers with the density functional perturbation theory. The mode ordering was reverse to those predicted by the tight-binding calculations of Tagami *et al*.[26,27] (the two calculations predicted splitting values of 0 and 194 cm^{-1}), and the DFT simulations[24] by the same researchers (which predicted a splitting of 48 cm^{-1}). Although unobserved experimentally, the mode ordering predicted by present calculations was similar to that of the canted dihydride modes in the missing-row morphology, suggesting the current prediction (and that of Freking *et al.* and Arnold *et al.)* to be the correct ordering for these modes.

The scissor and wag mode energies of H/Si(100) were lower than the 822.7 cm^{-1} and 613.0 cm^{-1} predicted energies for these two modes by Freking *et al*. Tagami *et al*.,[26] however, predicted a energy range of 968 - 1,129 cm^{-1} for the scissor mode and energy of either 596 cm^{-1} or 678 cm^{-1} for the wag mode (the other mode they ascribed to the twist mode which would be infrared-inactive); therefore an absolute comparison of their predictions with present results cannot be made.

6.4.2. Strain Dependence of Errors

The errors in the vibrational energies of stretch modes were highly dependent on the strain on the site. For the stretch modes involving unstrained Si-H bonds only (Fig. 6.5, 6.6, 6.7, and 6.9), the overestimation of the mode energies was consistently ~1.0 - 1.5% (21 - 32 cm^{-1}). For the stretch vibrations of strained species, mode energies had much less errors. The stretch modes of the strained Si-H_B and Si-H_C bonds on vicinal H/Si(111) surfaces in Fig. 6.6, which were strained on only one side, showed lower errors of 0.7% and 0.9%, respectively, in the vibrational energies. The stretch modes of the strained, canted dihydrides in the missing-row morphology, which are strained on both sides, had errors of ~0.3%. The errors of bend mode energies did not show such dependence on strain.

Although the origin of this strain dependence of errors is unclear, these systematic errors dependent on strain can explain the discrepancies in the predicted ordering and energy splittings on vicinal H/Si(111) surfaces and the missing-row morphology on H/Si(100) surfaces. On the vicinal H/Si(111) surfaces miscut towards the $\langle \bar{1}\bar{1}2 \rangle$ direction, shown in Fig. 6.6(c), the energies of the C_1 and the C_2 modes were predicted in reverse order than the experimental values. The C_1 mode predominantly involved stretch vibrations of the unstrained Si-H_C bond, whereas C_2 mode predominantly involved stretch vibrations of the strained monohydride Si-H_A. The differences in the errors of the unstrained and the strained sites stretch energies (up to ~32 cm^{-1}) and the relatively close energies of these modes (<10 cm^{-1}) can account for the discrepancy in the predicted mode ordering. Similarly, the significantly lower energy splittings predicted for the C_1 and C_3 modes (17 cm^{-1}) than the experimental value of 40 cm^{-1} could be explained by only the C_3 mode involving predominant vibrations of the strained (Si-H_B) bond. The discrepancy of splitting between strained and unstrained stretch vibrations on the H/Si(100) missing-row morphology (*i.e.,* the

splitting between D_{ss}^{u} and D_{dn}^{c} or D_{up}^{c} and D_{as}^{u}) with experiment is also a result of the differences in the errors of two sites.

6.4.3. Point Defects and Spectral Broadening

The simulations of point defects on H/Si(111) and H/Si(100) surfaces explained different extents of the heterogeneous broadening of infrared-bands on the two surfaces. On (defective) vicinal H/Si(111) surfaces, calculations predicted red shifts of ~2 cm^{-1} in the terrace Si-H stretch mode A_1 [Figs. 6.5 and 6.6] relative to the mode energies on flat H/Si(111) surface. This red shift and associated heterogeneous broadening was consistent with the previous studies of the effect of dynamic dipole coupling on the energy shifts on Si-H stretch bands on H/Si(111) surfaces.[3,63]

On Si(100) surface, point defects led to very different mechanisms of spectral broadening and much larger band broadening, particularly for the vibrations involving strained sites. Defects in the strained, canted dihydride rows (Fig. 6.10) led to significant structural changes and resulted in many new stretch modes over a range of ~35 cm^{-1}. In addition, these point defects varied the vibrational energy of the "down" mode of neighboring canted dihydride row over a range of ~15 cm^{-1}. Defects in the unstrained dihydride rows, as shown in the structures in Fig. 6.12, caused the "down" mode energies in the neighboring canted dihydride rows to vary by up to 16 cm^{-1} relative to the flat H/Si(100) surface shown in Fig. 6.10(a), while multiple modes involving the "up" vibrations were observed over a energy range of ~7 cm^{-1}. These energy shifts showed that even when the strained, canted dihydride row has no defects in it, defects in neighboring rows can vary their stretch vibration energies by ~31 cm^{-1}.

For the unstrained dihydride stretch modes, the simulation of defects predicted much smaller energy shifts. Decreasing the unstrained dihydride row length from infinite to one [Fig. 6.12 (a - d)] produced a blue shift of ~3 cm^{-1} in the stretch mode energies. When the unstrained dihydride had canted dihydride row as its neighbors [Fig.

6.10(d)], its stretch energies were same as the energies of unstrained dihydride in the missing-row structure [Fig. 6.12(a)],[64] suggesting that canting of neighboring dihydride did not affect the stretch energies of an unstrained dihydride.

These simulations showed that point defects on H/Si(100) can introduce long range disorder in the structure of strained dihydrides and cause large shifts in their vibrational energies, thereby explaining the large broadening observed for the strained dihydride bands in the NH_4F-etched H/Si(100) spectra compared to the unstrained dihydride bands in the spectra.

6.4.4. Simulation Accuracy and Scope for Improvement

The DFT simulations had three principles sources of errors. First were finite approximations used on many formally infinite parameters, including the sizes of the basis set, the *k*-point mesh, and the slab as well as the vacuum spacing. The errors with respect to each of these parameters were minimized within the given computational limits, and increasing the limits on any one of these parameters would not improve the accuracy of the mode energies by more than ~1 cm^{-1}. Second was the choice of exchange correlation functionals and pseudopotentials. The vibrational mode energies showed much larger variations (~10 cm^{-1}) with functional choice and slightly less variation with the core-radius of the pseudopotentials. In this study, only three functionals and PAW pseudopotentials were tested. Further investigation and optimization of functionals and pseudopotentials are warranted. Finally, these calculations assumed harmonic potentials and absolute zero conditions.

The anharmonicity of a potential depends on the bonded atoms (atomic mass, nature of bonds etc.) and the neighboring chemical environment. Therefore, strained and unstrained bonds may have different anharmonicities and thus different systematic trends in simulation accuracy. Researchers have often corrected for the errors induced by harmonic approximation by including a multiplicative correction factors either to the

force field (used to calculate the vibrational energies) or directly to the vibrational energies.[65] In recent year, more rigorous methods to model anharmonicity of interatomic potentials in first principles calculations have been developed.[66] These methods are computationally more expensive, but are becoming feasible with existing computational resources. Further investigations of the role of anharmonicities are also warranted.

The errors due to finite temperatures are likely to be small in magnitude. Experimental investigation of the spectrum of H/Si(111)[5] and H/Si(100)[67] surfaces show that 200 K changes in temperature lead to ~5 cm^{-1} changes in vibrational energy; however, the relative energies of the stretch modes do not change appreciably. A temperature-dependent study of H/Si(111) surface spectra by Dumas *et al*.[54] attributed these shifts to coupling of surface phonons to the (low-energy) bulk phonons. Therefore, the inclusion of finite temperature effects is not likely to improve the accuracy of the vibrational energy calculations significantly.

6.5. Conclusions

The ground state structures and vibrational spectra of ideal and defective H/Si(111), H/(110) and H/Si(100) surfaces were simulated using DFT. The simulated vibrational energies were within 1.5% of the experimental values for the Si-H stretch modes and with ~3% of the experimental values for the bend modes. The stretch mode energies were typically overestimated whereas the bend mode energies were consistently underestimated.

The errors of the stretch mode energies were dependent on the strain of the site. The unstrained sites had the stretch mode energies consistently overestimated by ~ 1.0-1.5%. The strained sites with strain on only one side displayed errors of ~ 0.7-0.9%, and the sites strained on two Si-H bonds had errors of ~0.3% or less. The origin of this strain dependence of errors is unclear.

The simulation predicted the two vibrational energies of H/Si(111) surface with accuracy comparable to the calculations of Sandford *et al.*[10] (stretch ~1%, bend ~2%). The simulations of flat H/Si(110) surface reproduced absolute mode energies as well as mode splitting with high accuracy — an improvement over previous calculations of Graschus *et al.*[11] The simulations of vicinal H/Si(111) miscut towards the $\langle \bar{1}\bar{1}2 \rangle$ direction yielded incorrect mode ordering, whereas previous simulations of Raghavachari *et al.*[4] and Li *et al.*[9] obtained it correctly. This discrepancy was attributed to the strain dependence of errors.

For bulk-terminated H/Si(100) surface, the calculations predicted canting of the dihydrides and independent stretch modes for the two Si-H bonds of the dihydride in agreement with previous simulations by Freking *et al.*[25] and Arnold *et al.*[28] Nevertheless, the predicted mode splitting was significantly smaller than that predicted by these researchers.

The simulations of the infrared spectrum of the recently observed missing-row morphology on H/Si(100) were consistent with the energies and polarizations observed experimentally. The simulations of point defects on H/Si(100) surfaces showed that interadsorbate strain can cause large shifts in energies of both monohydrides and dihydrides. The pronounced line broadening observed experimentally was explained in terms of heterogeneous strain fields surrounding point defects. Although the spectrum of an ideal missing-row H/Si(100) structure would likely have linewidths comparable to other near-perfect H/Si surfaces, such as NH_4F-etched H/Si(111) and H/Si(110), the calculations suggested that the high density and heterogeneous distribution of point defects on NH_4F-etched H/Si(100) explain the unusually broad linewidths observed experimentally.

REFERENCES

[1] Y. J. Chabal and K. Raghavachari, Surf. Sci. **502-503**, 41 (2002).

[2] Y. J. Chabal, G. S. Higashi, K. Raghavachari, and V. A. Burrows, J. Vac. Sci. Technol. A **7**, 2104 (1989).

[3] P. Jakob, Y. J. Chabal, K. Raghavachari, and S. B. Christman, Phys. Rev. B **47**, 6839 (1993).

[4] K. Raghavachari, P. Jakob, and Y. J. Chabal, Chem. Phys. Lett. 206, 156 (1993).

[5] S. Watanabe, Surf. Sci. **415**, 385 (1998).

[6] P. Jakob and Y. J. Chabal, J. Chem. Phys. **95**, 2897 (1991).

[7] E. Kaxiras and J. D. Joannopoulos, Phys. Rev. B, **37**, 8842 (1988).

[8] X.-P. Li and D. Vanderbilt, Phys. Rev. Lett. **69**, 2543 (1992).

[9] X.-P. Li, D. Vanderbilt and R. D. King-Smith, Phys. Rev. B **50**, 4637 (1994).

[10] B. Sandford, A. Mazur and J. Pollmann, Phys. Rev. B **51**, 7139 (1995).

[11] V. Gräschus, A. Mazur and J. Pollmann, Phys. Rev. B **56** 6482 (1997).

[12] A good overview of surface phonon calculation methods is given in: G. P. Srivastava, *Theoretical Modeling of Semiconductor Surfaces* (World Scientific, Singapore, 1999).

[13] W. Goldammer and W. Ludwig, Phys. Lett. A **133**, 85 (1988).

[14] L. Miglio, P. Ruggerone and G. Benedek, Phys. Scr. **37**, 768 (1988).

[15] Several researchers use the phrase "*ab-initio*" for Hartree-Fock-based methods only and not for DFT methods. This distinction is not well defined and not widely followed. In this chapter, the term "first principles" is used to refer to all quantum mechanical methods, including both Hartree-Fock-based and DFT methods.

[16] For an introduction to different solid models in simulation, see P. Deák, Phys. Status Solidi B **217**, 9 (2000).

[17] For a discussion on cluster and slab models of surfaces, see R. A. Evarestov, Th. Bredow, and K. Jug, Phys. Sol. St. **43**, 1774 (2001).

[18] Y.J. Chabal and K. Raghavachari, Phys. Rev. Lett. **53**, 282 (1984).

[19] Y.J. Chabal and K. Raghavachari, Phys. Rev. Lett. **54**, 1055 (1985).

[20] R. Honke, P. Jakob, Y. J. Chabal, A. Dvořák, S. Tausendpfund, W. Stigler, P. Pavone, A. P. Mayer, and U. Schröder, Phys. Rev. B **59**, 10996 (1999).

[21] S. Ciraci and I. P. Batra, Surf. Sci. **178**, 80 (1986).

[22] J. E. Northrup, Phys. Rev. B **44,** 1419 (1991).

[23] K. Endo, K. Arima, K. Hirose, T. Kataoka, Y. Mori, J. Appl. Phys. **91**, 4065 (2002).

[24] K. Tagami, E. Tsuchida and M. Tsukada, Surf. Sci. **446**, L108 (2000).

[25] U. Freking, P. Krüger, A. Mazur, J. Pollmann, Phys. Rev. B **69**, 035315 (2004).

[26] K. Tagami and M. Tsukuda, Surf. Sci. **384**, 308 (1997). The authors use nine Si layers per slab in this work.

[27] K. Tagami and M. Tsukuda, J. Phys. Soc. Jpn. **68**, 3303 (1999). The authors use five Si layers per slab in this work.

[28] Arnold *et al*. and Tausendpfund *et al*., unpublished results. The details of their results have been given in reference 25.

[29] I. T. Clark, B. S. Aldinger, A. Gupta, and M. A. Hines, J. Phys. Chem. C **114**, 423 (2010).

[30] M. F. Faggin, S. K. Green, I. T. Clark, K. T. Queeney, and M. A. Hines, J. Am. Chem. Soc. **128**, 11455 (2006).

[31] W. Kohn and L. J. Sham, Phys. Rev. **140**, A1133 (1965).

[32] A detailed overview of computational aspects of DFT can be found in: D. S. Sholl and J. A. Steckel, *Density Functional Theory: A Practical Introduction* (John Wiley and Sons, New Jersey, 2009).

[33] A detailed description of pseudopotential formalism in DFT can be found in W. E. Pickett, Comp. Phys. Rep. **9**, 115 (1989).

[34] P. E. Blöchl, Phys. Rev. B **50,** 17953 (1994).

[35] G. Kresse and D. Joubert, Phys. Rev. B **59**, 1758 (1999).

[36] M. C. Payne, M. P. Teter, D. C. Allan, T. A. Arias, and J. D. Joannopoulos, Rev. Mod. Phys. **64**, 1045 (1992).

[37] G. Kresse and J. Furthmueller, Phys. Rev. B **54,** 11169 (1996).

[38] G. Kresse and J. Furthmueller, Computat. Mater. Sci. **6,** 15 (1996).

[39] G. Kresse and J. Hafner, Phys. Rev. B **48,** 13115 (1993).

[40] A recent review on DFT methods in VASP simulation package can be found in J. Hafner, J. Comput. Chem. **29**, 2044 (2008).

[41] D. M. Ceperly and B. J. Alder, Phys. Rev. Lett. **45**, 566 (1980).

[42] J. P. Perdew and A. Zunger, Phys. Rev. B **23**, 5048 (1981).

[43] J. P. Perdew, K. Burke, and M. Ernzerhof, Phys. Rev. Lett. **77**, 3865 (1996).

[44] J. P. Perdew, A. Ruzsinszky, G. I. Csonka, O. A. Vydrov, G. E. Scuseria, L. A. Constantin, X. Zhou, and K. Burke, Phys. Rev. Lett. **100**, 136406 (2008).

[45] R. D. King-Smith, M. C. Payne, and J. S. Lin, Phys. Rev. B **44**, 13063 (1991).

[46] H. J. Monkhorst and J. D. Pack, Phys. Rev. B **13**, 5188 (1976).

[47] P. E. Blöchl, O. Jepsen and O. K. Andersen, Phys. Rev. B **49**, 16223 (1994).

[48] M. Methfessel and A. T. Paxton, Phys. Rev. B **40**, 3616 (1989).

[49] A simple discussion of this method can be found in W. H. Press, B. P. Flannery, S. A. Teukolsky and W.T. Vetterling, *Numerical Recipes: The Art of Scientific Computing* (Cambridge University Press, New York, 1986).

[50] S. Baroni, S. de Gironcoli, A. D. Corso and P. Ginnozzi, Rev. Mod. Phys. **73**, 515 (2001).

[51] K.-W. Lee and W. E. Pickett, Phys. Rev. B **68**, 85308 (2003).

[52] R. G. Hennig, A. Wadhera, K. P. Driver, W. D. Parker, C. J. Umrigar, and J. W. Wilkins, Phys. Rev. B **82**, 14101 (2010).

[53] R. Hull, ed., *Properties of Crystalline Silicon* (INSPEC, London, 1999), chap. 3. Structural and Mechanical Properties, p. 89.

[54] P. Dumas, Y. J. Chabal, and G. S. Higashi, Phys. Rev. Lett. **65**, 1124 (1990).

[55] Y. Caudano, P. A. Thiry, and Y. J. Chabal, Surf. Sci. **502-503**, 91 (2002).

[56] H. W. Kattenberg and A. Oskam, J. Mol. Spec. **49**, 52 (1974).

[57] K. Raghavachari, P. Jakob, and Y. J. Chabal, Chem. Phys. Lett. **206**, 156 (1993).

[58] M. A. Hines, Y. J. Chabal, T. D. Harris, and A. L. Harris, J. Chem. Phys. **101**, 8055 (1994).

[59] S. Watanabe, Surf. Sci. **351**, 149 (1996).

[60] This symmetry breaking on H/Si(100) was implemented in VASP by displacing the H atoms away from their symmetric position before relaxing the structures.

[61] The vibrational energies of the H/Si(100) missing-row structure were also calculated with other functionals and normal PAW pseudopotentials. Calculations with the PBE functional and hard PAW pseudopotentials best matched the experimental data, thus supporting their use in this study. These results are included in Appendix C.

[62] The bend modes of the unstrained and strained monohydrides were strongly coupled to each other and to the vibrations of neighboring atoms, making a simple and accurate description of the modes difficult. These modes are therefore not included.

[63] T. A. Newton, J. A. Boiani, and M. A. Hines, Surf. Sci. **430**, 67 (1999).

[64] These mode energies should only be compared with the 4 × 2 H/Si(100) structures and not with the missing-row structure in Fig. 6.9 since that used different (reciprocal space) projectors in calculations than the 4 × 2 supercells.

[65] For a discussion on correction factors employed in vibrational spectra calculations, see R. J. Meier, Vib. Spec. **43**, 26 (2007).

[66] R. B. Gerber, G. M. Chaban, B. Brauer, and Y. Miller, in *Theory and Applications of Computational Chemistry: The First Forty Years*, edited by C. E. Dykstra, G. Frenking, K. S. Kim, and G. E. Scuseria (Elsevier B. V. , Amsterdam, 2005), Ch. 9.

[67] B. S. Aldinger, Ph.D. Dissertation, Cornell University, 2010.

Appendix A

STM Electronics

This appendix contains the Schematic for currently implemented Leg Piezo Driver Circuit.

Figure A.1. Circuit diagram for 3-Trident Leg Piezo Driver. Circuit designed by Melissa A. Hines.

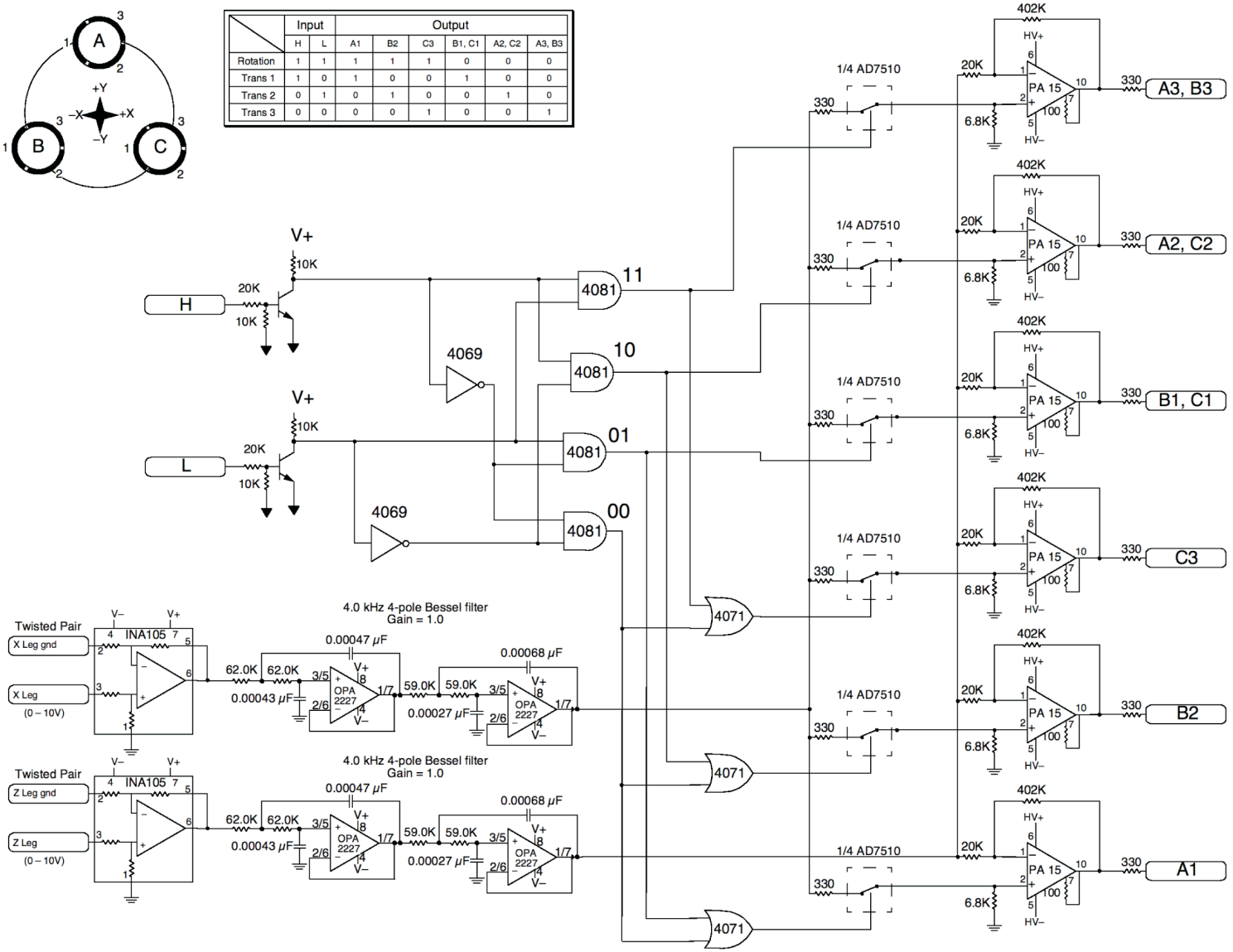
A
B
C
+Y
−X
+X
−Y
Input
Output
H
L
A1
B2
C3
B1, C1
A2, C2
A3, B3
Rotation
Trans 1
Trans 2
Trans 3
V+
10K
20K
H
L
4069
4081
11
10
01
00
4071
1/4 AD7510
330
402K
HV+
HV−
PA 15
6.8K
A3, B3
A2, C2
B1, C1
C3
B2
A1
Twisted Pair
X Leg gnd
X Leg
(0 – 10V)
Z Leg gnd
Z Leg
INA105
V−
4.0 kHz 4-pole Bessel filter
Gain = 1.0
62.0K
0.00047 μF
0.00043 μF
59.0K
0.00068 μF
0.00027 μF
OPA
2227

Appendix B

Etch Rates used in KMC Simulations

The KMC simulation code of H/Si(100) etching currently defines 20 kind of kinetically-distinct sites. In the following, these sites are defined and then the etch rates used in the simulations in Chapter 5 are tabulated.

The following definitions are used:
(i) Trihydride: Silicon atom with three bonds to H atoms and one bond to a silicon atom.
(ii) Dihydride: Silicon atom with two bonds to H atoms and two to silicon atoms.
(iii) Monohydride: Silicon atom with one bond to a H atom and three to silicon atoms.
(iv) Bulk silicon: Silicon atom with four bonds to silicon atoms.

The sites defined in the code are as follows:

1) Trihydride
2) LooseDi: Dihydride bonded to another dihydride or trihydride.
3) IsoDi: A dihydride that is not a looseDi with two H atoms that are sterically unhindered.
4) Str1Di: Same as IsoDi except one H atom is sterically hindered.
5) Str2Di: Same as IsoDi except both H atoms are sterically hindered and at least one of the H atoms is strained by a Str1 species (e.g., Str1Di, Str1DiM).
6) ConstrDi: Same as Str2Di except that neither H is strained by a Str1 species.
7) IsoDiM: Same as IsoDi except the dihydride silicon atom is bonded to at least one sterically unstrained monohydride and not bonded to a sterically strained monohydride.
8) Str1DiM: Same as Str1Di except the dihydride silicon atom is bonded to at least one sterically unstrained monohydride and not bonded to a sterically strained monohydride.
9) Str2DiM: Same as Str2Di except the dihydride silicon atom is bonded to at least one sterically unstrained monohydride and not bonded to a sterically strained monohydride.
10) ConstrDiM: Same as ConstrDi except the dihydride silicon atom is bonded to at least one sterically unstrained monohydride and not bonded to a sterically strained monohydride.
11) IsoDiStrM: Same as IsoDi except the dihydride silicon atom is bonded to at least one monohydride whose H atom is sterically hindered.
12) Str1DiStrM: Same as Str1Di except the dihydride silicon atom is bonded to at least one monohydride whose H atom is sterically hindered.
13) Str2DiStrM: Same as Str2Di except the dihydride silicon atom is bonded to at least one monohydride whose H atom is sterically hindered.
14) ConstrDiStrM: Same as ConstrDi except the dihydride silicon atom is bonded to at least one monohydride whose H atom is sterically hindered.

15) IsoRigidMono: A monohydride that is bonded to three bulk silicon atoms with a sterically unhindered H atom. This is also a H/Si(111) terrace site.
16) StrRigidMono: A monohydride that is bonded to three bulk silicon atoms with a sterically hindered H atom.
17) IsoLooseMono: A sterically unhindered monohydride that is bonded to at least one silicon hydride. These sites are found, for example, on H/Si(110) facets.
18) StrLooseMono: A sterically hindered monohydride that is bonded to at least one silicon hydride.
19) IsoDistMono: A sterically unhindered monohydride that is bonded to a str1DiM. This site is typified by a H/Si(111) kink site.
20) StrDistMono: A sterically hindered monohydride that is bonded to a str1DiStrM.

Tables B.1-B.4 list the etch rates used for the simulations reported in Chapter 5.

Table B.1. Etch rates for the model used in Section 5.3.1. The sites with the same etch rates in the KMC code are listed in the brackets.

Figure	Monohydrides (isoRigidMono, strRigidMono, isoLooseMono, strLooseMono, isoDistMono, strDistMono)	Dihydrides (looseDi, isoDi, str1Di, str2Di, constrDi, isoDiM, str1DiM, str2DiM, constrDiM, isoDiStrM, str1DiStrM, str2DiStrM, constrDiStrM)	Trihydrides
5.6 (a)	1	1	∞
5.6 (b)	10^{-2}	1	∞
5.6 (c)	10^{-4}	1	∞
5.7 (a)	1	10^{-4}	∞
5.7 (b)	1	10^{-2}	∞
5.7 (c)	1	1	∞
5.7 (d)	10^{-2}	1	∞
5.7 (e)	10^{-4}	1	∞

Table B.2. Etch rates for the model used in Section 5.3.2. The sites with the same etch rates in the KMC code are listed in the brackets.

Figure	Monohydrides (isoRigidMono, strRigidMono, isoLooseMono, strLooseMono, isoDistMono, strDistMono)	Unstrained Dihydride (looseDi, isoDi, isoDiM, isoDistrM)	Strained Dihydrides (str1Di, str2Di, constrDi, str1DiM, str2DiM, constrDiM, str1DiStrM, str2DiStrM, constrDiStrM)	Trihydrides
5.8 (a)	10^{-6}	10^{2}	10^{-2}	∞
5.8 (b)	10^{-6}	1	10^{-2}	∞
5.8 (c)	10^{-6}	10^{-2}	1	∞
5.8 (d)	10^{-6}	10^{-2}	10^{2}	∞

Table B.3. Etch rates for the model used in Section 5.3.3. The sites with the same etch rates in the KMC code are listed in the brackets.

Figure	Monohydrides (isoRigidMono, strRigidMono, isoLooseMono, strLooseMono, isoDistMono, strDistMono)	Unstr Dihydride (looseDi, isoDi, isoDiM, isoDistrM)	Str^1 Dihydride (str1Di, str1DiM, str1DiStrM)	Str^2 Dihydride (str2Di, constrDi, str2DiM, constrDiM, str2DiStrM, constrDiStrM)	Trihydrides
5.12 (a1)	10^{-6}	0.01	10^{-4}	10^{-6}	∞
5.12 (a2)	10^{-6}	0.01	10^{-3}	10^{-5}	∞
5.12 (a3)	10^{-6}	0.01	0.01	10^{-4}	∞
5.12 (a4)	10^{-6}	0.01	0.1	10^{-3}	∞
5.12 (a5)	10^{-6}	0.01	1	0.01	∞
5.12 (b1)	10^{-6}	0.01	10^{-4}	10^{-5}	∞
5.12 (b2)	10^{-6}	0.01	10^{-3}	10^{-4}	∞
5.12 (b3)	10^{-6}	0.01	0.01	10^{-3}	∞
5.12 (b4)	10^{-6}	0.01	0.1	0.01	∞
5.12 (b5)	10^{-6}	0.01	1	0.1	∞
5.12 (c1)	10^{-6}	0.01	10^{-4}	10^{-3}	∞
5.12 (c2)	10^{-6}	0.01	10^{-3}	0.01	∞
5.12 (c3)	10^{-6}	0.01	0.01	0.1	∞
5.12 (c4)	10^{-6}	0.01	0.1	1	∞
5.12 (c5)	10^{-6}	0.01	1	10	∞

Table B.4. Etch rates for the model used in Section 5.3.4. The sites with the same etch rates in the KMC code are listed in the brackets.

Figure	Monohydrides (isoRigidMono, strRigidMono, isoLooseMono, strLooseMono, isoDistMono, strDistMono)	Di (looseDi, isoDi, str1Di, str2Di, constrDi,)	α-Di^{str} (isoDiM, str1DiM, str2DiM, constrDiM,)	α-Di^{u} (isoDiStrM, str1DiStrM, str2DiStrM, ConstrDiStrM)	Trihydrides
5.14 (a1)	10^{-6}	0.01	10^{-3}	10^{-5}	∞
5.14 (a2)	10^{-6}	0.01	0.01	10^{-4}	∞
5.14 (a3)	10^{-6}	0.01	0.1	10^{-3}	∞
5.14 (a4)	10^{-6}	0.01	1	0.01	∞
5.14 (a5)	10^{-6}	0.01	10	0.1	∞
5.14 (b1)	10^{-6}	0.01	10^{-3}	10^{-3}	∞
5.14 (b2)	10^{-6}	0.01	0.01	0.01	∞
5.14 (b3)	10^{-6}	0.01	0.1	0.1	∞
5.14 (b4)	10^{-6}	0.01	1	1	∞
5.14 (b5)	10^{-6}	0.01	10	10	∞
5.14 (c1)	10^{-6}	0.01	10^{-3}	0.1	∞
5.14 (c2)	10^{-6}	0.01	0.01	1	∞
5.14 (c3)	10^{-6}	0.01	0.1	10	∞
5.14 (c4)	10^{-6}	0.01	1	100	∞
5.14 (c5)	10^{-6}	0.01	10	10^{3}	∞

Appendix C

Density Functional Theory Calculations

C.1. VASP Parameters

Following is a list of VASP parameters that were used in the calculations. The details of these parameters can be found on the VASP guide available online.[1]

The terms included in the INCAR file:

(a) ISMEAR

This parameter determined the method used for total energy calculations. ISMEAR was set to -5 (no SIGMA needed) for the calculations using tetrahedron methods with Blöchl correction, and was set to 0 with SIGMA = 0.1 for calculations using Gaussian smearing methods.

(b) LREAL

This parameter determined whether the PAW pseudopotentials were implemented in real (LREAL = TRUE) or reciprocal space projectors (LREAL = FALSE). For the 4 × 2 H/Si(100) surfaces using real space projector basis, an additional parameter ROPT with value 2×10^{-4} eV/atom was used, which determined the precision of the real space projectors.

(c) ISIF

This tag was used to control which degrees of freedom were allowed to change. For the structural optimization ISIF was set to 3 for bulk Si, and 2 for the slabs and silane in a box. For the vibrational calculations, this value was 3 for bulk Si and 5 for silane in a box and the slabs.

(d) IBRION

This tag determined the algorithms used for the motion of atoms in a calculation. This was set to 2 for the structural optimizations and 8 for the vibrational calculations.

(e) EDIFF

This parameter sets the minimum difference in the supercell energies obtained from two successive structure optimization steps which must be reached before terminating the optimizations. This parameter was set to 10^{-5} eV for most calculations.

(f) ENCUT

This parameter sets the energy cut-off for the plane-wave basis set in eV. Its value is specified with the calculations.

The *k*-point mesh size was set in the KPOINTS file.

C.2. Optimization of Computational Parameters for H/Si slabs

The methods used for optimization of computational parameters for the slabs used to model the H/Si surfaces are described in Chapter 6. This section includes the

[1] http://cms.mpi.univie.ac.at/vasp/guide/vasp.html

optimization tests that were performed for different slabs to ensure the convergence of their vibrational energies.

C.2.1. H/Si(111) surface

The variations of the total cell and Si-H vibrational energies of the H/Si(111) surface with *k*-point mesh are shown in Table C.1. The cell and vibrational energies variations reduced to less than 0.1 eV and 1 cm^{-1}, respectively, for *k*-point meshes of 5 × 5 × 2 or denser.

Table C.1. Total cell and the Si-H stretch and bend mode energies calculated with different *k*-point meshes for the H/Si(111) supercell shown in Fig. 6.1. The energy cut-off was 800 eV for the structural relaxation and 700 eV for the vibrational mode calculations.

k-mesh	Cell Energy (eV)	Si-H stretch (cm^{-1})	Si-H bend (cm^{-1})
3 × 3 × 2	-38.240	2106.95	615.81
5 × 5 × 2	-39.052	2107.64	615.22
5 × 5 × 5	-39.052	2107.65	615.20
7 × 7 × 2	-39.135	2108.07	614.83

C.2.2. H/Si(111) surface miscut towards the $\langle 11\bar{2} \rangle$direction

Simulations of the 10.0° miscut H/Si(111) surface shown in Fig. 6.5 with available computational resources necessitated the reduction of *k*-point mesh to 1 × 4 × 1 and use of Gaussian smearing methods (ISMEAR = 0) during the vibrational energy calculations. To test if the use of Gaussian smearing methods instead of the tetrahedron method [used for most other surfaces] changed the calculated vibrational energies, the vibrational energy calculations were repeated for the (smaller) 15.8° miscut structure

Table C.2. Si-H vibrational energies of H/Si(111) surface miscut by 15.8° towards the $\langle 11\bar{2} \rangle$ direction, shown in Fig. 6.6, calculated with ISMEAR = -5 and ISMEAR = 0.The calculations were performed with normal PAW and PBE functionals, and a vacuum spacing of 7.0 Å. The relaxed structure with an energy cutoff of 650 eV and *k*-point mesh 2 × 4 × 1 was used for both calculations. The vibrational mode calculations were performed with energy cut-off of 650 eV and the *k*-point mesh specified in the table.

Band	Vibrational energy (cm^{-1})	
	k-mesh: 2 × 4 × 1 Tetrahedron method	*k*-mesh: 1 × 4 × 1 Gaussian smearing (SIGMA = 0.05)
B_2	2113.2	2113.6
B_1	2098.8	2098.6
A_3	2103.2	2102.9
B_3	641.4	641.8
B_4	595.9	596.3
A_2	609.5, 618.3	607.1, 618.9

with both methods and 1 × 4 × 1 *k*-point mesh. The results of this calculation are shown in Table C.2. Changing the methods changed the stretch modes energies by <0.5cm^{-1} and the bending mode energies by ~2 cm^{-1}. The vibrational energies were also calculated with SIGMA = 0.1 (ISMEAR = 0), and the energies were same as the results with SIGMA = 0.05 (ISMEAR = 0) to within 1 cm^{-1}.

These results for the 15.8° miscut H/Si(111) surface showed that the Gaussian smearing methods used for surfaces such as the 10.0° miscut H/Si(111) surface and 4 × 2 H/Si(100) supercells did not produce significant shift in mode energies compared to the tetrahedron method.

C.2.3. H/Si(111) surface miscut towards the $\langle \bar{1}\bar{1}2 \rangle$ direction

This surface had much lower symmetry than the flat H/Si(111) surface and a significant relaxation of the step dihydride. Therefore, the sufficiency of the *k*-point mesh and the number of layers was tested using the 19.9° miscut structure.

(a) k-*Point Meshes*

Table C.3 shows the Si-H vibrational energies of this surface with varying *k*-point mesh. The vibrational energies with a 2 × 4 × 1 mesh was within 1 cm^{-1} of that obtained with a 2 × 8 × 1 mesh. The structure was also relaxed with 4 × 4 × 1 and 2 × 4 × 2 meshes; however the atom positions were identical to the 2 × 4 × 1 results to 0.001 Å. This showed that that the 2 × 4 × 1 mesh was well optimized along all three axes.

Table C.3. The Si-H vibrational energies of vicinal H/Si(111) miscut by 19.9° toward the $\langle \bar{1}\bar{1}2 \rangle$ direction, shown in Fig. 6.6, with different *k*-point meshes. The structural relaxation and vibrational calculations were performed with normal PAW pseudopotentials, PBE functional, and an energy cut-off of 650 eV. The vacuum spacing of the calculation with 2 × 4 × 1 mesh was 7.0 Å; 7.4 Å was used for the other two. This increase in vacuum spacing (to incorporate the effect of miscut) negligibly changed the mode energies. [The vibrational energies reported in Chapter 6 used hard PAW pseudopotentials and therefore are slightly different from these values.]

Band	Vibrational energies (cm^{-1}) with *k*-point meshes		
	2 × 4 × 1	2 × 6 × 1	2 × 8 × 1
C_3	2150.2	2150.6	2150.7
C_1	2124.6	2124.8	2124.8
C_2	2120.0	2120.7	2120.7
A_1	2103.1	2103.2	2103.2
C_4	893.2	893.0	893.1
C_5	636.6	635.6	635.4
A_2	614.1, 621.5	613.3, 622.4	613.0, 622.5

(b) Slab Thickness

To check the sufficiency of bulk Si layers to allow for proper relaxation of the step dihydride on vicinal Si(111) surfaces, Si atoms were added to the bottom layer of the slab shown in Fig. 6.6, and calculations repeated. All calculations had only the

bottom two layers (single bilayer) of Si atoms frozen. As listed in Table C.4, increasing the number of Si atoms from 18 (used for the results presented in Chapter 6) to 24 changed the Si-H vibrational energies by less than 2 cm^{-1}.

Table C.4. The Si-H vibrational energies for H/Si(111) miscut by 19.9° toward the $\langle \bar{1}\bar{1}2 \rangle$ direction, shown in Fig. 6.6, with different number of bulk Si atoms in the slab. The calculations were done with hard PAW potentials, PBE functionals, 2 × 4 × 1 *k*-point mesh, and a vacuum spacing of 7.4 Å. Structures optimization and vibrational mode calculations used 800 eV and 750 eV energy cut-offs, respectively.

Band	Vibrational energies (cm^{-1})		
	18 Si atoms	20 Si atoms	24 Si atoms
C_3	2152.5	2151.6	2150.1
C_1	2126.3	2125.6	2124.3
C_2	2122.4	2121.4	2121.0
A_1	2105.1	2104.8	2102.6
C_4	892.4	891.7	891.9
C_5	636.7	636.6	636.7
A_2	614.4, 621.8	613.8, 621.7	614.0, 622.0

C.2.4. H/Si(110) surface

Since the H/Si(110) surface was modeled as a 35.5º miscut H/Si(111), the system had much lower symmetry than the H/Si(111) slab. Therefore, the sufficiency of the *k*-point mesh and the vacuum spacing was tested. In addition, this structure was also used to optimize the energy cut-off with the hard version of the PAW pseudopotentials.

(a) k-*Point Meshes and Vacuum Spacing*

As shown in Table C.5, increasing the *k*-point mesh density from 3 × 4 × 1 to 6 × 8 × 1 and the vacuum spacing from 10 Å to 12 Å changed the vibrational energies by less than 1 cm^{-1}. The vacuum spacing was also independently varied by keeping the *k*-point mesh constant at 3 × 4 × 1, and the atom positions changed by less than 0.001 Å. These results showed that both values were optimum for the vibrational energy calculations.

Table C.5. The vibrational energies for H/Si(110) surface, with different *k*-point meshes and vacuum spacings. The calculations were performed with normal PAW and PBE functionals at an energy cut-off of 650 eV.

Band	Vibrational energy (cm^{-1})	
	k-point mesh: 3 × 4 × 1 Vacuum spacing = 10 Å	*k*-point mesh: 6 × 8 × 1 Vacuum spacing = 12 Å
B_2	2114.6	2115.3
B_1	2097.1	2097.5
B_3	626.6	627.0
B_4	600.0	599.3

(b) Energy Cut-off

As shown in Table C.6, the difference in vibrational energies calculated with energy cut-offs of 700 eV and 800 eV was less than 2 cm^{-1}. These results showed that energy cut offs of 700 eV and above were sufficient for vibrational energy calculations with hard PAW and PBE functionals.

Table C.6: The vibrational energies for H/Si(110) surface calculated at different energy cut-offs. The structural relaxation as well as the vibrational mode calculations were done with hard PAW potentials, PBE functionals, vacuum spacing of 12.05 Å, 3 × 4 × 1 *k*-point mesh, and the energy cut-offs given in the table.

Mode	Vibrational energy (cm^{-1}) with energy cut-off		
	600 eV	700 eV	800 eV
B_2	2121.2	2117.6	2115.7
B_1	2102.5	2098.9	2098.1
B_3	626.5	626.2	627.0
B_4	600.9	600.3	601.0

C.2.5. Missing-Row Morphology on H/Si(100)

The missing-row structure observed on the NH_4F-etched Si(100) surface is experimentally observed and characterized and was therefore used to test the accuracy of different potentials and exchange-correlation functionals. In addition, the sufficiency of the *k*-point mesh was also tested. For these structures, the mode splittings were relatively less dependent on the computational parameters than the absolute mode energies (*vide infra*), and therefore were used as the important indicator of accuracy.

(a) Pseudopotentials and Exchange Correlation Functionals

The Si-H stretch energies for the missing-row morphology calculated with various functionals and pseudopotentials are shown in Table C.7. PBE functional predicted the most accurate mode splitting for the unstrained and canted strained dihydrides. The LDA functional did not predict the mode ordering observed in experiment.

Based on these data, the hard PAW pseudopotential with the PBE functional predicted the mode splittings most accurately, and therefore were the most suitable choice for this structure.

(b) k-*Point Meshes*

Table C.8 shows the variation of the Si-H stretch energies of the missing-row structure on H/Si(00) with *k*-point meshes used during structural relaxation and vibrational energy calculations. Although large parameter space was not tested, these results showed that the *k*-point meshes of 4 × 8 × 2 and 3 × 6 × 1 used for structural optimizations and the vibrational energy calculations, respectively, with the energy cut-offs (ENCUT) mentioned in the table, were optimum for the calculations.

Table C.7. Si-H stretch mode energies of the missing-row structure, shown in Fig. 6.9, computed using LDA, PBE and PBEsol functionals with regular and hard versions of PAW potentials. Experimental mode energies (at T = 293 K, Chapter 3) are included for comparison. The energy cut-off was 750 eV for all calculation. A k-point mesh of 3 × 7 × 1 was used for the LDA functional, and 3 × 6 × 1 was used for the PBE and PBEsol functionals.

Mode	LDA (cm^{-1})		PBE (cm^{-1})		PBEsol (cm^{-1})	Experimental (cm^{-1})
	Regular	Hard	Regular	Hard	Regular	
D^{c}_{up}	2120.8	2114.5	2144.4	2141.1	2133.6	2143.5
D^{u}_{as}	2121.7	2128.3	2140.7	2136.6	2126.6	2112.2
D^{u}_{ss}	2107.4	2108.1	2129.6	2123.4	2113.2	2103.5
D^{c}_{dn}	2017.3	2051.3	2057.3	2071.1	2028.9	2083.3
$D^{c}_{up} - D^{c}_{dn}$ splitting	103.5	63.2	87.1	70.0	104.7	60.2
$D^{u}_{as} - D^{u}_{ss}$ splitting	14.3	20.2	11.1	13.2	13.4	8.7
Relative order	Incorrect	Incorrect	Correct	Correct	Correct	

Table C.8. Vibrational energies of missing-row structure shown in Fig. 6.9 with varying k-point meshes and energy cut-offs. The calculations used hard PAW and PBE functionals.

Mode	Vibrational Energies (cm^{-1})		
	Relaxation ENCUT :750 eV k-mesh: 3 × 6 × 1 Vibrational Calculations ENCUT: 750 eV k-mesh: 3 × 6 × 1	Relaxation ENCUT :850 eV k-mesh: 4 × 8 × 2 Vibration Calculations ENCUT: 750 eV k-mesh: 3 × 6 × 1	Relaxation ENCUT :850 eV k-mesh: 4 × 8 × 2 Vibrational Calculations ENCUT: 750 eV k-mesh: 3 × 5 × 1
D^{c}_{up}	2141.1	2142.9	2142.9
D^{u}_{as}	2136.6	2138.4	2138.3
D^{u}_{ss}	2123.4	2126.9	2126.9
D^{c}_{dn}	2071.1	2076.7	2077.6
$D^{c}_{up} - D^{c}_{dn}$ splitting	70.0	66.2	65.3
$D^{u}_{as} - D^{u}_{ss}$ splitting	13.2	11.4	11.4

C.2.6. H/Si(100) – 4 × 2 supercell

For the 4 × 2 supercell structures of H/Si(100), real space projectors were used because of computational efficiency. In the real space projectors, the parameter ROPT determines the accuracy of the projectors (lower value of ROPT denotes higher precision). Table C.9 shows the variation of one of the 4 × 2 supercell structures with energy cut-off and ROPT. These data showed that the change in ROPT value and energy cut-off changed absolute mode energies significantly, but the mode splittings showed negligible variations (< 2 cm^{-1}).

Table C.9. Vibrational energies of the 4 × 2 H/Si(100) supercell with 3 unstrained dihydrides, shown in Fig. 6.12(b), with change in ROPT (in meV/atom) and energy cut-off (in eV). The structures were optimized with a 2 × 3 × 2 *k*-point mesh and an energy cut-off of 850 eV. Vibrational energies were calculated with 1 × 2 × 1 *k*-point mesh and the energy cut-offs given in the table. Only the Si-H stretch energies of opposite monohydride (opp. mono.), unstrained dihydride (unstr. di.), and the highest "up" and lowest "down" modes of canted dihydrides are specified here.

Mode	Vibrational energies (cm^{-1})			
	ROPT = 10^{-3} ENCUT = 750 eV	ROPT = 5×10^{-4} ENCUT = 750 eV	ROPT = 2×10^{-4} ENCUT = 750 eV	ROPT = 2×10^{-4} ENCUT = 850 eV
Opp. Mono. Sym.	2121.6	2167.1	2162.5	2154.1
Opp. Mono. Asym.	2108.1	2153.4	2148.5	2140.7
Highest Up mode	2107.3	2152.8	2149.1	2138.7
Unstr. Di. Asym.	2101.3	2145.8	2143.8	2135.3
Unstr. Di. Sym.	2089.4	2135.4	2131.0	2122.6
Lowest Down mode	2039.4	2083.9	2081.1	2071.8
Opp. Mono split	13.5	13.7	14.0	13.4
Up/Down split	67.9	68.9	68.0	66.9
Unstr. Di. split	11.9	10.4	12.8	12.7

Appendix D

Calculation of Born-Effective Charges

One possible theoretical method to calculate transition dipole moments of a vibrational mode is the Born-effective charge (BEC) method. The Born effective charge tensor of an atom k is defined as

$$Z_{\alpha\beta}(k) = \left.\frac{\partial^2 E}{\partial \varepsilon_\beta \partial u_{k\alpha}}\right|_{\varepsilon_\beta = 0, u_{k\alpha} = 0},$$

where E is the energy of the system (or the supercell), ε_β is the electric field along the direction β (= x, y, or z), and $u_{k\alpha}$ is the displacement vector for atom k along the direction α (= x, y, or z). In essence, the BEC tensor represents the changes in charge on an atom (which is the derivative of energy with respect to electric field at infinitesimal electric fields) with infinitesimal displacement from its equilibrium position. Using the BEC tensor, the Cartesian components of the transition dipole moment of a normal vibrational mode, which are also termed mode effective charges by Gonze and Lee,[1] are

$$Z_\beta^* = \frac{\sum_k \sum_\alpha Z_{\alpha\beta}(k) u_{k\alpha}}{\sum_k \left(\sum_\alpha u_{k\alpha}^2 \right)}.$$

This approach has been used by Lee et al.[2] to predict the infrared response of LiBC crystals.

The calculations of BECs using VASP posed a practical problem. The convergence of BECs with respect to k-point mesh and vacuum spacing required values of these parameters which were beyond the computational resources available.

This appendix presents the optimization of the vacuum spacing and k-point meshes for BECs of surface Si and H atoms on the flat H/Si(111) surface shown in Fig. 6.1. The BEC tensors for these atoms, obtained with relatively large values of the vacuum spacing and k-points, were diagonal, and unexpectedly, the Z_{zz} component (Cartesian axes as defined in Fig. 6.1) was significantly smaller than the Z_{xx} and Z_{yy} elements, which were of almost equal magnitude (*vide infra*). To test if these results were related to the implementation of VASP software, the calculations were repeated with another density functional theory code — Car-Parrinello Molecular Dynamics (CPMD).[3] These studies showed trends for the calculations of BECs that might help in further investigations in this direction.

In the following, the results with the two codes are presented, followed by conclusions of this study and future directions.

D.1. Results with VASP

BEC tensors of surface Si and H atoms on H/Si(111) surface were calculated using VASP with various simulation parameters. The BEC tensor elements showed unexpectedly high sensitivity to the vacuum spacing and k-points. Table D.1 lists the

diagonal elements of the BEC tensors as a function of vacuum spacing; the off-diagonal elements were negligible compared to the diagonal elements and therefore are not reported. The *x*- and *y*-diagonal elements showed no dependence on the vacuum spacing; however, the *z*-diagonal elements (Z_{zz}) for both Si and H decreased monotonically with vacuum spacing and did not converge even at a vacuum spacing of 24 Å. Interestingly, plots of Z_{zz} values for both H and Si atoms with 1/(vacuum spacing), as shown in Fig. D.1, were highly linear. By using a linear fit, the Z_{zz} values for the surface H and Si atoms at infinite vacuum spacing were estimated as -0.128 and 0.108, respectively.

Table D.1 The diagonal elements of BEC tensors of surface H and Si atoms on H/Si(111) surface shown in Fig 6.1, calculated with varying vacuum spacing. The calculation were done with PBE functional, hard PAW potentials, 800 eV energy cut off , and *k*-points mesh of 5 × 5 × 1.

Vacuum Spacing (Å)	H			Si		
	Z_{xx}	Z_{yy}	Z_{zz}	Z_{xx}	Z_{yy}	Z_{zz}
6.4	-0.557	-0.556	-0.283	0.279	0.275	0.244
8.4	-0.557	-0.556	-0.249	0.280	0.276	0.213
10.4	-0.557	-0.556	-0.226	0.280	0.276	0.193
12.4	-0.557	-0.556	-0.210	0.280	0.276	0.180
18.4	-0.557	-0.556	-0.182	0.280	0.276	0.156
20.4	-0.557	-0.556	-0.176	0.280	0.276	0.151
24.4	-0.557	-0.556	-0.168	0.280	0.276	0.143

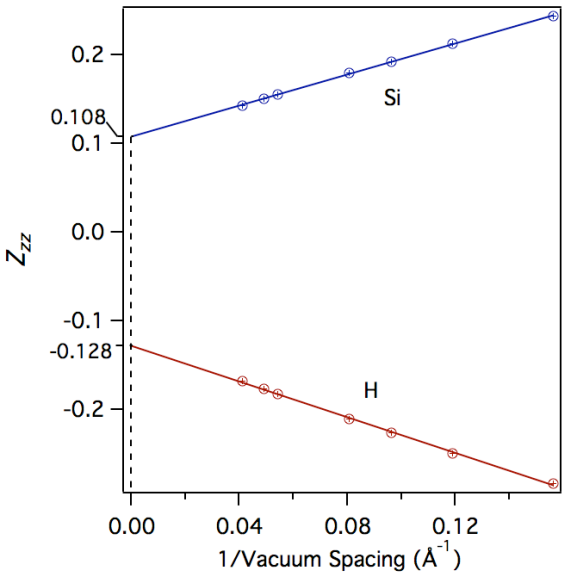

Figure D.1. The *zz*-component of the BEC tensors of H and Si atoms on H/Si(111) surface shown in Fig 6.1 plotted versus the inverse of vacuum spacing between the slabs. Linear fits to the data points are shown as solid line, which are extrapolated to 0 on the *x*-axis to estimate the value of Born effective charges corresponding to an infinite vacuum spacing.

The inverse dependence of Z_{zz} on the vacuum spacing suggested its origin was likely due to electrostatic interactions between the slabs and not due to changes in slab size along *z*-axis, which was supported by the studies with *k*-points variation (*vide infra*). This variation also showed that the converged value at infinite vacuum spacing can be estimated accurately by extrapolating the BEC values calculated at small vacuum spacings.

The dependence of BECs on the *k*-point mesh was studied with two values of vacuum spacing — 6.4 Å and 24.4 Å. Table D.2 shows the diagonal elements of BEC tensor for surface H and Si atoms with 6.4 Å vacuum spacing. The *z*-components of BEC showed negligible variations with the *k*-point mesh, but *x*- and *y*-components required ~ 13 × 13 × 1 *k*-points to reduce variations with 1%, particularly for Si atoms. The change of *k*-points from 7 × 7 × 1 to 7 × 7 × 2 produced negligible differences (< 0.005) in the BEC values, showing that 1 *k*-point in the *z*-direction was sufficient, and also the effect of change in vacuum spacing was not due to change in *z*-dimension of the supercell (which should reflect in the *k*-point dependence).

Table D.2. Born Effective Charges of surface H and Si atoms on H/Si(111) surface shown in Fig 6.1, calculated with varying *k*-points. The calculations were done with PBE functional, hard PAW pseudopotentials, an energy cut off of 700 eV, and a vacuum spacing of 6.4 Å.

k-points	H			Si		
	Z_{xx}	Z_{yy}	Z_{zz}	Z_{xx}	Z_{yy}	Z_{zz}
5 × 5 × 1	-0.557	-0.556	-0.282	0.281	0.277	0.245
7 × 7 × 1	-0.564	-0.563	-0.281	0.584	0.581	0.244
7 × 7 × 2	-0.564	-0.563	-0.285	0.585	0.582	0.245
9 × 9 × 1	-0.566	-0.565	-0.281	0.670	0.668	0.244
11 × 11 × 1	-0.566	-0.566	-0.281	0.695	0.693	0.244
13 × 13 × 1	-0.566	-0.566	-0.281	0.702	0.700	0.244

Table D.3. BECs of surface H and Si atoms on H/Si(111) surface shown in Fig 6.1, calculated at different *k*-points with a vacuum spacing of 24.4 Å. The calculations used PBE functional, normal PAW potentials, and energy cut off of 500 eV. Since *x*- and *y*- elements of the BEC tensor were almost equal, only the *x*- elements are shown.

k-points	H		Si	
	Z_{xx}	Z_{zz}	Z_{xx}	Z_{zz}
1 × 1 × 1	0.762	-0.334	-10.589	0.365
2 × 2 × 1	-0.589	-0.160	0.843	0.135
3 × 3 × 1	-0.505	-0.166	-1.104	0.141
4 × 4 × 1	-0.570	-0.164	0.905	0.142
5 × 5 × 1	-0.556	-0.166	0.243	0.145
6 × 6 × 1	-0.567	-0.164	0.779	0.142
7 × 7 × 1	-0.562	-0.165	0.575	0.145
8 × 8 × 1	-0.566	-0.165	0.729	0.143

The variation of BECs with vacuum spacing of 24.4 Å is listed in Table D.3, which showed convergence trend similar to those at a vacuum spacing of 6.4 Å.

D.2. Results with CPMD

The calculation of BEC tensor of surface Si and H atoms of H/Si(111) surface with CPMD showed trends similar to VASP. In CPMD code, only a 1 × 1 × 1 *k*-point mesh is implemented. This drawback necessitated the study of BEC convergence with supercell size. Also for supercells with orthogonal cell vectors (only), the CPMD code has the possibility to switch off periodicity in the *z*-direction, which removes the electrostatic interaction between the slabs.

Three simulations were performed with the CPMD code: one with a hexagonal 1 × 1 × 1 supercell of Si(111) as shown in Fig. 6.1 having the *z*-periodicity, and two with (orthogonal) $\sqrt{3}\times 2\times 1$ and $\sqrt{3}\times 6\times 1$ supercells in which the *z*-periodicity was switched off. Table D.4 lists the BECs obtained from these simulations. The BEC values depended significantly on the supercell size. Computational limits prevented simulations with larger supercells, hence converged values of BECs could not be obtained. Nonetheless, the simulations with the (largest) $\sqrt{3}\times 6$ supercell yielded values comparable to the VASP results — in particular, the Z_{zz} values obtained from the two codes were ~5 times smaller than the Z_{xx} values.

Table D.4. BECs of surface H and Si atoms on H/Si(111) surface with different supercells of the slab shown in Fig. 6.1, calculated with CPMD software. Z_{xx} and Z_{yy} for H and Si atoms were almost equal, therefore only Z_{xx} values are shown.

Supercell	H		Si	
	Z_{xx}	Z_{zz}	Z_{xx}	Z_{zz}
1 × 1 × 1 (with *z*-periodicity)	-0.621	-0.332	0.990	0.340
$\sqrt{3}\times 2\times 1$ (no *z*-periodicity)	-0.554	-0.303	0.769	-0.306
$\sqrt{3}$ × 6 × 1 (no *z*-periodicity)	-0.527	-0.062	0.948	0.170

D.3. Conclusions and Future directions

The BECs for the surface H and Si atoms of H/Si(111) surface required very large vacuum spacing and *k*-point mesh for convergence. The BEC tensors for both H and Si atoms were diagonal. The *z*-diagonal elements of the BEC tensor showed inverse variation with vacuum spacing, making it possible to estimate the value at infinite vacuum spacing by interpolating the values calculated with small vacuum spacings. The *x*- and *y*-diagonal elements of the two BEC tensors showed a stronger dependence on the *k*-point mesh than the *z*-diagonal element.

The magnitude of the *z*-diagonal elements of the two tensors was ~5 times smaller than the *x*- and *y*-diagonal elements; this trend was consistently observed in results obtained from both VASP and CPMD softwares.

For H/Si(111), there is no direct method to check the accuracy of BEC charges since there is only one Si-H stretch mode with surface normal vibrations and one Si-H bend mode with in-plane vibrations. These two modes lie in very different energy

ranges and accurate experimental estimates of the relative intensities of the Si-H stretch and bending modes are not available.

A future direction to check the accuracy of BEC method to estimate the infrared intensities would be to perform these calculations for a vicinal H/Si(111) surface miscut towards the $\langle \bar{1}\bar{1}2 \rangle$ direction. This surface has both in-plane and perpendicular vibrational modes in the Si-H stretch region, whose relative intensities can be accurately obtain from experimental data.

REFERENCES

[1] X. Gonze and C. Lee, Phys. Rev. B **55**, 10 355 (1997).
[2] K.-W. Lee and W. E. Pickett, Phys. Rev. B **68**, 85308 (2003).
[3] CPMD V3.13 Copyright IBM Corp 1990-2008, Copyright MPI fuer Festkoerperforschung Stuttgart 1997-2001.